5-2014

Image based approach for early assessment of heart failure.

Hisham Z. Sliman
University of Louisville

IMAGE BASED APPROACH FOR EARLY ASSESSMENT OF HEART FAILURE

By

Hisham Z. Sliman
B.S., AIN SHAMS University, 2004, M.S., Purdue School of Engineering and
Technology IUPUI, 2008

A Dissertation
Submitted to the Faculty of the
J. B. Speed School of Engineering of the University of Louisville
in Partial Fulfillment of the Requirements
for the Degree of

Doctor of Philosophy

Department of Computer Engineering and Computer Science
University of Louisville
Louisville, Kentucky

May 2014

IMAGE BASED APPROACH FOR EARLY ASSESSMENT OF HEART FAILURE

By

Hisham Z. Sliman
B.S., AIN SHAMS University, 2004, M.S., Purdue School of Engineering and
Technology IUPUI, 2008

A Dissertation Approved On

April 11,2014

_____

Date

by the following Dissertation Committee:

_____

Adel Elmaghraby, Ph.D., Dissertation Director

_____

Ayman El-Baz, Ph.D., Co-Advisor

_____

Ibrahim Imam, Ph.D.

_____

Olfa Nasraoui, Ph.D.

_____

Xiao-Feng Li, M.D., Ph.D.

ACKNOWLEDGEMENTS

ABSTRACT

IMAGE BASED APPROACH FOR EARLY ASSESSMENT OF HEART FAILURE

Hisham Z. Sliman

April 11, 2014

In diagnosing heart diseases, the estimation of cardiac performance indices requires accurate segmentation of the left ventricle (LV) wall from cine cardiac magnetic resonance (CMR) images. MR imaging is noninvasive and generates clear images; however, it is impractical to manually process the huge number of images generated to calculate the performance indices. In this dissertation, we introduce a novel, fast, robust, bi-directional coupled parametric deformable models that are capable of segmenting the LV wall borders using first- and second-order visual appearance features. These features are embedded in a new stochastic external force that preserves the topology of the LV wall to track the evolution of the parametric deformable models control points. We tested the proposed segmentation approach on 15 data sets in 6 infarction patients using the Dice similarity coefficient (DSC) and the average distance (AD) between the ground truth and automated segmentation contours. Our approach achieves a mean DSC value of 0.926 ± 0.022 and mean AD value of 2.16 ± 0.60 mm compared to two other level set methods that achieve mean DSC values of 0.904 ± 0.033 and 0.885 ± 0.02; and mean AD values of 2.86 ± 1.35 mm and 5.72 ± 4.70 mm, respectively.

Also, a novel framework for assessing both 3D functional strain and wall thickening from 4D cine cardiac magnetic resonance imaging (CCMR) is introduced.

The introduced approach is primarily based on using geometrical features to track the LV wall during the cardiac cycle. The 4D tracking approach consists of the following two main steps: (i) Initially, the surface points on the LV wall are tracked by solving a 3D Laplace equation between two subsequent LV surfaces; and (ii) Secondly, the locations of the tracked LV surface points are iteratively adjusted through an energy minimization cost function using a generalized Gauss-Markov random field (GGMRF) image model in order to remove inconsistencies and preserve the anatomy of the heart wall during the tracking process. Then the circumferential strains are straight forward calculated from the location of the tracked LV surface points. In addition, myocardial wall thickening is estimated by co-allocation of the corresponding points, or matches between the endocardium and epicardium surfaces of the LV wall using the solution of the 3D laplace equation. Experimental results on in vivo data confirm the accuracy and robustness of our method. Moreover, the comparison results demonstrate that our approach outperforms 2D wall thickening estimation approaches.

TABLE OF CONTENTS

LIST OF TABLES

LIST OF FIGURES

CHAPTER I

INTRODUCTION

The heart is a vital muscle. It pumps the blood to the whole body and back continuously. Being a pump, it can become clogged, break down and need repair [1]. Medical reports show that the early detection of heart diseases can assist the clinicians to afford better treatment and leads to increase in the survival rate of patients with these diseases. Nowadays, Medical imaging represents a noninvasive way that is effectively used to assist clinicians and cardiologists in diagnosis, therapy decisions, and surgery operations.

A   Heart Anatomy and Blood Circulation

The heart is a hollow, cone-shaped muscle that is between the lungs and behind the breastbone. Two-thirds of the heart is located to the left of the midline of the body and one-third is to the right. The size of the heart is almost the size of the fist and its weight is negligible compared to the total body weight [1].

As we can see in Fig 1, the heart consists of four chambers: Right Atrium (RA), Right Ventricle (RV), Left Atrium (LA) and Left Ventricle (LV). Each side has its function and all the chambers have a one-way valve at their exit to forbid blood from flowing backwards [2].

To pump blood out of the heart, the heart muscle contracts (systole phase) on two steps. In the first step, the RA and LA contract at the same time, pumping blood to the RV and LV. In the second step, both Ventricles contract together to push blood out of the heart. The heart muscle then relaxes (diastole phase) to

1
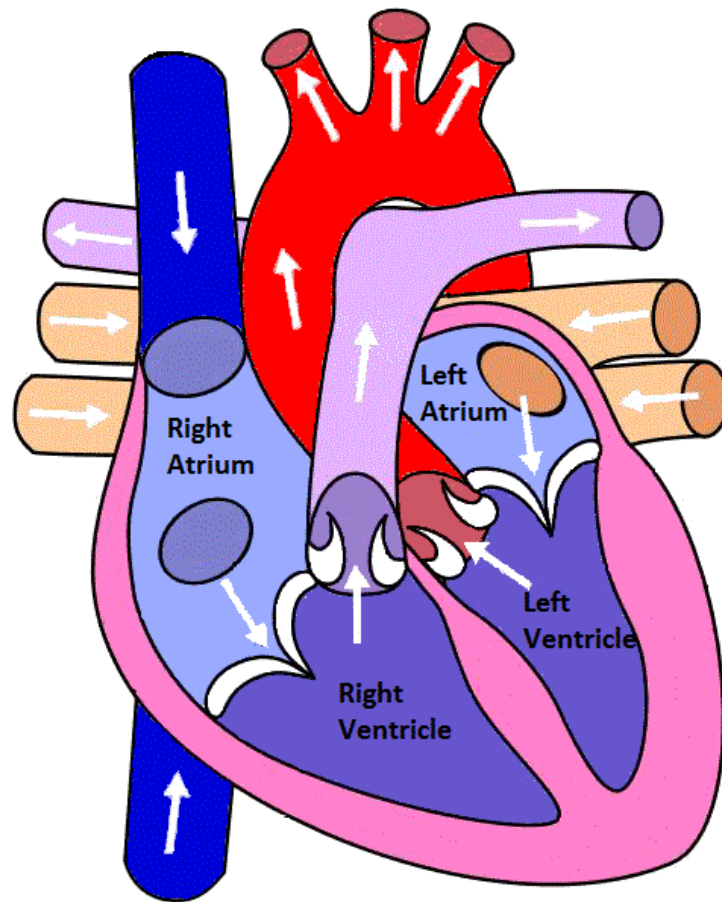
Figure 1. Diagram of the human heart showing heart chambers and the blood flow within the heart. The dotted lines point to the one-way valves. The image is taken from [3].

gather blood and fill up again before the next heartbeat [2].

The heart's right and left sides act differently. The heart's right side gathers oxygen-poor blood from the body to pump it to the lungs where it picks up oxygen and releases carbon dioxide. The left side of the heart then gets oxygen rich blood from the lungs to pump it to the whole body to get the oxygen needed to function properly [1].

Blood circulates through arteries and veins, the blood vessels that make up the circulatory system. Arteries carry the oxygen-rich blood and veins carry the oxygen-poor blood [1].

After the body's organs and tissues have used the oxygen in the blood, all blood returns to the heart from the body in a relatively exhausted status, poor in oxygen, and goes into the RA. The RA contracts allowing the blood to enter into the RV Which contracts to pump blood into the lungs where blood picks up oxygen [4].

Oxygen-rich blood now returns from the lungs and goes into the LA which contracts to deliver blood to the LV. The LV is a very important chamber that pumps blood into the whole body. The LV has a thick muscle, thicker than any other heart chamber, because it must pump blood to the rest of the body against much higher pressure in the general circulation (blood pressure) [4].

The heart, just like any other organ, requires to get oxygen and other nutrients from blood to do its function. The heart does not extract its needs from the blood flowing inside it. Rather, it gets them from blood flowing in coronary arteries that eventually carry blood within the heart muscle. The heart also has veins that collect oxygen-poor blood from the heart muscle [1].

1 Heart Disease

Heart disease includes all types of disorder that affect the heart and its functionality, where heart here means all the parts that are working together to pump blood [2]. Heart's conditions and diseases of the heart's muscle make it hard

for the heart to pump blood normally. Heart disease is the leading cause of mortality in the U.S, 25.4% of all deaths in the USA today are caused by heart disease [5]. Slowly over time this develops to a complete heart failure. Although we are witnessing unprecedented medical advancement, heart disease still causes sudden death and many people die before even reaching the hospital [6, 7].

B Heart Failure

More than 5 million Americans are affected by heart failure and the number of people who have heart failure is growing. More than 500,000 people are newly diagnosed with it each year. Moreover, it is the leading cause of hospitalization in people older than 65 as aging weakens the heart muscle. Heart failure indicates that the heart's pumping power is weaker than it is supposed to be. So, the blood moves through the body at a slower rate, and pressure in the heart increases, then it cannot supply the body's needs of oxygen and nutrients. As a response, the heart stretches more to keep the blood moving for a short while, but in time, the heart muscle weakens and becomes unable to pump as strongly. This being said, if heart failure is not diagnosed and treated early, these patients will have a relentless time course to premature death [1, 2, 4, 5, 7].

1 Causes of Heart Failure

Disorders that damage the heart muscle and lead to heart failure are many, including [1, 2, 4, 5, 7]:

- **Coronary heart disease (CAD):** Also known as coronary heart disease, is caused by narrowing of the arteries that supply oxygen-rich blood to the heart due to plaque build up. This reduces blood flow to the heart muscle and makes it more likely that blood clots will form in the arteries which can partially or completely block blood flow.If the blood supply is cut off, a heart attack results.

- **High Blood Pressure:** Also known as hypertension, is the force of blood exerted against the walls of the arteries as blood flows through them. If this pressure rises and stays high over time, it can weaken the heart and lead to plaque buildup. Blood pressure always refers to two readings. The first is the blood pressure at the heart's maximum contraction; this is called the systolic pressure. The second reading is measured at the heart's minimum contraction, maximum filling, and is called diastolic pressure.

- **Diabetes:** It is a disease in which the body's blood glucose level is too high. The body either doesn't make enough insulin or doesn't use its insulin properly to turn the glucose into energy. Over time, high blood sugar levels can damage and weaken the heart muscle and the blood vessels around the heart, leading to heart failure.

- **Heart attack:** A heart attack may occur when a coronary artery becomes suddenly blocked, stopping the flow of blood to the heart muscle and damaging it. All or part of the heart muscle becomes cut off from its supply of oxygen. A heart attack can damage the heart muscle, resulting in a scarred area that does not function properly.

- **Cardiomyopathy:** Damage to the heart muscle. Causes include artery or blood flow problems, infections, and alcohol and drug abuse.

- **Dilated cardiomyopathy:** In this disorder the heart chambers become dilated because the heart muscle has become weak and cannot pump blood properly. The most common reason is not enough oxygen reaching the heart muscle (ischemia) due to coronary artery disease. Usually the left ventricle is affected.

- **Hypertrophic cardiomyopathy:** A genetic disorder in which the wall of the left ventricle becomes thick, making it harder for blood to leave the heart.

The heart has to work harder to pump blood. This is the leading cause of sudden death in athletes. A father or mother with hypertrophic cardiomyopathy has a 50% chance of passing the disorder onto their children.

- **Conditions that overwork the heart:** Conditions like high blood pressure, heart valve disease, thyroid disease, kidney disease, diabetes, or heart defects present at birth can all cause heart failure. In addition, heart failure can occur when several diseases or conditions are present at once.

2   Types of Heart Failure

Decreased heart's pumping function occurs in two major ways:

1. **Systolic dysfunction:** Also called systolic heart failure; occurs when the heart muscle doesn't contract with enough force, so there is less oxygen-rich blood that is pumped throughout the body.

2. **Diastolic dysfunction:** Also called diastolic heart failure; occurs when the heart contracts normally, but the ventricle – the main pumping chamber – does not relax properly, reducing the amount of blood that can enter the heart and raising blood pressure in the lungs.

Ejection fraction (EF) is a measure of the percentage of blood that the heart pumps out with each beat. EF is used to measure how well the heart pumps with each beat to help determine if heart failure is present. In patients with systolic heart failure, the EF is less than 40%. Heart failure can be detected by modern imaging techniques. If systolic heart failure exists, imaging studies show the heart is enlarged and pumps out less than a normal amount of blood. In contrast, patients with diastolic heart failure usually have a normal ejection fraction, normal heart pumping capability, but Imaging can show that the heart does not fill up with blood properly when the heart is at the diastolic phase [2].

3 Heart Failure Diagnostic Tests

A cardiologist may recommend one or more tests for diagnosing the heart failure [1, 2, 4]:

- **Electrocardiogram (EKG):** An EKG is a simple, painless test that detects and records the heart's electrical activity. The test shows how fast the heart is beating and its rhythm (steady or irregular). An EKG also records the strength and timing of electrical signals as they pass through the heart. It may show whether the walls in the heart's pumping chambers are thicker than normal. Thicker walls can make it harder for the heart to pump blood. An EKG also can show signs of a previous or current heart attack.

- **X-ray:** A chest X-ray takes pictures of the structures inside the chest, such as the heart, lungs, and blood vessels. This test can show whether the heart is enlarged, you have fluid in the lungs, or you have lung disease.

- **Stress Tests:** They can diagnose the heart while it is beating fast. During the test, the patient runs on a treadmill or pedals a bicycle to make the heart work hard. If it's not possible to exercise, the patient may be given medicine to raise his heart rate. Heart tests, such as nuclear heart scanning and Echocardiography, often are done during stress testing.

- **Nuclear Scan:** A nuclear heart scan shows how well blood is flowing through the heart and how much blood is reaching the heart muscle. During the scan, a radioactive substance, tracer, is injected into the bloodstream through a vein. The tracer travels to the heart and releases energy. Special cameras detect the released energy and create pictures of the heart to distinguish between the healthy and damaged areas of the heart muscle. A positron emission tomography scan (PET). PET is a type of nuclear heart scan. It shows the level of chemical activity in areas of the heart. This test can help

the doctor see whether enough blood is flowing to these areas. A PET scan can show blood flow problems that other tests might not detect.

- **Echocardiography (echo):** echo uses sound waves to create a moving picture of the heart. The test shows the size and shape of the heart and how well its chambers and valves work. It can also identify areas of poor blood flow to the heart, areas of heart muscle with contractile dysfunction, and any damage caused by lack of blood flow.

- **Doppler ultrasound:** A Doppler ultrasound uses sound waves to measure the speed and direction of blood flow. This test often is done with echo to give a more complete picture of blood flow to the heart and lungs.

- **Cardiac Catheterization:** During cardiac catheterization, a long, thin, and flexible tube called a catheter is put into a blood vessel in the arm or neck and threaded to the heart. This allows the doctor to look inside the coronary arteries and check the blood pressure and flow in the heart chambers, collect blood samples, and use X-rays to look at the coronary arteries.

- **Coronary angiography:** It is usually done with cardiac catheterization by injecting a dye that can be seen on X-ray into the bloodstream through the tip of the catheter. This allows for monitoring the blood flow and heart mechanics.

- **Cardiac magnetic resonance imaging (CMR):** CMR uses radio waves, magnets, and a computer to create pictures of the heart as it's beating. The test produces both still and moving pictures of the heart and major blood vessels. A CMR can show whether parts of the heart are damaged. Doctors also use CMR in research studies to find early signs of heart failure, even before symptoms appear.

Heart failure can be mitigated by undergoing a bypass surgery or a balloon valvuloplasty. There is also an implantable left ventricular assist device. The latter is for patients who haven't responded to other treatments. Lastly, if nothing works, a person's diseased heart can be exchanged with a healthy donor's heart in a heart transplant surgery.

A heart transplant is a surgery to remove a person's diseased heart and replace it with a healthy heart from a deceased donor. Most of these transplants are done on patients who have end-stage heart failure; "End-stage" means the condition is so severe that all treatments,other than a heart transplant, have failed. Because heart donors are rare, patients who need heart transplants go through a careful selection process. They must be sick enough to need a new heart, yet healthy enough to receive one.

C   Dissertation Organization

The dissertation consists of five chapters. The following remarks summarize the scope of each chapter:

Chapter II overviews the existing computational methods for identifying left ventricle heart pathologies.

Chapter III illustrates the proposed framework for the segmentation of the inner cavity and outer border of the myocardial (LV) wall using graph-cut optimization of a cost function that accounts for the object visual appearance and shape.

Chapter IV illustrates the proposed framework for LV pathology identification and quantification based on a joint MGRF of image and its region map that accounts for the pixel intensities and the spatial interactions between the pixels.

Chapter V concludes the work and outlines the future work.

CHAPTER II

IMAGING THE HEART: SURVEY

Cardiovascular diseases (CVD) are the major cause of death worldwide. Efforts have been made towards diagnosing CVD as early as possible to provide efficient treatments and, hence, significantly decrease its mortality rate [8, 9]. CVD may be identified and localized through the analysis of the cardiac deformation. Especially, analyzing the left ventricle (LV) information is very important as it is the main pumping chamber of the heart. Early efforts for quantifying the ventricular wall motion used to be invasive and impractical, e.g., cardiac catheterization and tracking of implanted markers[10, 11]. Instead, noninvasive imaging techniques have been widely used over the last years to provide noninvasive cardiac imaging methods that delineate cardiac structures and assess myocardial perfusion, function, and metabolism, e.g., echocardiography, nuclear imaging, computed tomography (CT) and cardiac magnetic resonance imaging (CMR) [12], see Fig. 2.
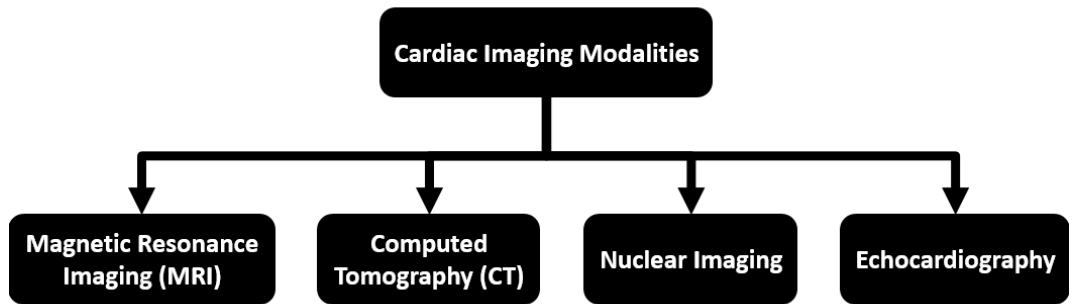
Figure 2. Cardiac imaging modalities.

A   Cardiac Imaging Modalities

1   Echocardiography

Echocardiography, also called cardiac ultrasound, uses standard ultrasound techniques to produce 2D image slices of the heart and/or 1D M-mode echocardiograms that show how the positions of intra-cardiac structures change during the course of the cardiac cycle and permit measurement of cardiac dimensions and motion patterns; see Fig. 3. Moreover, it can also produce accurate assessment of the velocity of blood and cardiac tissue at any arbitrary point using Doppler ultrasound. It possesses unique characteristics like: It is free form ionizing radiation, less expensive than other imaging modalities of similar capabilities, and portable; i.e., can be easily transported to the patient. It also produces images in real time. The many advantages that ultrasound can offer have enabled it to become a valuable diagnostic tool in such medical disciplines as cardiology. Due to its importance, echocardiography is a training that every cardiologist must have [13, 14]. Echocardiography also has several drawbacks:It depends on operator skills, and It is sometimes impossible to obtain good images from certain types of patients, e.g.,obese patients.

Echocardiography has many types [13, 15, 16]:

Transthoracic Echocardiogram (TTE)

In TTE the transducer, probe, is placed on the chest wall, thorax, of the patient and images are taken. It allows non-invasive visualization of the heart and the blood flow through the heart which gives a quick assessment of the overall health of the heart.
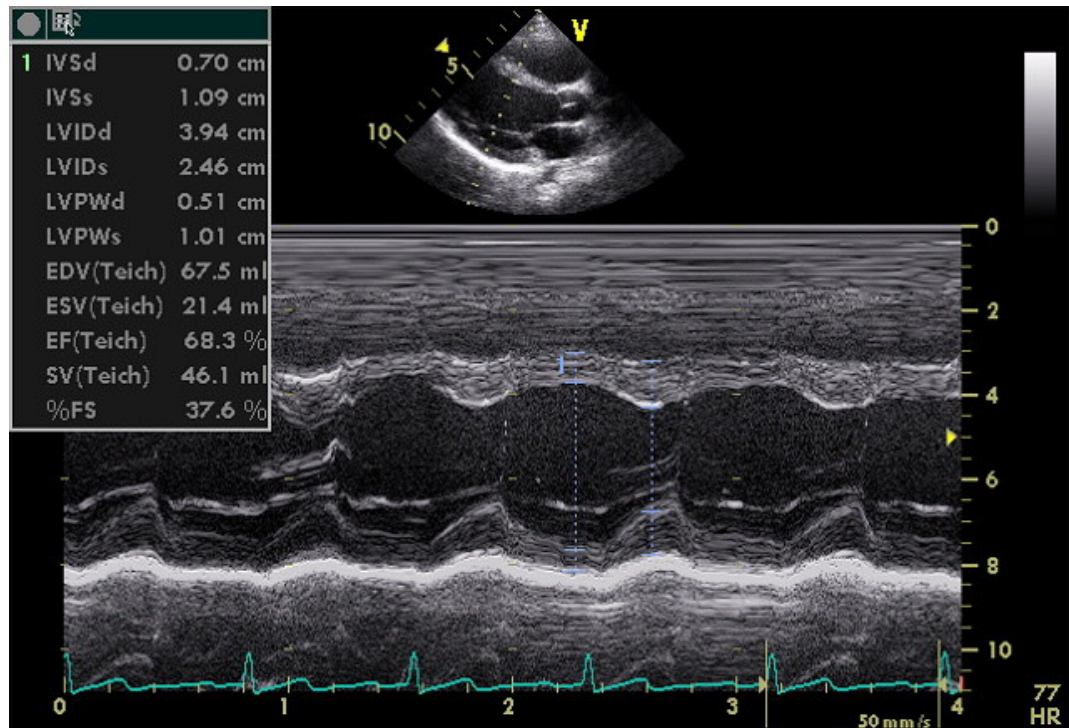
Figure 3. Echocardiogram in the parasternal long-axis view, showing a measurement of the heart's left ventricle. Image from [15].

Transesophageal Echocardiogram (TEE)

This is an alternative way of performing an echocardiogram. A specialized probe containing an ultrasound transducer at its tip is passed into the patient's esophagus. This allows image and Doppler evaluation from a location directly behind the heart.TEEs are mostly used when clearer images are required for assessment.

Stress Echocardiography (SE)

SE utilizes ultrasound imaging of the heart to assess the regional myocardial function in response to physical stress. Images of the heart are taken at rest first to be a baseline of the patient's wall motion at a resting heart rate. Then, the heart is imaged at stress to assess wall motion at the peak heart rate. A stress echo assesses
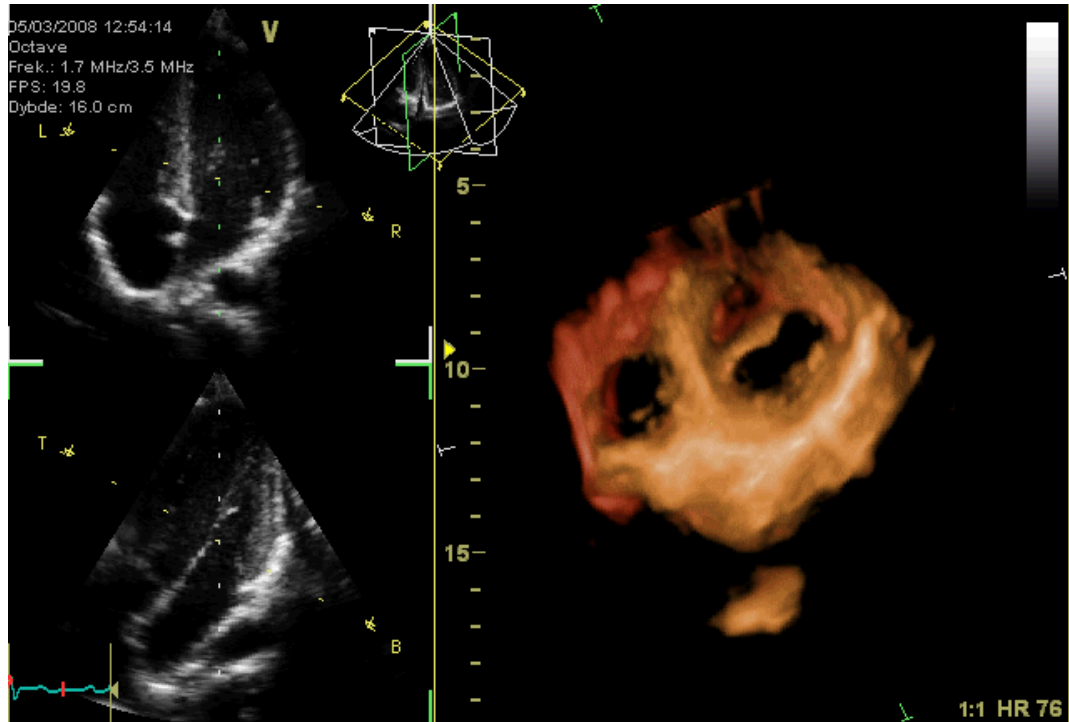
Figure 4. A 3D echocardiogram of a heart viewed from the apex, with the apical part of the ventricles removed and the mitral valve clearly visible. To the left are two standard two-dimensional views taken from the 3D dataset. Image is taken from [15].

wall motion of the heart.

Three-Dimensional Echocardiography (3DE)

3DE is achieved using special ultrasound probe and an appropriate processing system. This enables detailed anatomical assessment of cardiac pathology. Real Time 3DE can be used as a guide in many intraoperative assessments; see Fig. 4.

Contrast Echocardiography

Contrast is used in echocardiography, Contrast-enhanced ultrasound, for the assessment of global and regional systolic function, visualization of wall thickening and for the assessment of blood perfusion throughout myocardium. Contrast agents enhance border detection.
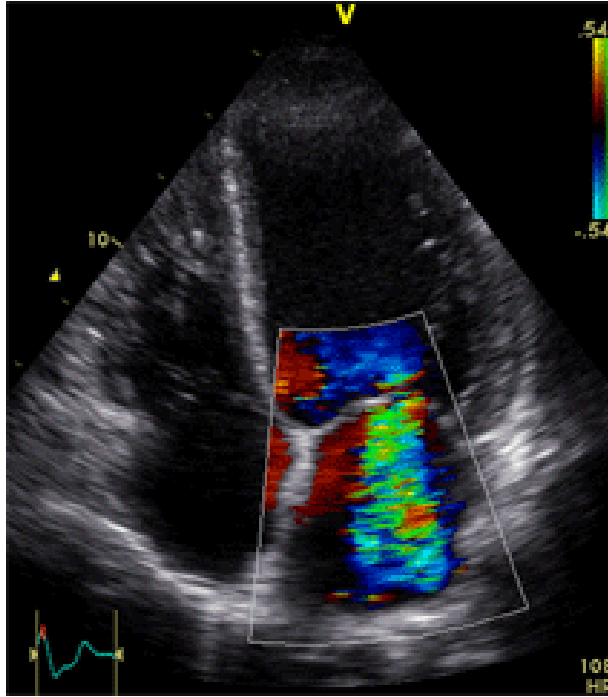
Figure 5. Doppler echocardiogram showing a mid-muscular ventricular septal defect. The trace in the lower left shows the cardiac cycle and the red mark the time in the cardiac cycle that the image was captured. Colors are used to represent the velocity and direction of blood flow. Image from [15].

Doppler Echocardiography

Doppler echocardiography is a method for detecting the direction and velocity of moving blood within the heart, as seen in Fig 5.

2 Computed Tomography (CT)

In a CT scan, an x-ray tube is rotated rapidly around the patient to produce cross-sectional views of the body [2, 4, 17], Fig 6 shows different CT scanning techniques. Cardiac CT is a heart-imaging test that uses CT technology with or without contrast to visualize the heart and its surroundings and assess cardiac structure and function.[2, 4, 17]

Conventional CT

Also called the sequential CT. It involves taking scans slice by slice in a step and shoot mode [2, 17].Here, taking smaller slice thickness allows for better resolution, but this causes increased radiation exposure and scanning time [17].
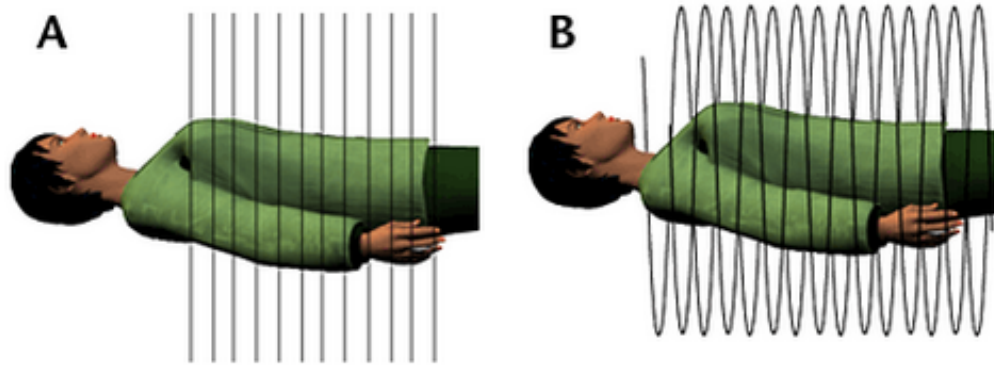
Figure 6. (A) Conventional CT scan, (B) Spiral CT scan; [18].

Electron-Beam Computed Tomography (EBCT)

Also know as ultrafast CT scanners, EBCT is a variation of conventional cross-sectional CT technique. It scans in a step and shoot mode, but instead of using rotating x-ray tube it uses a focused electron beam is created from an electron gun [19, 20]; as seen in Fig 7. It's used to generate cine CT images [20].

SPIRAL CT, Single-Slice CT (SSCT)

Spiral scanners have the ability to rotate an X-ray tube continuously while pushing forward the patient table through the scanning ring creating a 3-D volumetric series. these scanners use one x-ray source and a fan beam; see Fig 8.
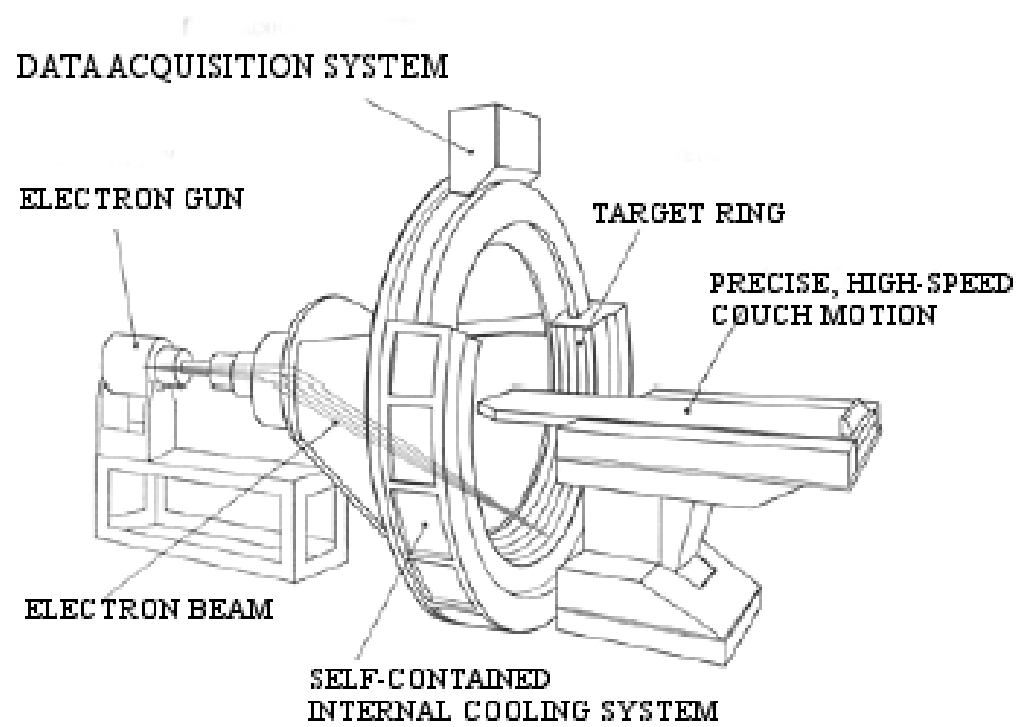
Figure 7. EBCT scanner [21].
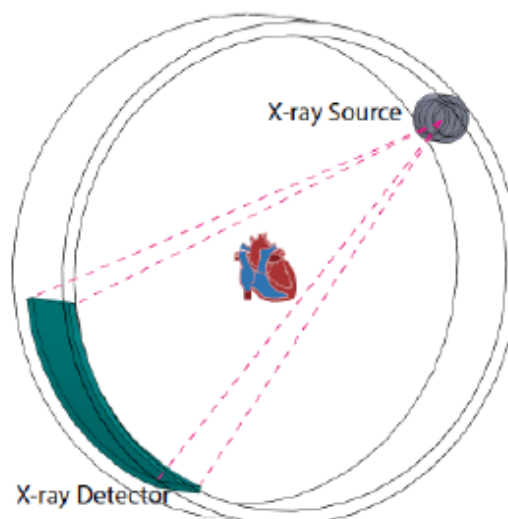
Figure 8. SDCT construction [21].
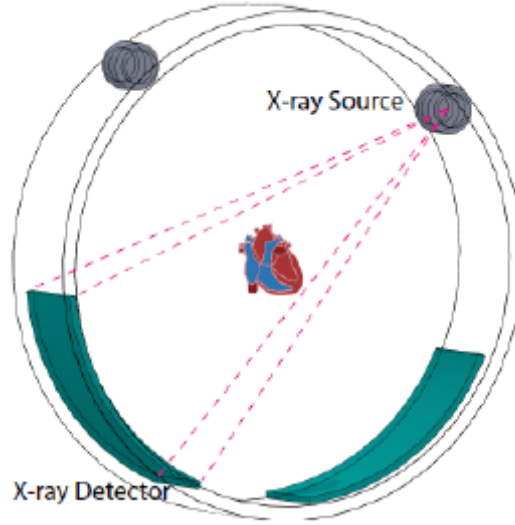
Figure 9. DSCT [21].

Multi-Slice CT (MSCT)

MSCT uses multiple detectors and a cone beam which enables capturing multiple image slices during the rotation of the CT X-ray tube. This capability has sped up the amount of time needed to complete CT scans over that of the spiral scanner [17, 19]; see Fig 10.

Dual-Source CT (DSCT)

The DSCT scanner uses two X-ray sources simultaneously, yielding the best temporal resolution of any of the CT scanners. This allows to perform non-invasive imaging of the structures of the heart at any heart rate [23–25]; see Fig 9.

Base on the fact that structures that attenuate similarly to X-rays producing similar CT numbers at one beam energy may respond differently at another, DSCT can increase the amount of information available from CT imaging by assigning a different energy values for the X-ray tubes, becoming a dual-energy CT.
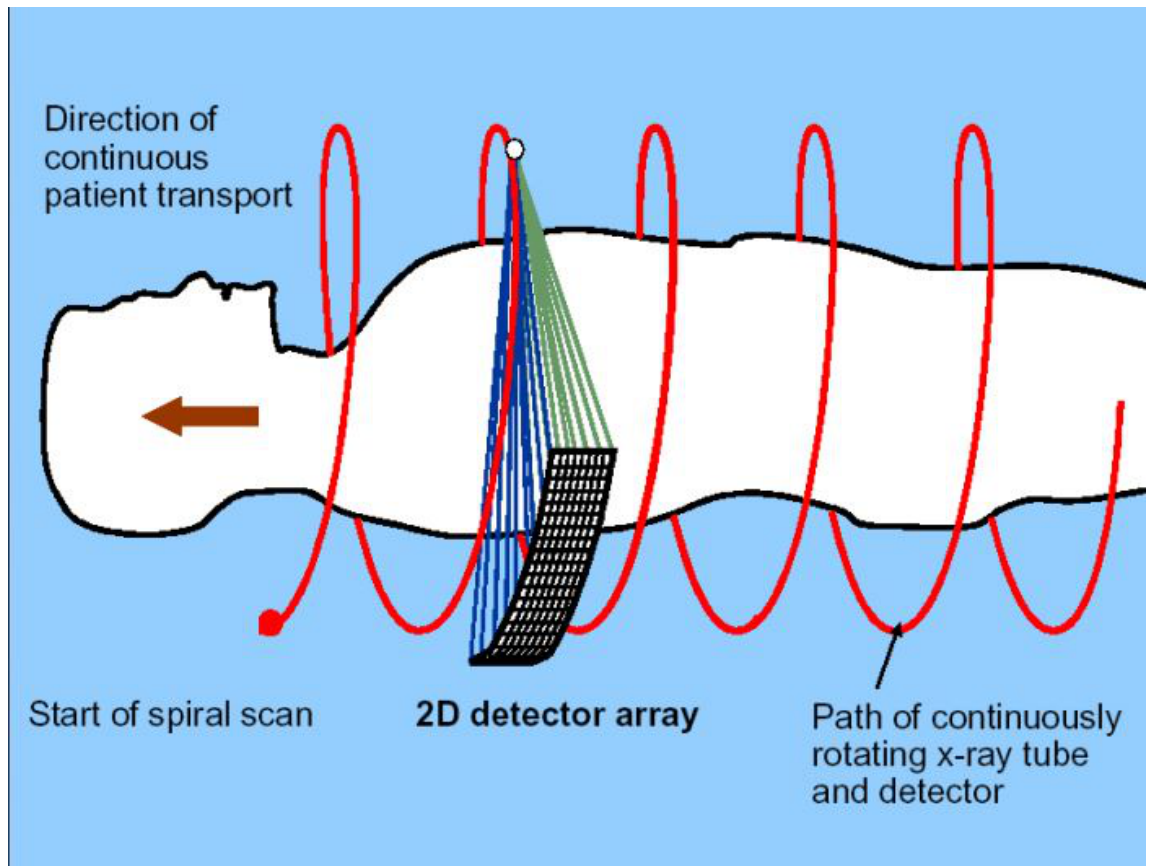
Figure 10. Multi-slice CT.

Disadvantages of CT

Cardiac CT involves ionizing radiation. In general, higher radiation doses result in higher-resolution images. Unfortunately, radiation might lead to cancer [2, 16]. CT contrast medium is potentially nephrotoxic [16]. Contrast medium induced nephropathy is a caveat for cardiac CT in clinical practice. Moreover, obese patients, representing an increasingly prevalent segment, can't undergo a cardiac CT imaging as Image resolution may be deteriorated in them due to the X-ray attenuation.
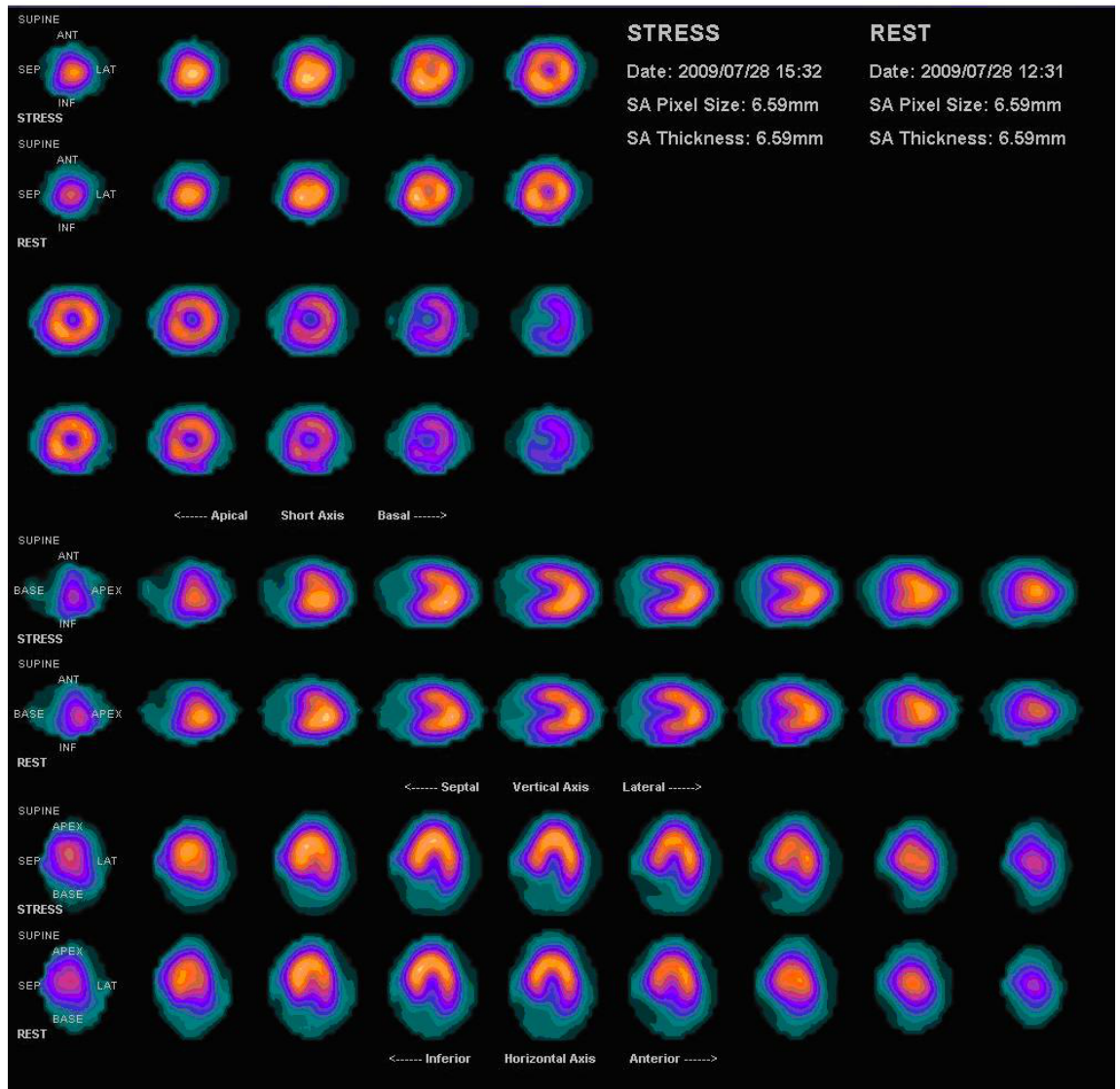
Figure 11. Nuclear cardiac imaging [22].

3 Nuclear Imaging

Nuclear imaging, single photon emission computed tomography (SPECT) and positron emission tomography (PET), utilizes radioactive molecules, inserted in the body by shot, inhaled, or swallowed, that target the heart for the imaging. The nuclear imaging differs from other imaging disciplines in showing functional, metabolic, instead of anatomic information of the heart [26]; see Fig 11. It can be reliably used for myocardial perfusion and viability and with great power predict short- and long-term prognosis [12, 27]. Nuclear imaging suffers from long examination time and poor spatial resolution [26]. Nowadays, hybrid SPECT/CT or PET/CT imaging is used to allow a patient-friendly image acquisition in only one visit while combining the information of both modalities [12].

4 CMR

While there are competing modalities for every clinical application of CMR, there is no one modality that can provide a comprehensive evaluation like CMR [28]. CMR is a very versatile technique that generates a great variety of image contrasts for a wide range of clinical and research applications with no or little modifications to the imaging equipment [29, 30]. Based on the accurate and reproducible anatomical and functional information provided by CMR, physicians can determine appropriate therapeutic procedures [31–33].CMR allows studying different aspects of the heart anatomy and function depending on the acquisition settings, providing complementary data.

The advantages of CMR are [16, 34]:

- It is noninvasive, accurate and versatile.

- It lacks ionizing radiation.

- It has the highest spatial resolution compared to other imaging modalities.

- It is capable of visualizing cardiac events in near real time cine mode.

- It captures high quality images.

- It can diagnose a broad range of conditions, including cardiovascular anatomical anomalies, functional abnormalities, tumors and conditions related to coronary artery disease.

- The contrast material used in exams is less likely to produce an allergic reaction than the iodine-based contrast materials used for conventional X-rays and CT scanning.

CMR also provides excellent dynamic and quantitative information on cardiac function and on cardiac chamber blood flow. It can also be effective in detecting myocardial infarcts, which can be valuable in the evaluation of myocardial viability for planning the treatment of CAD [23].

On the other hand, CMR is contraindicated in a substantial number of patients for various reasons [34–36]:

- If the patient has any type of medical implants.

- If the patient is Large and can't fit into the bore of the MRI device.

- If the patient is Claustrophobic.

- If the patient is unable to lie still; movements degrade the taken images quality.

- If the patient undergone a surgery in the previous 6 weeks.

Cine CMR

Cine CMR acquires images at each stage of the cardiac cycle. Cine CMR can discriminate very well between blood and myocardium and is capable of extracting
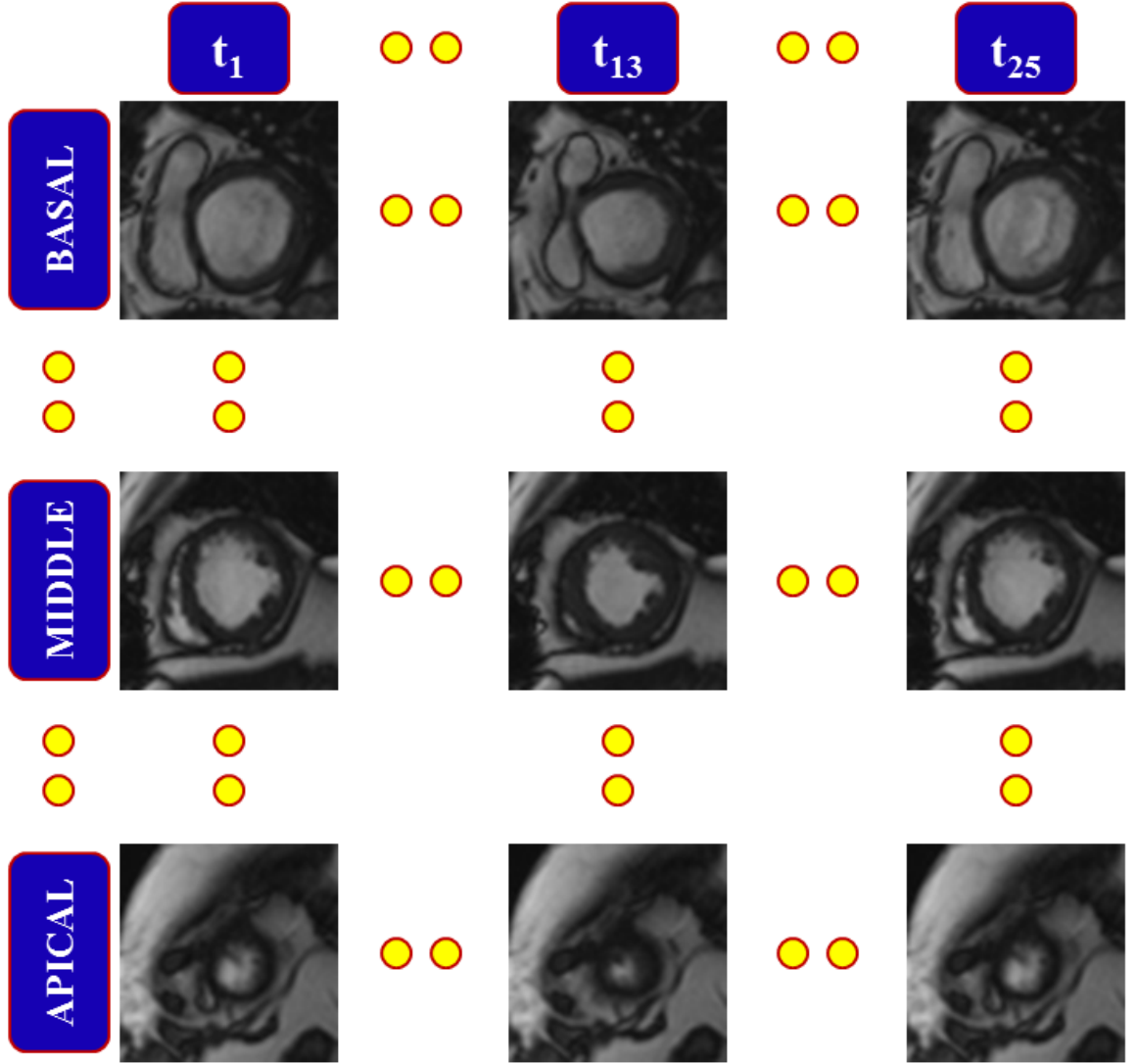
Figure 12. Cine CMR output. The images shown row-wise are from the basal, middle and apical slices, respectively.

multiple diagnostic performance indices [37]. An example of the cine images is introduced in Fig 12

Tagged CMR

Tagged CMR (tCMR) asses the myocardial contractility through capturing tissue displacement which detects non-functioning myocardium. First, a grid of dark

lines is superimposed across the first cine CMR image. Then, these tags subsequently deform through the cardiac cycle allowing the estimation of regional myocardial strain [37–40]. This can be seen in Fig 13.
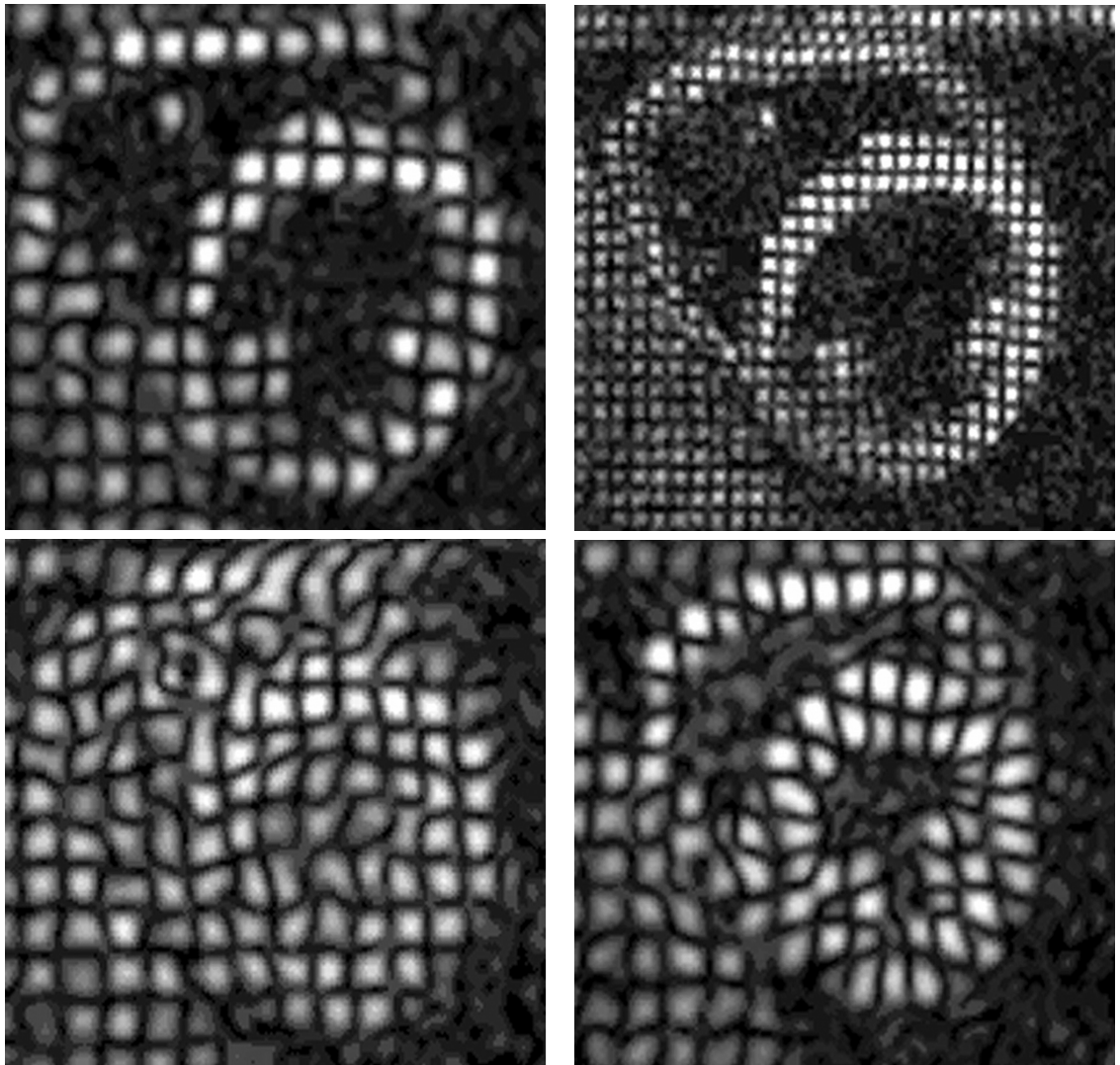
Figure 13. Tagged cine images of the Heart. Images are taken from [41].

Velocity-Encoded Phase Contrast CMR:

Phase contrast CMR (pcCMR) can be used to translate the instantaneous flow information, strain rate and shunt volume. Unlike doppler ultrasonography, pcCMR is not limited by acoustic windows[37, 42–44]. Images from pcCMR can be seen in Fig 14.
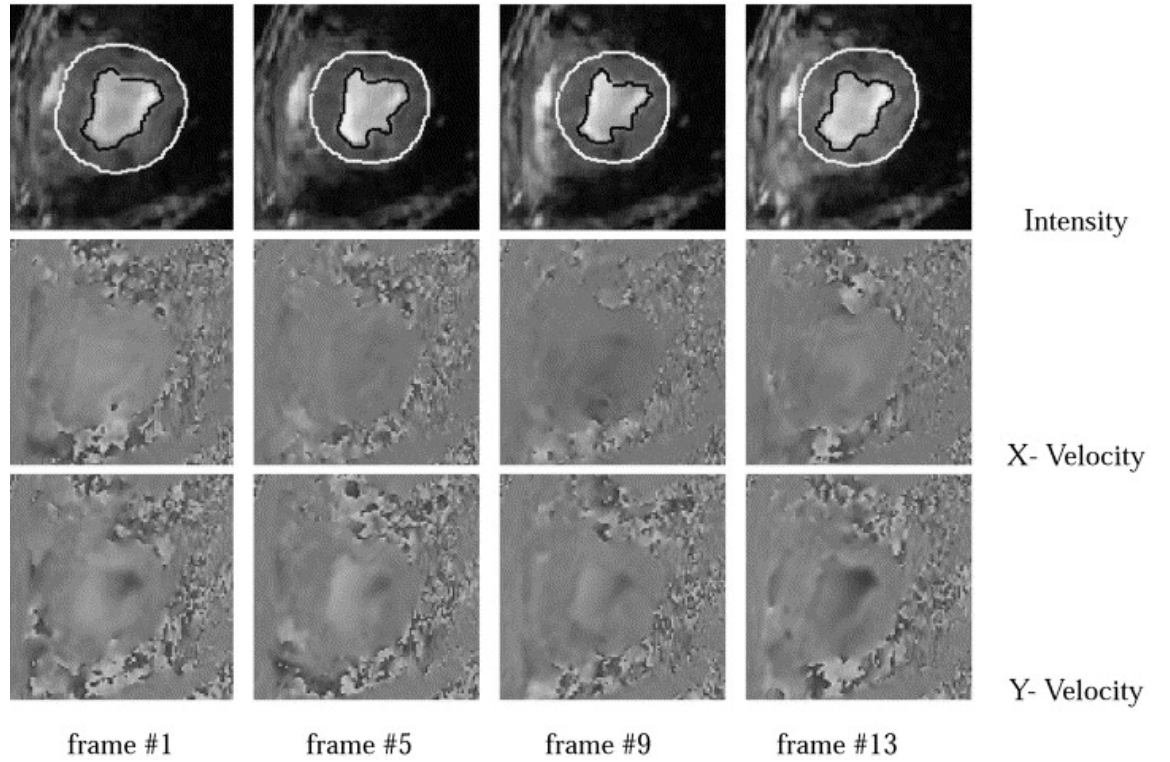
Figure 14. Short-axis velocity encoded pcCMR images, x-velocity and y-velocity image sequences throughout cardiac cycle [43].

Contrast-Enhanced CMR (CE-CMR):

Although structural CMR provides excellent soft tissue contrast, it lacks functional information. Contrast-enhanced CMR (CE-CMR) is a special MR technique that has the ability to provide superior information of the anatomy,

function, and metabolism of target tissues [45]. The technique involves the acquisition of MR images with high temporal resolution before, during, and at several times after the administration of a contrast agent into the blood stream. In CE-CMR, the signal intensity in target tissue changes in proportion to the contrast agent concentration in the volume element of measurement, or voxel. CE-CMR is commonly used to enhance the contrast between different tissues, particularly normal and pathological. Typical examples of CE-CMR time series data of the heart is shown in Fig. 15.

CE-CMR has gained considerable attention due to the lack of ionizing radiation, and increased spatial resolution. It has been extensively used in many clinical applications, including detection of pathological tissue in the myocardium and early detection of acute renal rejection [46]. The most successful MRI contrast agents that have been widely investigated are gadolinium-based. Gadolinium, a rare metal, is a non-toxic paramagnetic contrast agent that enhances the detected MR signal and produces high contrast images of soft tissues by decreasing T1 relaxation times of water protons in living tissue in the vicinity of the paramagnetic contrast agent. Gadolinium-based CE-MRI has been extensively used in cardiovascular imaging applications [47].

Late Contrast-Enhanced CMR (LCE-CMR)

LCE-CMR distinguishes infarct from viable myocardium [48]. The viable parts appear dark in the LCECMR images, while the defected parts appear bright white. The improved spatial resolution of MR imaging provides clear advantages such that MR imaging is considered by some to outperform other modalities [49]. Images from LCE-CMR can be seen in Figs 15,16.

Pre-Contrast   **Post-Contrast**   **Late-Contrast**
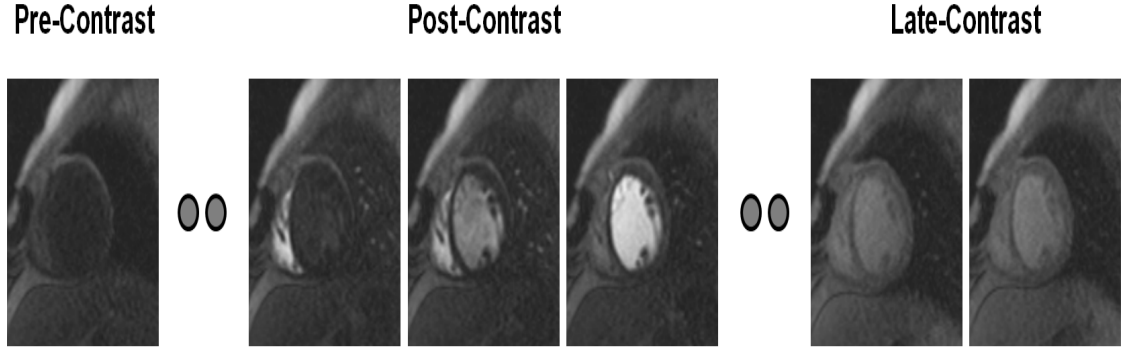
Figure 15. CMR heart images taken at different time points post the adminstration of the contrast agent showing the change of the contrast as the contrast agent perfuse into the heart tissues. It starts in the right ventricle, followed by the left ventricle, and ending with a progressive myocardial enhancement.

Dynamic Contrast-Enhanced CMR(DCE-CMR)

Conventional CE-CMR displays a single snapshot of the scanned body area after the adminstration of the contrast agent. Although the anatomical information derived from such images is valuable, it lacks functional information. Dynamic contrast-enhanced CMR (DCE-CMR) has emerged as an MR imaging technique that has the ability to yield superior anatomical and functional information about the heart tissue [45]. This CMR technique has gained considerable attention because of its ability to yield information about the hemodynamic (i.e., perfusion) properties of tissues (blood flow, blood volume, mean transit time), micro-vascular permeability, and extracellular leakage space. DCE-CMR helps guide intervention and treatment for coronary artery narrowing and has been identified as a promising approach for preliminary detection of CAD [51, 52].

The technique involves the acquisition of serial MR images with high temporal resolution before, during, and at several times after the administration of a contrast agent. The signal intensity in target tissue will change in proportion to the contrast agent concentration in the volume element of measurement. DCE-CMR is commonly used to enhance the contrast between different tissues, particularly
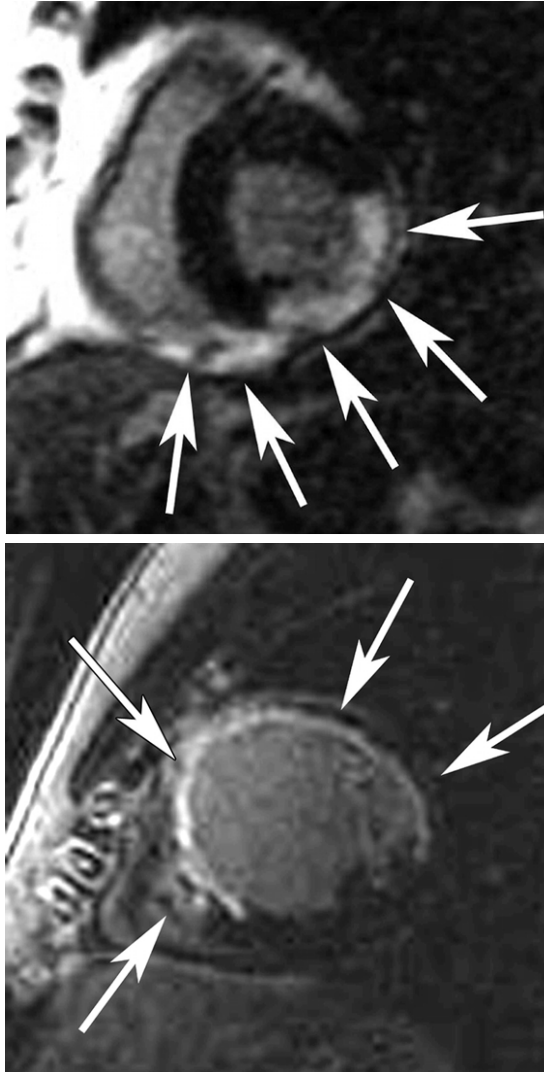
Figure 16. Short-axis LCE-CMR images; arrows point to defected myocardium. Images are taken from [50].

normal and pathologic. The enhancement kinetics and the pattern of enhancement can be used to improve the diagnostic specificity of suspicious lesions. A typical example of DCE-CMR time series data of the heart is shown in Fig. 15.

In general, DCE-CMR poses multiple challenges stemming from (i) the need to image very quickly, to capture the transient first-pass transit event, while maintaining adequate spatial resolution, (ii) varying signal intensities over the time course of agent transit, (iii) variations of the target object shape changes due to patient motion, breathing, heart contraction, and other pulsatile or transmitted effects from adjacent structures, such as bowels.

All in all, MRI potential advantages include:

- MRI does not involve exposure to any harmful radiation,

- MRI can be repeated sequentially over time, and has the ability to generate cross-sectional images in any plane (including oblique planes).

- MRI has the ability to distinguish the differences between two arbitrarily similar but not identical tissues

- MRI plays an important role in assessing tumors locations and extent, directing biopsies, planning proper therapy, and evaluating therapeutic results.

On the other hand, MRI imaging modality has its own disadvantages:

- MRI data acquisition is a relatively long and complex process,

- For each scan the imaging parameters and the pulse sequence need to be fixed,

- MRI is not suitable for patients with metal implants due to its magnetic nature,

- MRI suffers from sensitivity to noise and image artifacts,

- MRI signals are dependent on the imaging sequence used and can become non-linear beyond certain concentrations leading to errors in extracted physiology,

- MRI scanning processes may be uncomfortable for some people because it noisy and it can produce claustrophobia. Recent improvements in MRI design alleviates this by using more open magnet designs and shorter exam times while sacrificing some of the image quality.

5   Quantifying the Heart Status

Different metrics can be extracted to quantify the Heart Status, especially the LV functionality, and detect any local and global cardiac diseases using MRI, such as the functional indexes. This can help cardiologists to accurately quantify the heart status and detect local and global cardiac diseases, e.g., the EF metric and the functional strain. The EF is a clinically relevant and well-documented global indicator of the LV function in terms of the total cavity volume (the LV volume variation over time): where ESV and EDV are the end systolic (the smallest cavity area) and the end diastolic (the greatest cavity area) volumes, respectively.

To estimate the EF, the LV cavity volume-time data at each image slice is used. Following the delineation of the cavity contour at each time point (image frame) of the cardiac cycle, the corresponding cavity areas are computed and a curve representing the physiology over the cardiac cycle is constructed. Then, the Simpsons rule is used to estimate the total LV volume by summing the contributions of enclosed areas from the individual image slices. From the total ventricular function curve, the EDV and ESV can be automatically extracted and hence calculate the EF.

On the other hand, Wall thickness and functional strain are used to detect local wall function. The Wall thickness is measuring the distance between the inner and outer borders of the LV wall in order to assess the regional function of the

myocardium and is found to be more accurate than wall motion analysis in detecting dysfunctional myocardium. It is typically assessed by visual inspection, which is preferred clinically for practical purposes [53, 54]. The functional strain is also used to detect any cardiac wall dysfunction that manifests on strain slopes during the contraction and expansion phases of the cardiac cycle [55]. Traditionally, the functional strain is estimated by using the tagged images that lead to errors between the estimated indexes due to the inter-slice variability between the different image modalities.

CHAPTER III

MYOCARDIAL BORDERS SEGMENTATION FROM CINE MR IMAGES USING DEFORMABLE MODELS

A   Introduction

Accurate extraction of the myocardium from cine cardiac magnetic resonance (CMR) images is an essential step for the quantification of the heart function by estimating global (e.g., stroke volume (SV), end-systolic volume (ESV), end-diastolic volume (EDV), and ejection fraction (EF)) and local (e.g., wall thickening) performance indexes. These indexes help cardiologists in accurately quantifying the heart status. The segmentation problem of the left ventricle (LV) wall is being extensively investigated. However, segmentation of the LV wall is a challenging task due to many reasons: *(i)* poor image quality and noise due to patient movement, respiration motion, and artifacts from the moving blood within the ventricular cavity; *(ii)* shape-deformations and intensity-variations of the LV at different image slices and within the same slice over the cardiac cycle; *(iii)* partial influence of adjacent structures, such as the diaphragm; *(iv)* irregularities and protrusions of papillary muscles (PM) structures in the cavity boundary; and *(v)* the lack of strong edges between the epicardium and the surrounding structures.

Traditionally, the segmentation of the left ventricle (LV) wall contours is performed manually [56, 57]. However, it is prohibitively time consuming, labor-intensive, and is prone to intra- and inter-observer variability [58]. To avoid the manual procedure shortcomings, several semi-automated and automated techniques have been proposed for the delineation of the LV wall. Below we will

present an overview of the related work on cine CMR image segmentation.

1 Semi-automated Methods

In order to address the above-mentioned challenges, many semi-automated techniques for the extraction of the LV wall borders have been proposed [59–65]. For example, Ben Ayed et al. [59, 60] proposed a semi-automated approach for the segmentation of the LV using a variational deformable model-based approach to minimize an energy functional containing a similarity/dissimilarity overlap constraint, measured by the Bhattacharyya coefficient. A semi-automated framework to extract the myocardium was proposed by Li et al. [61]. Their framework employed two energy functionals, each represented by a weighted sum of edge-, region-, and shape-based features, for segmenting the endo- and the epi-cardiums. Feng et al. [62] developed a geometry-independent dual-contour propagation technique to segment the myocardium. The LV endocardial contours were manually drawn at end systole and end diastole. Their dual-contour propagation technique showed promising results for the exclusion of the PM from the LV wall, more accurate than single-contour propagation. Chen et al. [63] proposed a hybrid semi-automated framework to segment the LV wall borders using variational level sets. The myocardium is separated from the background, in a user defined region-of-interest (ROI), based on the difference in their intensity distributions. The deformable model evolution was derived by minimizing an energy function consisting of regional and edge-based information. Pednekar et al. [64] proposed an intensity-based segmentation approach that uses circular Hough transform to estimate the LV borders in CMR images. Uzümcü et al. [65] proposed a semi-automated method that is based on a multidimensional dynamic programming (DP), which is applied to a parametric shape model instead of applying it directly to image data. Please see Petitjean and Dacher [66] for a more comprehensive review of semi-automated methods for cardiac image segmentation.

2 Automated Methods

The challenging problem of the LV wall borders segmentation has also been addressed using automated techniques [9, 67–69, 72, 74–78, 80–90]. In particular, Khalifa et al. [67–69] presented an automated level set-based framework for the segmentation of the myocardial borders on cine CMR images. They used a stochastic force that accounts for a binary joint Markov-Gibbs random field (MGRF) image model of the LV and its background to constrain the evolution of the deformable contour. O'Brien et al. [70] proposed a model-based technique for the LV segmentation on cardiac MR image. An active shape model (ASM) was employed for statistical modeling of the LV shape and separate models for spatial and temporal variation were used. Cousty et al. [71] proposed a segmentation framework based on discrete mathematical morphology and spatiotemporal watershed transforms to segment the endocardium and the epicardium separately. Zhang et al. [72] proposed a segmentation approach based on a combination of an ASM and an active appearance model (AAM) to segment the LV wall using short- and long-axes CMR data. A refinement step followed by using a reversed 3D ASM model to achieve better cardiac motion tracking as well as improved shape details. Andreopoulos et al. [73] achieved LV segmentation using statistical models of shape and appearance. Their method employed fitting of a 3D AAM on short axis cardiac MR images followed by hierarchical 2D + time ASM to refine segmentation. Jolly et al. [74] proposed an automated framework based on deformable registration for the LV segmentation. Candidate contours of each slice are obtained in the average image of the co-aligned time frames using the shortest paths, and a minimal surface is built to generate the final contours. Kurkure et al. [75] proposed a hybrid segmentation approach that integrates intensity- and texture-based information for the extraction of the myocardium, LV blood pool, and other adjacent structures, e.g., lungs and liver. A DP-based boundary detection method was used to delineate the LV myocardial contours. A fully automated approach for LV segmentation was

proposed by Schllhuber [9]. A ROI covering the heart was located by a hierarchical pattern matching algorithm. Motion artifacts are minimized by image registration using mutual information (MI). Cocosco et al. [76] proposed an automated approach for the segmentation of the LV on cardiac images based on binary classification within a predefined ROI to segment the blood pool. Lynch et al. [77] presented an automated level-set scheme for the segmentation of CMR data using prior knowledge of the temporal deformation of the myocardium. Liang et al. [78] proposed an automated approach using the radial GVF [79] and the Hough transform to segment the LV contours. Zhuang et al. [80] proposed a framework to propagate the labels in a heart atlas to the CMR images for ventricle segmentations based on image registration. Their method employed anatomical information from the atlas as priors to constrain the registration. To improve the quality of segmentations obtained by the AAMs on CMR data, Zambal et al. [81] combined a set of local 2D AAMs with a global shape model. Their method propagates the position and size of the basal slices to apical ones and keeps the global shape characteristics plausible. Lynch et al. [82] presented a coupled level-set segmentation of the LV of the heart using a priori information. Two fronts representing the epi- and endo-cardium boundaries of the LV are evolved using both gradient and region-based information. The segmentation is supervised with a coupling function and a probabilistic model built from training instances. An approach relying on morphological operations is proposed by Katouzian et al. [83]. For endo-cardium segmentation, the edge detection is performed and the PM are excluded via a convex-hull method. The epicardial boundary is delineated through a threshold decomposition opening approach. Jolly et al. [84, 85] introduced an automated LV segmentation technique to extract the myocardium using Gaussian mixture models and Dijkstra active contours. Lynch et al. [86] introduced an automated framework for the segmentation of the LV of the heart using clustering and cardiac anatomy knowledge. Lelieveldt et al. [87] proposed a multiview AAM for the segmentation of

multiple views in long- and short-axis CMR images. Fu et al. [88] developed a wavelet-based image enhancement technique to enhance the LV wall borders profiles as the pre-processor for a DP-based automatic border detection algorithm. Lalande et al. [90] applied fuzzy logic-based automatic contour detection for the identification of the LV wall borders in short-axis CMR images. A variational coupled level set approach that combined boundary and region-based information to segment the LV borders was introduced by Paragios [91]. They introduced an anatomical module to constrain the relative positions of the endocardium and epicardium interfaces and to enforce an intensity consistency over the temporal cycle. A 3-D graph-based simultaneous multi-object segmentation proposed by Song et al. [92] incorporates both shape and context prior knowledge to segment, e.g., intraretinal layers from optical coherence tomography images, and prostate and bladder from 3-D CT images. State-of-the-art automated techniques for cardiac image segmentation are detailed in the recent review by Petitjean and Dacher [66].

To summarize, the segmentation of cine CMR images has been the subject of extensive research in the last few years. Several semi-automated and automated segmentation methods have been developed. However, the known methods have the following limitations: *(i)* some techniques require intensive manual training; *(ii)* most of them are computationally expensive; *(iii)* parametric shape-based approaches depend on the existence of good texture features in cardiac images and perform poorly on some slices due to noise and lack of well-defined features; and *(iv)* the accuracy of the knowledge-based approaches (e.g., deformable models that are based on shape priors) depends on the size of the training data and the accuracy of the alignment.

To overcome these limitations, we propose a novel approach to segment the LV wall borders from short-axis cine CMR images, which exploits bi-directional coupled parametric deformable models. Control points of these models are tracked with a conventional internal force in addition to a novel external force. This force

incorporates the first– and second–order visual appearance features of cine CMR images, as well as a new coupling factor. The latter prevents the overlap between the inner and outer borders of the LV wall in order to preserve the heart topology. Unlike other existing methods, our approach needs neither shape prior, nor training. All parameters, which are used to construct and evolve the deformable models, are estimated from the input data.

This chapter is organized as follows. The above overview (Section A) of the related work on cardiac image segmentation is followed in Section B by details of the proposed approach. Section C discusses metrics used to evaluate performance of our segmentation. Medical data used in this study, experimental results, and clinical applications of the proposed segmentation are presented in Section D. Conclusions are given in Section E.
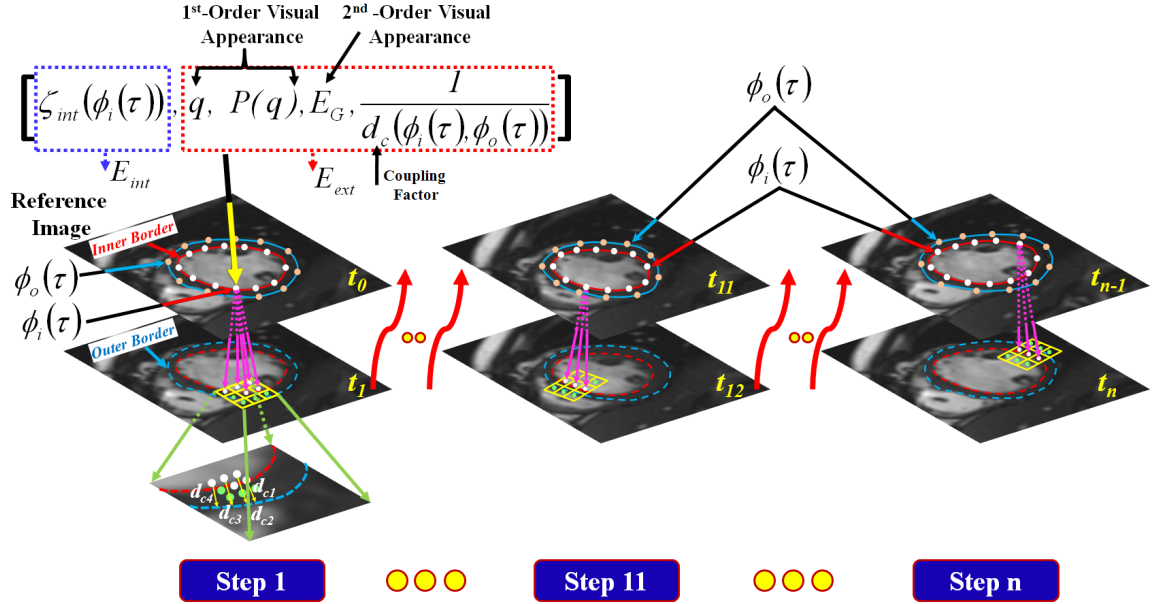
Figure 17. Tracking control points of the deformable models at different time frames of the cardiac cycle. Note that each deformable model was initialized using 20 points.

B   Methods

A 2D parametric deformable model is a curve
$\Phi = (\phi(\tau) = (x(\tau), y(\tau)); \tau \in T)$ in planar Cartesian co-ordinates (x, y) where $\phi(\tau)$
denotes the inner $(\phi_i(\tau))$ or outer $(\phi_o(\tau))$ control points of the deformable models, τ
is the continuous or discrete index of a contour point, and T is the index range,
$T = [0, 1]$. The inner deformable model moves through the spatial image domain to
minimize the total energy [93], in addition to a coupling factor $\frac{1}{d_c(\cdot,\cdot)}$:

$$
\begin{aligned}
E_i &= E_{\text{int}} + E_{\text{ext}} + \text{coupling factor} \\
&= \int_{\tau \in T} \xi_{\text{int}}(\phi_i(\tau)) + \xi_{\text{ext}}(\phi_i(\tau)) + \frac{1}{d_c(\phi_i(\tau), \phi_o(\tau))} d\tau
\end{aligned}
\tag{1}
$$

where $\xi_{\text{int}}(\phi_i(\tau))$, $\xi_{\text{ext}}(\phi_i(\tau))$ and $\frac{1}{d_c(\phi_i(\tau), \phi_o(\tau))}$ denote, respectively, internal and
external forces that control the point-wise model movements, and a coupling factor
represented by the distance between the inner border control points $\phi_i(\tau)$ and outer
border control points $\phi_o(\tau)$ to preserve the heart topology (see Fig. 17). The
internal energy keeps the deformable model as a single unit. The internal force is
typically defined as $\xi_{int}(\phi_i(\tau)) = \alpha|\phi_i'(\tau)|^2 + \beta|\phi_i''(\tau)|^2$ where weights α and β
control the curve's tension and rigidity, respectively (for all experiments, we use
$\alpha = 1$ and $\beta = \frac{1}{3}$), and $\phi_i'(\tau)$ and $\phi_i''(\tau)$ are the first and second derivatives of $\phi_i(\tau)$
with respect to τ. In a similar way, the energy of the outer deformable model, E_o, is
calculated. Typical external forces to lead an active contour toward step edges in a
greyscale image $\mathbf{g}$ (e.g., designed by Kass et al. [93], or other traditional forces
based on lines, edges, GVF, etc.) are not suitable to track the control points of a
deformable model from one image frame to another. To overcome these drawbacks,
we propose a novel external force that integrates both first-and second-order
appearance features of the cine images to track the evolution of the control points.

1 Second-Order Features of Visual Appearance

The 2D visual appearance of the LV wall in cine CMR images is modeled with a generic translation and rotation invariant second-order MGRF. Before describing the MGRF model of LV wall, let us define the following basic notation:

- $\mathbf{R} = [(x, y) : x = 0, \ldots, X - 1; y = 0, \ldots, Y - 1]$ is a 2D lattice supporting 2D images $\mathbf{g} = [g_{x,y} : (x, y) \in \mathbf{R}; g_{x,y} \in \mathbf{Q}]$ with a finite set of intensities $\mathbf{Q} = \{0, \ldots, Q - 1\}$.

- $\mathbf{N}$ is an index set of characteristic translation-rotation invariant central-symmetric pixel neighborhoods $\{\mathbf{n}_\nu : \nu \in \mathbf{N}\} on \mathbf{R}$, illustrated in Fig. 18.

- $\mathbf{C}_\nu = \{\mathbf{c}_\nu : \nu \in \mathbf{N}\}$ is a family of pairwise cliques forming the translation-rotation invariant neighborhoods indexed by $\nu \in \mathbf{N}$.

- $\mathbf{V}_\nu = [V_\nu(\Delta) : \Delta \in \mathbf{D}]^\mathsf{T}$, where T indicates the vector-matrix transposition, is the vector of values of a Gibbs potential for the cliques of the family $\mathbf{C}_\nu$. The potential is a scalar function $V_\nu : \mathbf{D} \to (-\infty, \infty)$ with only finite values, i.e. $-\infty < V_\nu(d) < \infty$, depending on integer arguments from the set $\mathbf{D} \equiv \mathbf{Q} = \{0, 1, \ldots, Q - 1\}$ of absolute pairwise signal differences.

A generic translation and rotation invariant second-order MGRF of images $\mathbf{g}$ has the following Gibbs probability distribution [94]:

$$P(\mathbf{g}|\mathbf{V}) = \frac{1}{Z_\mathbf{V}} \exp \left(|\mathbf{R}| \sum_{\nu \in \mathbf{N}} \rho_\nu \mathbf{V}_\nu^\mathsf{T} \mathbf{F}_\nu(\mathbf{g}) \right) \tag{2}$$

where $Z_\mathbf{V}$ is the normalizing factor (depending on the potentials $\mathbf{V} = [\mathbf{V}_\nu : \nu \in \mathbf{N}]$ for a chosen system of neighborhoods $\mathbf{N}$); $\rho_\nu = \frac{|\mathbf{C}_\nu|}{|\mathbf{R}|}$ is the relative size of the clique family with respect to the lattice cardinality $|\mathbf{R}|$, and $\mathbf{F}_\nu(\mathbf{g}) = [f_\nu(\Delta|\mathbf{g}) = \frac{|\mathbf{C}_{\nu:\Delta}(\mathbf{g})|}{|\mathbf{C}_\nu|}; \sum_{\Delta \in \mathbf{D}} f_\nu(\Delta|\mathbf{D}) = 1]$ is the vector of relative
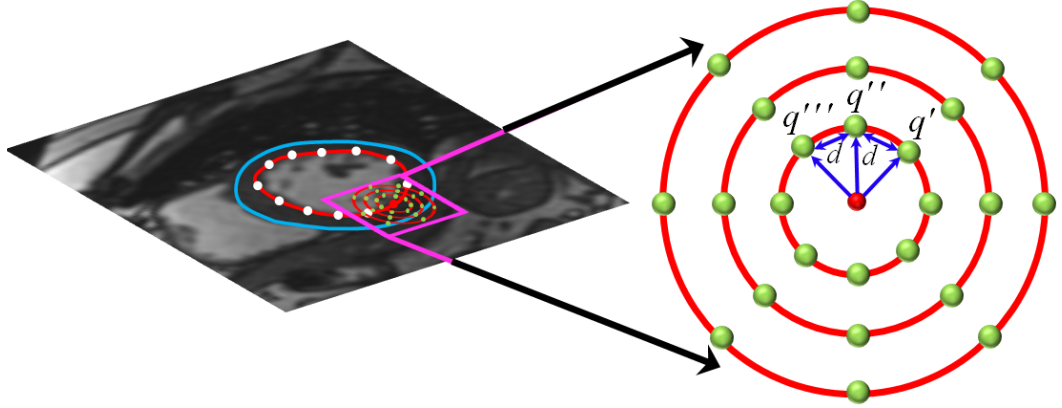
Figure 18. Central-symmetric second-order 2D neighborhood system.

frequencies, or empirical probabilities of absolute signal differences $\Delta \in \mathbf{D}$ in the cliques from the family $\mathbf{C}_\nu$ for an image $\mathbf{g}$. The subfamily $\mathbf{C}_{\nu:\Delta}(\mathbf{g})$ contains all the cliques of this family, such that $|g(x,y) - g(x',y')| = \Delta$.

The central-symmetric pixel neighborhood $\mathbf{n}_\nu$ embraces all pixel pairs such that the coordinate offsets between any pixel (x,y) and its neighbor (x',y') belong to an indexed semi-open interval $(d_{\nu,\min}, d_{\nu,\max})$; $\nu \in \mathbf{N} \subset \{1,2,3,\ldots\}$ of the inter-pixel distances. Figure 18 illustrates the neighborhoods for the distance ranges $d_{\nu,\min} = \nu - 0.5$ and $d_{\nu,\max} = \nu + 0.5$; $\nu \in \mathbf{N} = \{1,\ldots,4\}$. Each neighborhood $\mathbf{n}_\nu$ has the same potential function $\mathbf{V}_\nu$ of the absolute intensity difference $\Delta = |g(x,y) - g(x',y')|$ between the neighboring pixel pairs: $\mathbf{V}_\nu = (V_\nu(\Delta) : \Delta \in \mathbf{D})$. The pixel-wise potential $\mathbf{V}_{\text{pix}} = (V_{\text{pix}}(q) : q \in \mathbf{Q})$ depends on the pixel intensities.

To estimate the potentials of the MGRF, we use the analytical maximum likelihood approach proposed by El-Baz et al. [95–97]. Unlike more traditional ones, like e.g. in [99], learning MGRF models of the whole object appearance, we propose to learn the current appearance of each control point of the deformable model in order to track it from one frame to another. The potentials are analytically approximated just as in [95–97]: $V_\nu(\Delta) = \lambda\left(f_\nu(\Delta) - f_{\text{irf}}(\Delta)\right)$; $\nu \in \mathbf{N}$. Here, $f_\nu(\Delta)$ is the empirical probability of the pairwise intensity difference Δ for the pixel pairs

corresponding to the neighborhood $\mathbf{n}_\nu$ over the starting data set (i.e., the very first image frame, where the contours are manually initialized) and $f_{\text{irf}}(\Delta)$ denotes the probability of the same difference Δ for the independent random field of equiprobable intensities, i.e., $f_{\text{irf}}(\Delta) = \frac{1}{Q}$ if $\Delta = 0$ and $f_{\text{irf}}(\Delta) = \frac{2(Q-\Delta)}{Q^2}$ otherwise. The common factor λ is also computed analytically, but below it is omitted ($\lambda = 1$) because only relative potentials are used for computing relative energies $E_{\nu,\text{rel}}$ of the neighborhoods. The energy at location (x, y) in the image is given by:

$$E_G(g_{x,y}) = \mathbf{V}_{\text{pix}}^\mathsf{T} \mathbf{F}_{\text{pix}}(g_{x,y}) + \sum_{\nu \in \mathbf{N}} \rho_\nu \mathbf{V}_\nu^\mathsf{T} \mathbf{F}_\nu(g_{x,y}) \tag{3}$$

2   First-Order Feature of Visual Appearance

In addition to the second-order visual appearance model, the 1D empirical marginal grey level distributions inside and outside of an initial deformable boundary are approximated with linear combinations of discrete Gaussians (LCDG) [98, 100] in order to more accurately account for changes in the current image appearance. In contrast to a conventional mixture of Gaussians, one per region, the LCDG model approximates the mixed marginal intensity distribution for the whole image more closely. Then, it can be easily partitioned into the like LCDG submodels relating to each dominant mode in the mode in the mixture. The discrete Gaussians are differences between successive values of a cumulative Gaussian probability function Φ_θ with a shorthand notation $\theta = (\mu, \sigma^2)$ for the mean, μ, and the variance, σ^2:

$$\psi(q|\theta) = \begin{cases} \Phi_\theta(0.5) & \text{for} \quad q = 0 \\ \Phi_\theta(q + \frac{1}{2}) - \Phi_\theta(q - \frac{1}{2}) & \text{for} \quad q = 1, \ldots, Q - 2 \\ 1 - \Phi_\theta(Q - 1.5) & \text{for} \quad q = Q - 1 \end{cases} \tag{4}$$

The LCDG, which takes account of tails of the continuous Gaussian densities, fits a discrete empirical distribution better, than more conventional linear combinations of

the Gaussian densities (LCG) [99]. Moreover, the LCDG allows for on-line unsupervised model learning to account for non-uniform intensity variations in medical images acquired with different scanners and scanning parameters.

The estimated distributions allow for getting the marginal density for each control point during the evolution of the deformable models. For the K dominant modes of an empirical marginal distribution, which relate to the regions of interest (in our particular case, $K = 2$), the LCDG model with C_p positive and C_n negative components, such that $C_\mathrm{p} \geq K$, is defined as [98, 100]:

$$P_{\mathbf{w},\boldsymbol{\Theta}}(q) = \sum_{r=1}^{C_\mathrm{p}} w_{\mathrm{p},r}\psi(q|\theta_{\mathrm{p},r}) - \sum_{l=1}^{C_\mathrm{n}} w_{\mathrm{n},l}\psi(q|\theta_{\mathrm{n},l}) \tag{5}$$

with the restricted non-negative weights $\mathbf{w} = [w_{p,.}, w_{n,.}]$:
$\sum_{r=1}^{C_\mathrm{p}} w_{\mathrm{p},r} - \sum_{l=1}^{C_\mathrm{n}} w_{\mathrm{n},l} = 1$.

In our experiments, the marginal intensity distributions of the images have two dominant modes: one mode for the cavity and another mode for the LV wall. Figure 19 illustrates the basic steps of building the LCDG models of both the modes (more details are given in [98, 100]).

3 Tracking Control Points of Deformable Models

The proposed coupled deformable models are initialized manually by the user in the first image frame of a given slice (see Fig. 22). Each control point, $\phi(\tau)$, of the deformable model is characterized by the feature vector representing five features, namely, the grey level q, internal energy $\xi_{int}(\phi(\tau_q))$, marginal probability $P(q)$, total Gibbs energy E_G, and coupling factor $\frac{1}{d_c(\phi_i(\tau),\phi_o(\tau))}$, the latter being the inverse minimum distance between the control point on the current (inner or outer) border and the other border of the LV wall. The candidate control points of the current (say, inner) contour that are closer to the other (outer) contour will be discarded as they will result in a higher total energy. To rule out the possibility of increasing the
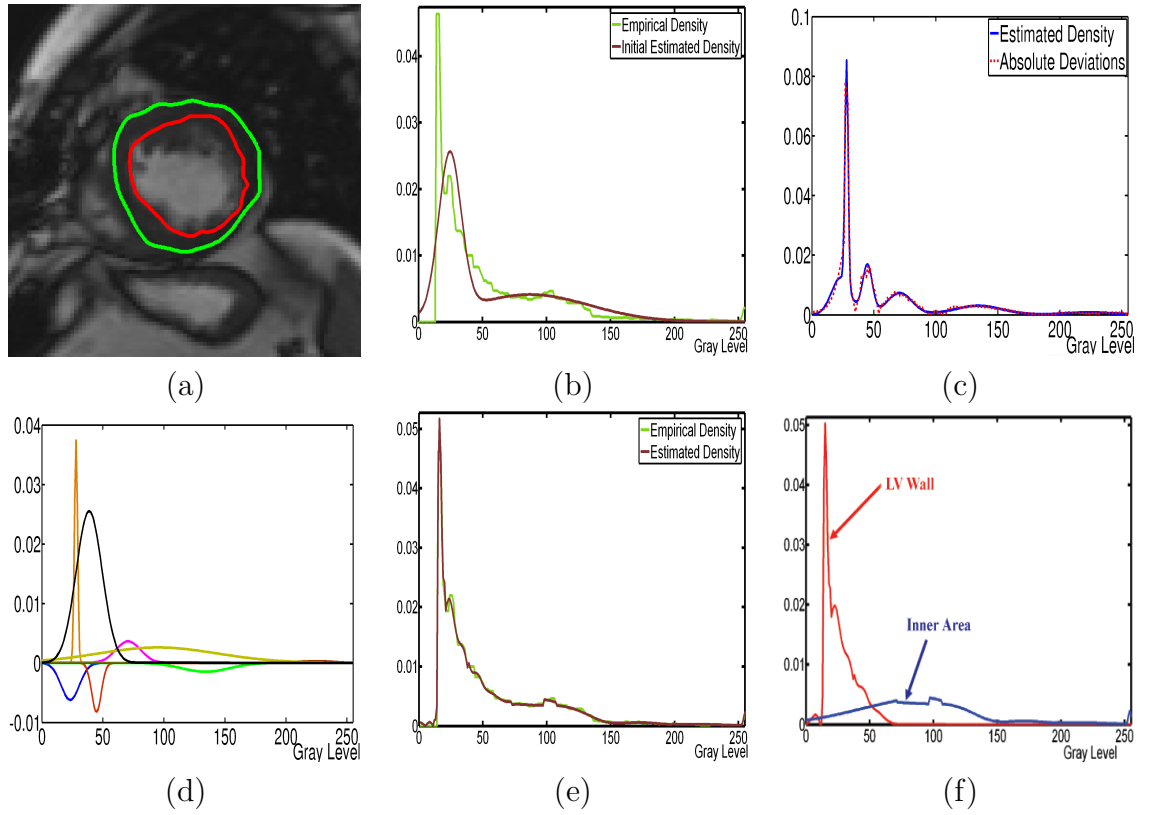
Figure 19. Step-wise LCDG modeling of the marginal intensity distribution: (a) LV wall borders found for a typical cine CMR image, (b) the estimated dominant bi-modal Gaussian mixture, (c) the subordinate Gaussian mixture estimated for the absolute deviations between the dominant mixture and empirical distribution, (d) the found sign-alternate LCDG components, (e) the final refined LCDG, and (f) the final estimated LCDGs for each dominant mode.

Algorithm 1 Main segmentation steps for each slice:

1. **Initialization:**

   - Define the initial contours by manually selecting a number of control points around the LV wall from the first image frame of the current slice (see Step #1 in Fig. 17).

2. **Estimate the first-order features of visual appearance:**

   - Collect the empirical grey level distribution for the current image frame.
   - Estimate the marginal intensities for the LV wall and background using the LCDG model.

3. **Estimate the second-order features of visual appearance** using the MGRF model defined in Eq. (3).

4. **Construct the labeled image** using the Bayesian classifier and the first- and second-order features of visual appearance.

5. **Tracking control points of the deformable models.** For each control point of the deformable contour on time frame t_n:

   - Estimate the internal energy using the first- and second-order derivatives of the contour.
   - Select from the nearest neighbors (i.e., the search space) of the current control point, on time frame t_{n+1}, those with the same label as the others (white and green points, respectively, in Fig. 17).
   - Calculate the distance between the selected and control points of the other contour.
   - Calculate the feature vectors of the candidate locations on time frame t_{n+1} and their Euclidean distances to the current control point.
   - Find the correspondence of the current control point by the minimum Euclidean distance.

6. Use the tracked points as the initial contour for the next image frame and repeat Steps 2 through 5 for all frames of the current slice.

wall size from our approach, the pixel is classified (Step 4 in Algorithm 1) before estimating the energy (Step 5 in Algorithm 1). If the pixel and the wall differ by their visual appearance(e.g., the point is outside the wall), it will be discarded at Step 4 by the Bayesian classifier. The correspondence between each control point in time frames t_n and t_{n+1} is estimated by matching all the five features. Note that all the features were normalized with respect to their maximum values and equally weighted. Basic steps of the whole process of tracking the control points of the deformable models are illustrated in Fig. 17 and detailed in Algorithm 1.

C   Evaluation Tests for the Proposed Segmentation

Performance of our segmentation is evaluated by using two types of metrics: a pixel-based similarity and a distance-based error. The pixel-based similarity indicates the overlap between the segmented area and the ground truth. It is important for studying areal measurements, e.g., the cavity area. The distance-based error indicates how close edges of the segmented region are to the ground truth. It is instrumental in studying linear measurements, e.g., wall-thickening. Both the evaluation metrics are detailed below.

1   Pixel-Based Similarity Metric

The segmentation accuracy is first evaluated using the Dice similarity coefficient (DSC), characterizing the agreement between the segmented and ground truth regions [101]:

$$\text{DSC} = \frac{2 \times \text{TP}}{2 \times \text{TP} + \text{FP} + \text{FN}} \tag{6}$$

where TP, FP, and FN denote the true positive, false positive, and false negative segmentation results, respectively (see Fig. 20). For a segmented region, $\mathbf{S}$, and its ground truth, $\mathbf{G}$, $\text{TP} = |\mathbf{S} \cap \mathbf{G}|$ is their overlap area, i.e., the number of the common points in $\mathbf{S}$ and $\mathbf{G}$; $\text{FP} = |\mathbf{S} - \mathbf{S} \cap \mathbf{G}|$ is the number of the different points between

S and TP, and FN = $|\mathbf{G} - \mathbf{S} \cap \mathbf{G}|$ is the number of different points between **G** and TP. The closer the DSC to the unit value, the better the segmentation. To obtain the ground truth in our experiments, an MRI expert delineated the LV borders.
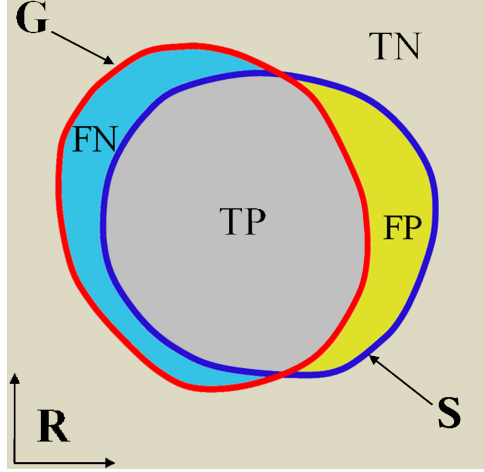
Figure 20. 2-D diagram of errors used for calculating the Dice similarity coefficient (DSC).

2 Distance-Based Error Metric

The distances between the ground truth, **G**, and segmentation, **S**, borders are used as an additional metric to measure the accuracy of our approach. Measuring the distances requires establishing accurate point-to-point correspondences between the borders of **G** and **S**. Traditionally, these correspondences are co-allocated by proceeding in the radial direction from one of the borders toward the other one. However, such a straightforward procedure is not accurate enough and leads to incorrect correspondences. Therefore, we use here a considerably more accurate search for the point-to-point correspondences, or matches between the borders based on solving the planar second-order partial differential Laplace equation [46]:

$$\nabla^2\gamma = \frac{\partial^2\gamma}{\partial^2 x^2} + \frac{\partial^2\gamma}{\partial^2 y^2} = 0 \tag{7}$$

that defines a scalar field γ, called the harmonic function. The solution $\gamma(x,y)$ of Eq. (7) between two boundaries (see Fig. 21) results in intermediate equipotential surfaces and streamlines (field lines), being everywhere orthogonal to all the equipotential surfaces. The streamlines establish natural point-to-point correspondences between the boundaries. Once the correspondences are established, the distance-based error metric is defined as the average Euclidian distance between the corresponding pairs of points. For better accuracy, all the points on the ground truth contour and their corresponding points on the segmented contour were used to calculate this metric.
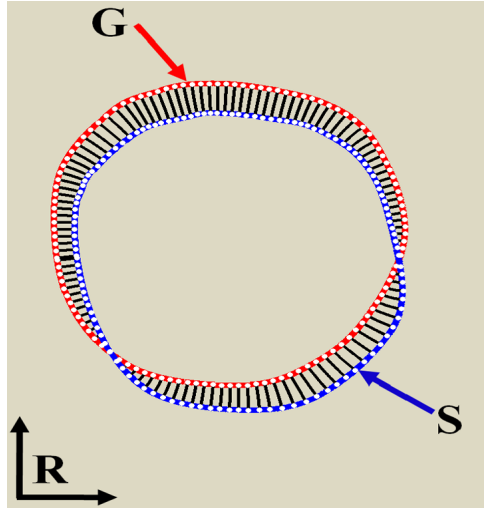
Figure 21. 2-D diagram illustrating the measurement of the distance-based error along the correspondences (black lines) between the ground truth, **G**, and automatically segmented, **S**, regions.

D Experimental Results

1 Clinical Data

The proposed approach has been tested on 15 independent cine CMR data sets from patients enrolled in a stem cell therapy project. The patients were with prior myocardial infarctions, by clinical indexes, and documented by viability MRI. We obtained about ten image sections, with typically 25 temporal image frames, for the complete coverage of the LV for each patient. Images were acquired using a 1.5T Espree system, Siemens Medical Solutions Inc., USA. Breath-hold cine acquisitions were done using segmented TrueFISP contrast, with phased array wrap-around reception coils. Typical parameters were as follows: TR – 4.16 ms; TE – 1.5 ms; flip angle – 80°, one average; 12 k-space lines per segment; typical in-plane spatial resolution – 1.4×3.1 mm^2; and slice thickness – 8 mm. The patients were part of an Institutional Review Board (IRB) approved study investigating a novel myoregeneration therapy, and all the patients had given informed consent before imaging.

2 Segmentation Results

Our segmentation was tested on the above cine CMR data sets, having been collected from six independent patients. To initialize the deformable models, six points were manually selected in the first image frame, for all experiments. Then, a spline fit to get a smooth curvature was used for producing 20 equi-spaced points in order to track them over the whole cardiac cycle. A step-wise segmentation of the LV wall boundaries for one data set at different image sections is shown in Fig. 22. Additional segmentation results for six independent data sets at different image sections are demonstrated in Fig. 23. To evaluate the accuracy of the proposed segmentation approach, we use the DSC [101] to determine the agreement between our segmentation and the ground truth borders, as described in Section 1. Table 1

47

summarizes the DSC statistics obtained for all data sets. The ground truth was obtained by manual contouring of the LV borders by an MRI expert.
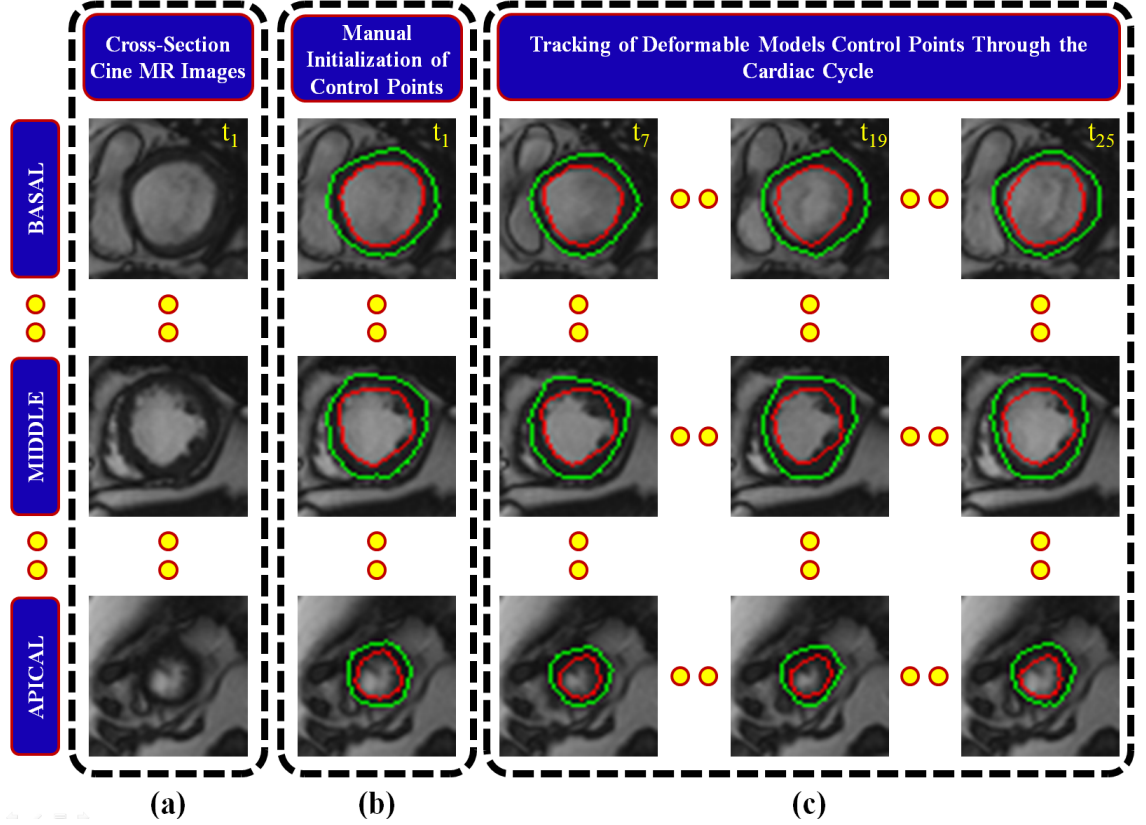
Figure 22. Steps of the proposed segmentation at different cross sections covering the LV for one data set: (a) typical cine CMR images, (b) manually initialized deformable contours, and (c) final segmentation based on tracking the control points of the initial contours at different time points over the cardiac cycle.

To highlight the advantage of the proposed segmentation, we compare its performance against the level set approach by Chan and Vese [102] (CV) and the shape-based level set approach by Abdelmunim and Farag [103] (AF). The comparative accuracy of the proposed approach versus the CV and AF on the representative data for five subjects is shown in Fig. 24. Table 1 compares our segmentation with the CV and AF methods versus the ground truth, based on the
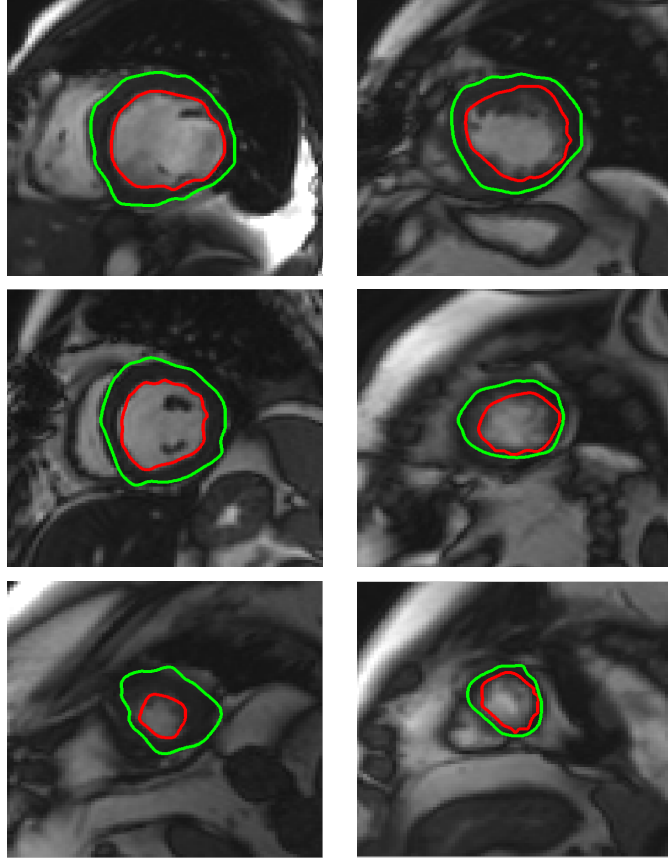
Figure 23. Reliable determination of the wall boundaries by the proposed segmentation at different image sections for six independent data sets. The inner and outer contours of the LV wall are in red and green, respectively.

TABLE 1. Comparative accuracy of our segmentation versus the methods in [102, 103] by the DSC on all the 15 data sets (AD and SD stand for average distance and standard deviation, respectively).

	DSC	
Approach	Mean ± SD	P-value
Our	0.93 ± 0.02	
CV [102]	0.89 ± 0.02	$\leq 10^{-4}$
AF [103]	0.90 ± 0.03	0.002

DSC metric for all data sets. As documented in Table 1, our approach performs notably better, according to its higher DSC value. Statistical significance of the better performance with respect to the CV and AF methods is confirmed by the paired t-tests between the DSC values for our and the compared methods. Table 1 shows that the advantage of our approach is statistically significant with respect to the CV and AF methods, evidenced by the P-values less than 0.05.

In addition to the DSC metric, the performance of our segmentation with respect to the CV [102] and AF [103] methods were evaluated using the distance-based metric described in Section 2. In order to compute the distance error, the point-to-point correspondences between the segmented borders and ground truth (obtained by an MR imaging expert) were accurately estimated by solving the Laplace equation and co-allocating the coincident points as described in Section 2. Comparative results of the paired t-test statistical analysis on the average distance (AD) values are summarized in Table 2. The performance analysis based on the DSC and AD metrics show that our method outperforms the CV and AF ones. The lower performance of the CV approach [102] could be caused by its sensitivity to image noise and inhomogeneity in the LV wall, because this method does not account for spatial pixel interactions in addition to the first-order intensity information. On the other hand, the AF approach [103] improves the segmentation accuracy by employing shape information. However, their shape prior, constructed as a linear combination of signed vector level set functions, does not cover all the variability that exists in the LV.

In order to test the sensitivity of our segmentation with respect to the ground truth contours produced by different observers, 100 images from four different data sets, at different sections of the heart, were manually segmented by using both experienced intra- and inter-observers. The DSC values for our segmentation versus the ground truth from these observers are summarized in Table 3. According to the paired t-test performed to test these trials, the P-values of 0.50 (intra-observer),
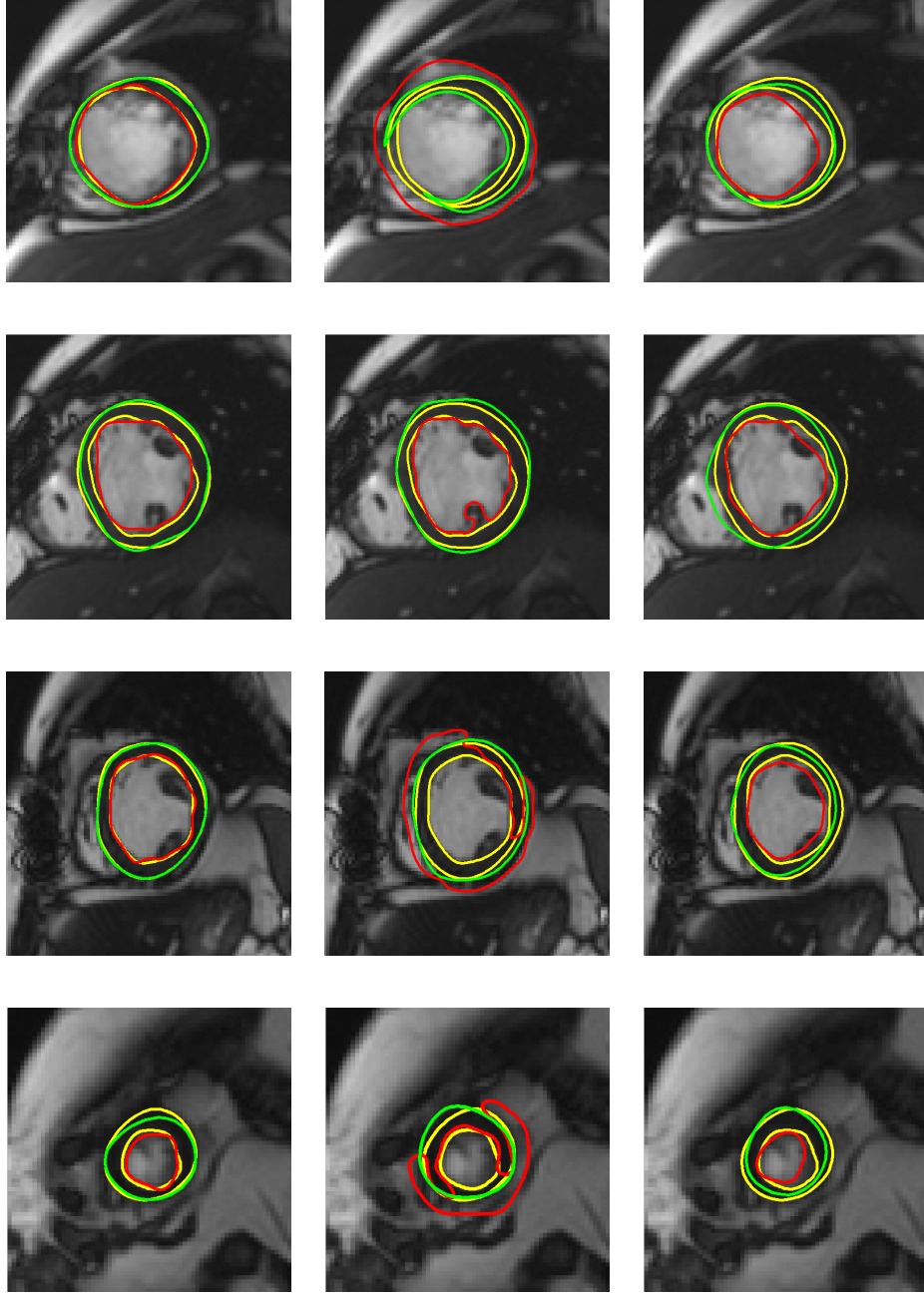
Figure 24. Comparative results for our approach (left column) and the traditional CV [102] level set (middle column) and AF [103] vector level set (right column) approaches with respect to the manual ground truth (yellow) from an expert for four independent subjects. The inner and outer contours of the model segmentation are in red and green, respectively.

TABLE 2. Comparative accuracy of the proposed segmentation versus the CV [102] and AF [103] methods in terms of the distance metric on all 15 data sets (IC, OC, AD, and SD stand for inner contour, outer contour, average distance, and standard deviation, respectively).

| | **Average distance**, *mm* | | | | | |
| | **IC** | | **OC** | | **Average** | |
Approach	AD±SD	*P*-value	AD±SD	*P*-value	AD±SD	*P*-value
Our	2.4±0.6		1.88±0.49		2.2±0.6	
CV [102]	8.8±4.9	10^{-3}	2.6±0.9	0.01	5.7±4.7	10^{-3}
AF [103]	3.4±1.3	0.013	2.29±1.17	0.22	2.9±1.4	0.013

and 0.32 and 0.75 (inter-observer) indicate that the differences are statistically insignificant, which supports their strong agreement.

Furthermore, to test the sensitivity of our approach to the choice of the control points that initialize the deformable boundaries, five different sets of the initial control points were selected around the LV wall on the data sets for one patient. The effect of these different initializations on the segmentation accuracy was evaluated using the DSC metric and summarized in Table 4. Both the DSC and *P*-values of the paired *t*-test confirm the proposed approach does not depend significantly on the initial choice of the control points.

TABLE 3. Intra- and inter-observer performance of the automated segmentation versus the ground truth using 100 images from different data sets and the DSC metric (SD and OB_i stand for standard deviation and observer *i*, respectively).

| | **DSC** | | |
| | OB_1 1st trial | OB_1 2nd trial | OB_2 |
	1	2	3
Mean	0.932	0.929	0.933
SD	0.0245	0.0245	0.0250
P-value	(1,2) : 0.50	(2,3) : 0.32	(1,3) : 0.74

Finally, that the proposed approach is not limited to the data collected by our scanning protocol was demonstrated by testing on cardiac cine MRI data provided

TABLE 4. Performance (in terms of the DSC metric) of our automated segmentation versus the ground truth on one patient data set for different choices of the initial control points of the deformable boundary (SD stands for standard deviation).

Initializing Trial	DSC	
	Mean $\pm$ SD	P-value
First	0.925 ± 0.027	
Second	0.931 ± 0.021	0.176
Third	0.924 ± 0.026	0.873
Fourth	0.925 ± 0.022	0.963
Fifth	0.926 ± 0.025	0.867

by organizers of the MICCAI 2009 Cardiac MR LV Segmentation Challenge. The data sets, scanning protocol, and evaluation criterion are fully described by Radau et al. [104]. The performance of our approach was compared first with the morphological segmentation by Lu et al. [105] and, secondly, with the related coupled-surface segmentation, such as the ASM method by O'Brien et al. [106]. The morphological segmentation was the most accurate among all the methods presented at the aforementioned MICCAI 2009 contest. Table 5 compares our approach and the morphological approach by Lu et al. [105] for three selected subjects with the highest, moderate, and lowest segmentation accuracy as reported by Lu et al. [105]. The comparisons show that our results are better in terms of the higher DSC values and lower average distances. In addition, O'Brien et al. [106] reported the lower mean Dice values of 0.81 and 0.91 and higher mean AD values of 3.73 mm and 3.16 mm for the coupled-surface based segmentation of the endocardium and epicardium, respectively. This highlights the advantages of our approach.

In addition, Table 6 shows the average execution time for each segmentation approach. Being implemented on an Intel quad-core processor (3.2 GHz each; 16 GB memory) and a 1.5 TB hard drive with RAID technology using Matlab, our approach takes 51.9$\pm$1.3 seconds for segmenting the wall border on a given time series (25 temporal images) of a CMR dataset. It is clear that our approach is

TABLE 5. Comparative segmentation accuracy (mean±SD) of the proposed segmentation versus the morphological method [105] on the selected three MICCAI 2009 Challenge data sets (IC, OC, DSC, and AD stand for inner contour, outer contour, Dice similarity coefficient, and average distance, respectively).

	DSC		AD (mm)	
Algorithm	IC	OC	IC	OC
Proposed Approach	**0.91±0.03**	**0.94±0.01**	**1.81±0.39**	**1.52±0.27**
Morphology-based approach	0.88±0.05	0.94±0.04	2.03±0.58	1.96±1.15

slightly faster than the AF approach [103] and significantly faster than the CV approach [102]. In part this is because our deformable models are initialized closer to the object borders and thus need no extra time to reach the actual contour, in contrast to the level-set methods, which are intrinsically iterative and take longer time to reach the borders.

TABLE 6. Comparative processing times of the proposed segmentation versus the Cv [102] and AF [103] methods for the wall border segmentation on a given time series (25 temporal images) of a CMR dataset (SD stands for standard deviation).

	Processing time
Approach	Mean ± SD
Our Approach	51.9 ± 1.3
CV Approach [102]	418.0 ± 110.4
SB Approach [103]	72.0 ± 6.7

3   Clinical Applications

The proposed segmentation is directly applicable to estimation of quantitative global indexes, such as wall mass, end-systolic volume (ESV), end-diastolic volume (EDV), and ejection fraction (EF), as well as local indexes, such as wall thickening and functional strain. These functional indexes help cardiologists to accurately quantify the heart status. This chapter uses the EF as a

clinically relevant and well-documented global indicator of the LV function in terms of the total cavity volume (the LV volume variation over time):

$$EF = \frac{EDV - ESV}{EDV} = 1 - \frac{ESV}{EDV} \qquad (8)$$

where ESV and EDV are the end systolic (the smallest cavity area) and the end diastolic (the greatest cavity area) volumes, respectively.

To estimate the EF, we use the LV cavity volume-time data at each image slice. Following the delineation of the cavity contour at each time point (image frame) of the cardiac cycle, the corresponding cavity areas are computed and a curve representing the physiology over the cardiac cycle is constructed. Then, the Simpson's rule is used to estimate the total LV volume by summing the contributions of enclosed areas from the individual image slices. From the total ventricular function curve, we can automatically extract the EDV and ESV (see Fig. 25) and hence calculate the EF.

The clinical benefit and applications of the proposed approach are highlighted by testing the ability of our framework to facilitate the follow-up treatment, using the EF metric. A typical example of the EF values estimated with our approach for the pre-and post-treatment of one patient enrolled in the stem cell therapy project is shown in Fig. 26. Table 7 summarizes the EF values for the pre- and post-treatment of five patients. These results show the improvement after therapy, which was also documented using other clinical indexes (e.g., by total reduction in infarct area using MRI viability [107]).

The accuracy of estimating the global functional indexes is validated by measuring the degree of agreement between the global functional parameters (EDV, ESV, and EF) obtained by our approach and the ground truth. The Bland-Altman analysis [108], calculating the bias (mean difference) and the 95% limits of agreement, i.e. $\pm$ 1.96 SD (standard deviation), around the bias, shows good agreement between our measurements and the ground truth as demonstrated in
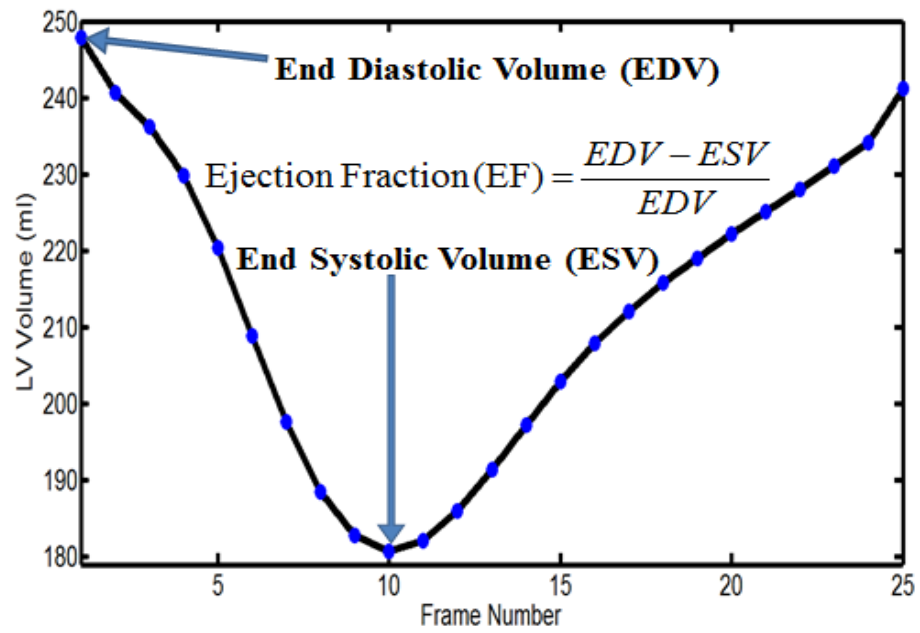
Figure 25. Ventricular function curve (obtained by summing the cavity areas over the heart) over the cardiac cycle, being used to estimate the EF.

TABLE 7. EF results, being used to follow up after the one year treatment for five patients enrolled in the stem cell therapy study. Larger EF values indicate an enhancement in the myocardial wall function.

	Ejection Fraction (EF%)	
	Pre	**Post**
Subject 1	31	46
Subject 2	20	28
Subject 3	35	44
Subject 4	20	25
Subject 5	25	28
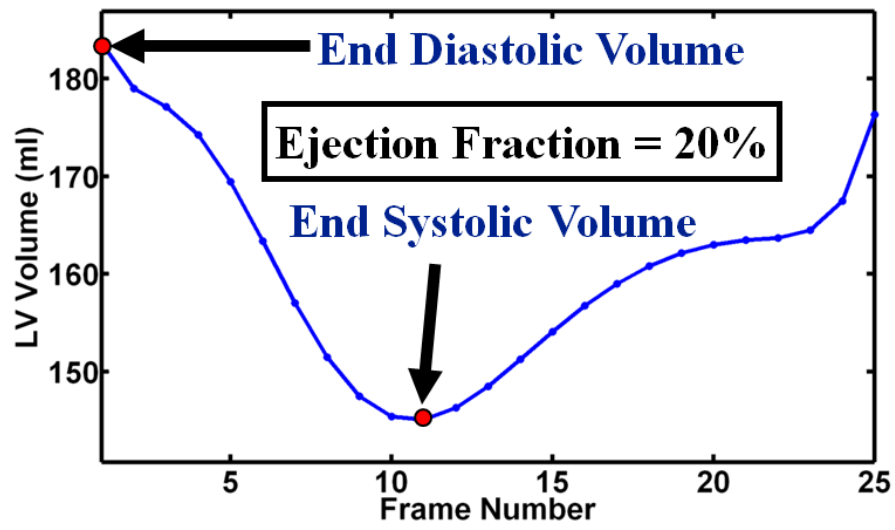
(a)
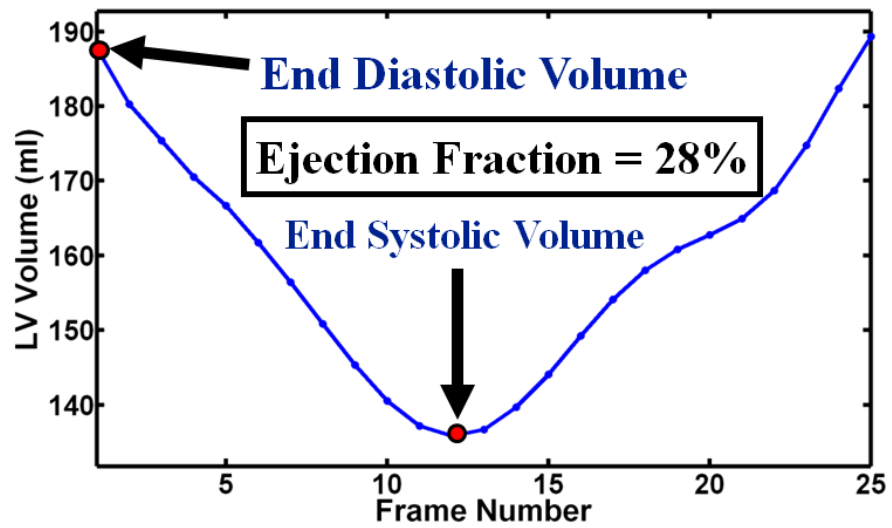
(b)

Figure 26. Ventricular function curves (a) before and (b) after one year treatment for one patient enrolled in the stem cell therapy study.

Fig. 27. The results show 10 ml maximum errors of estimating EDV and ESV values (less than 5% of the heart volume) and less than 4% error in the estimation of EF values, which is clinically acceptable.

Finally, since the proposed approach can accurately track the LV wall border points, our future work will be dedicated to ultimately estimating the wall thickening contractile function and using the cine CMR images to estimate the strain. Traditionally, the functional strain is estimated by using the tagged images that lead to errors between the estimated indexes due to the inter-slice variability between the different image modalities. We expect that our approach can precisely estimate more correlated global and local functional indexes to completely characterize the heart status.

E   Summary

In total, a 3D (2D + time) novel, fast, robust, bi-directional coupled parametric deformable models that are capable of segmenting LV wall borders is presented. These models use first- and second-order visual appearance features. First-order visual appearance of the cine CMR signals (inside and outside the bound- ary of the deformable model) is modeled with an adaptive linear combination of discrete Gaussians (LCDG). Second-order visual appearance of the LV wall is accurately modeled with a translational and rotation-invariant second order Markov-Gibbs random field (MGRF). The LCDG parameters are estimated using a modified EM algorithm, and the potentials of rotationally invariant MGRF are computed analytically. First, the initial contours are defined by manually selecting a number of control points around the LV wall from the first image frame of the current slice. Second, first- and second-order visual appearance features are estimated using the LCDG and the MGRF respectively and a labeled image is constructed using the Bayesian classifier and the first– and second–order features of visual appearance. Control points of the deformable modelsare then being tracked
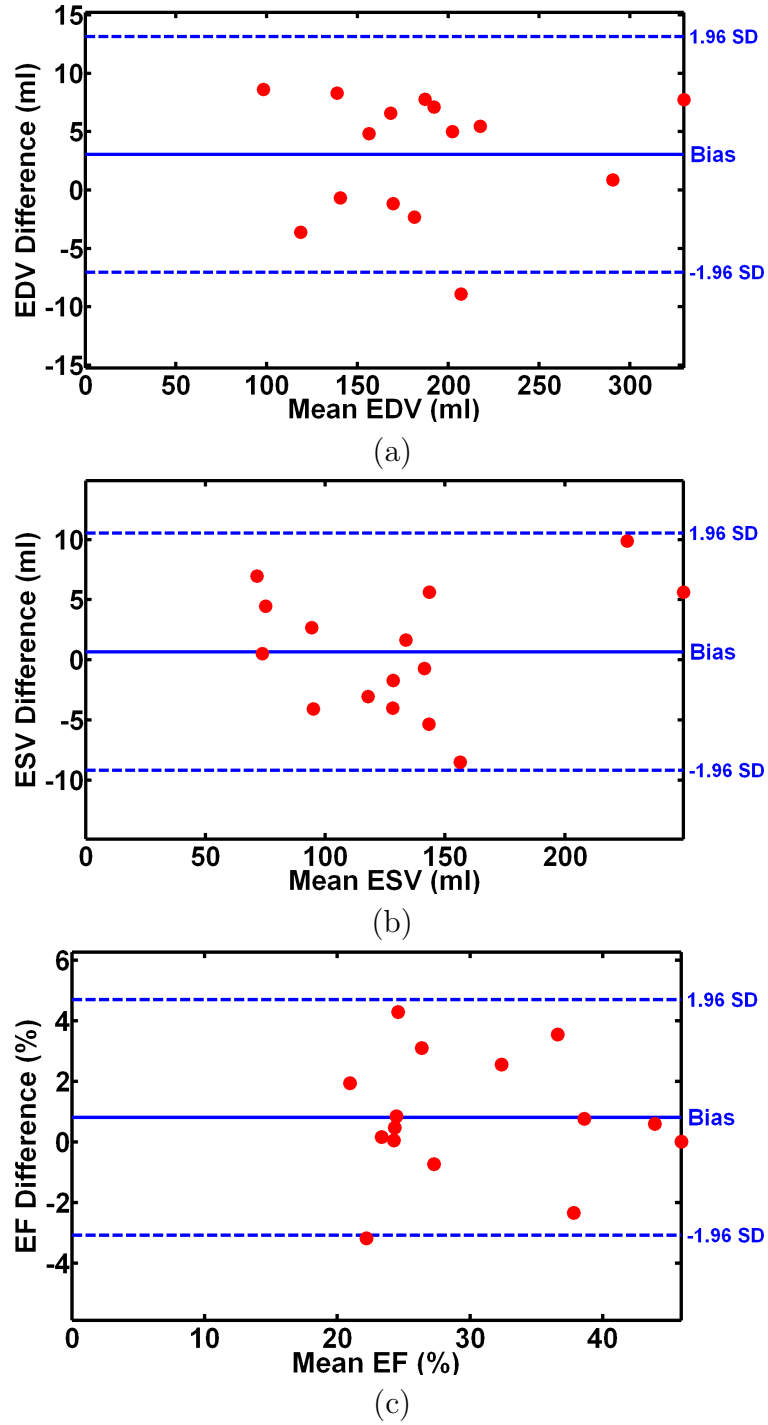
Figure 27. Bland-Altman plots for the global function parameters: (a) EDV, (b) ESV, and (c) EF, showing the difference between our segmentation and the ground truth (y-axis) versus their average (x-axis). For a good agreement, the data points should fall within the 95% limits of agreement, i.e., ± 1.96 SD around the bias.

till the last time fram. The results suggest that the proposed approach can precisely segment C-CMR images. In addition, the results confirm the robustness of the proposed methods against the shape variations of the LV and the anatomical structures that have noise and inhomogeneity problems. The work presented in this chapter has been published in Medical Physics [109], the IEEE International Conference on Image Processing (ICIP13) [110] and the International Symposium on Computational Models for Life Science (CMLS13) [111].

CHAPTER IV

MYOCARDIUM FUNCTION ASSESSMENT USING CINE MR IMAGES

A   Introduction

Quantification of cardiac performance is crucial for the diagnosis and management of patients with cardiac diseases. A number of important indicators have been employed for quantifying the cardiac performance, e.g., wall thickness, wall thickening, and functional strain [112]. Currently, a number of different medical image modalities have been used for estimating these indicators. For example, tagged MRI or ultrasound are the traditional medical image modalities for estimating the functional strain, whereas cine CMR is the traditional technique for estimating wall thickening. in this dissertation, we aim to develop a framework for estimating different performance indexes of the heart (e.g., functional strain and wall thickening) from the same image modality (i.e., cine CMR) in a way that avoids the inconsistency between different estimated indexes. This inconsistency results from the inter-slice variability and different image resolutions of the different image modalities. Next, we will overview the current methods for estimating the wall thickening and the functional strain as well as their limitations.

B   Wall Thickness Analysis

Wall thickening is an important indicator for myocardium dysfunction, which is more accurate than wall motion analysis [113–116]. It is typically assessed by visual inspection, which is preferred clinically for practical purposes [117].However,

this is obviously a time consuming process and is prone to considerable intra- and inter-observer variability which is a drawback [113, 118–120]. To overcome this, local myocardial wall thickness is derived, automatically or semiautomatically, after tracing the endocardial and epicardial boundaries in all short-axis images. Prasad et al. [121] proposed to measure the myocardial thickening in CMR more reliably by solving a partial differential Laplace equation. However, to reduce the effects of segmentation errors in the wall thickness estimation, a further step of manual adjustment was performed by a clinical expert. Recently, Khalifa et al. [67] proposed an automated framework for analyzing the wall thickness and thickening function by solving the 2D Laplace equation, However, their method is based on 2D analysis and did not take into account the 3D motion of the cardiac wall (i.e., out-of-plane motion). Therefore, there is a need for developing more methods for more accurate wall thickness analysis.

C   Functional Strain Analysis

Functional strain is another important indicator of the cardiac condition that can be used for detection of local cardiac diseases (such as coronary atherosclerosis) and global conditions (such as heart failure and diabetes) [55, 122]. In the literature, functional strain is estimated based on nonrigid registration using ultrasound images [123, 124] or motion analysis using tagged MRI [125–129]. Unfortunately, ultrasound images are low contrast. Also, the registration is computationally expensive and involve voxel/pixel errors. On the other hand, methods that are based on tagged MRI analysis are more common. However, these methods failed in cases of a high-rate motion between successive frames, a through plane motion, or boundary points [130]. Recent trends estimate the strain from cine CMR (e.g., [131–134]). Most of these methods depend on the texture features to track predefined points on the epicardium and endocardium contours of the LV wall. Thus, they are not sufficient to accurately track the LV points due to the lack of

texture information inside the wall. Therefore, there is a need for developing new methods for more accurate function strain estimation.
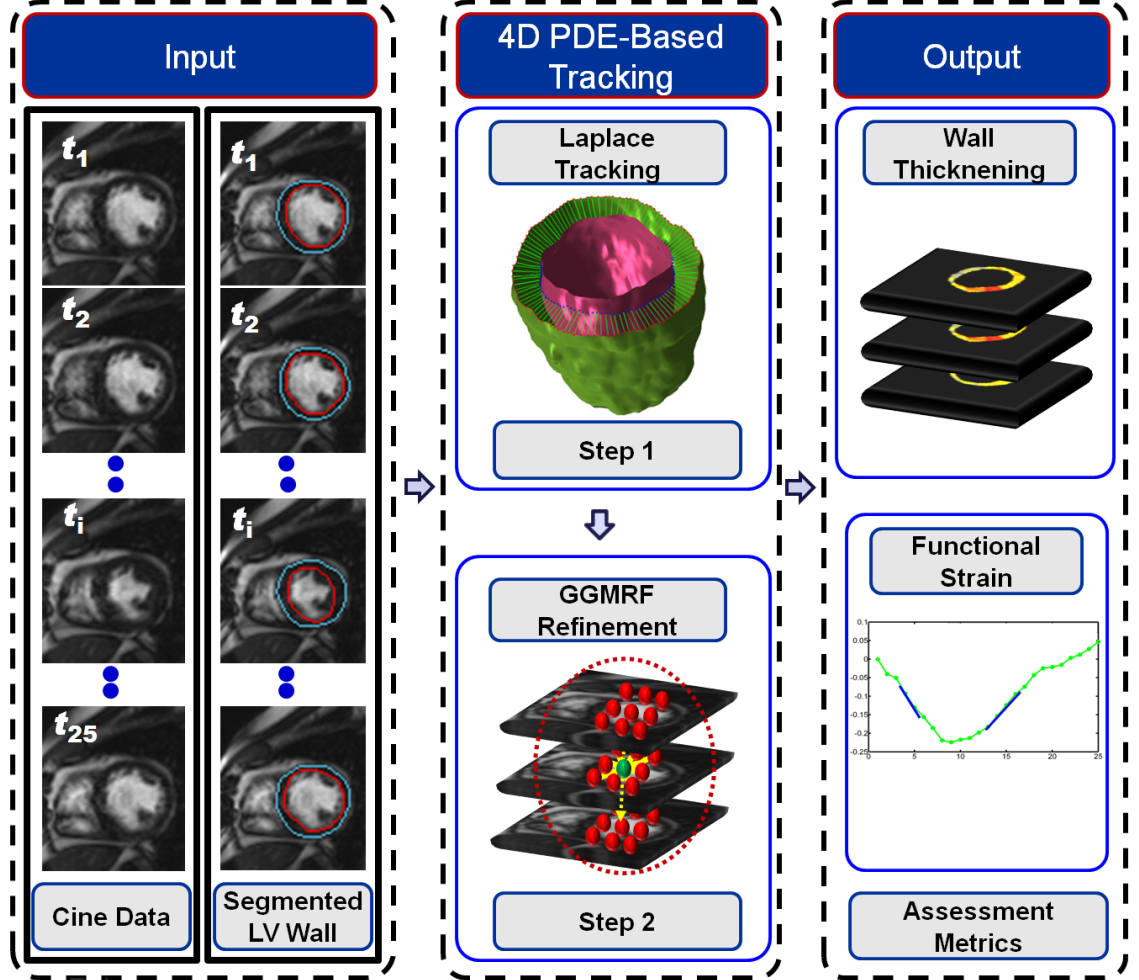
Figure 28. The proposed framework for estimating the performance indexes of the heart using cine CMR.

D   Limitations of Existing Works

In summary, the above-mentioned frameworks for analyzing the regional function (i.e., wall thickening and functional strain) are not sufficiently accurate and
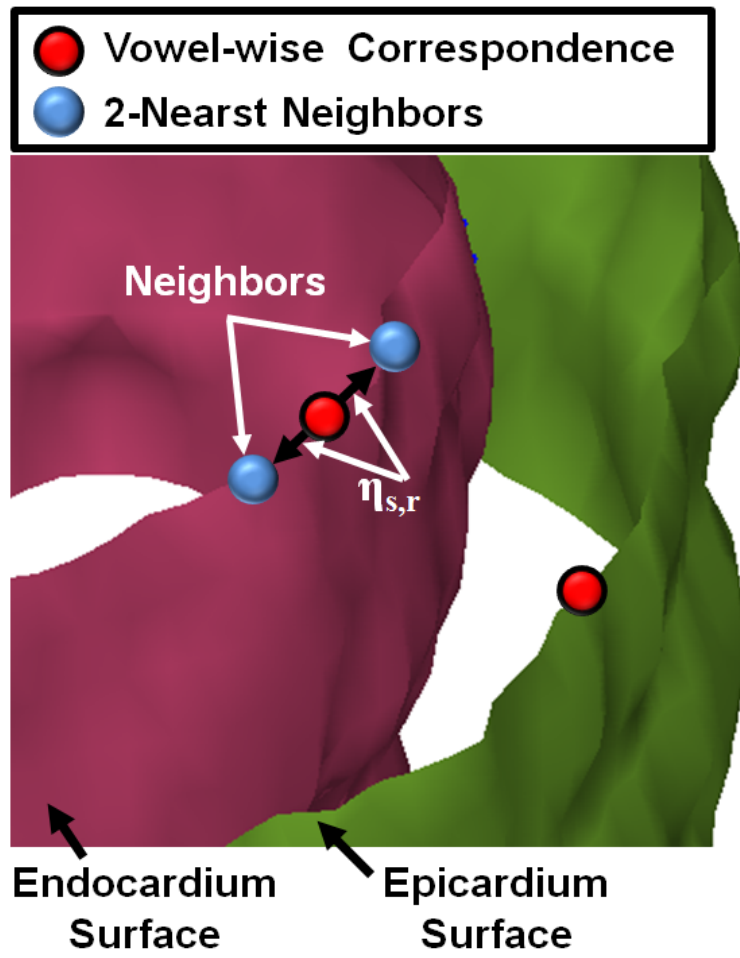
Figure 29. Schematic illustration of the 2-nearest voxels.

reliable for several reasons: (*i*) current tagged MRI strain estimation methods fail in cases of a high-rate motion between successive frames, a through plane motion, or boundary points [130], (*ii*) current tracking-based strain estimation methods are based on image features, such as the pixels' intensity and their spatial features, so they are not sufficient to accurately track the LV points due to the lack of texture information inside the wall, (*iii*) the derived indexes from cine (e.g., wall thickening) and tagged (e.g., functional strain) CMR suffer from inter-slice variability since they are driven from different cross-sections and different modalities with different resolutions, and (*iv*) current 2D methods for wall thickening estimation lead to inaccurate measurements because they do not take into account the 3D motion of the heart (i.e., out-of-plane motion).

To overcome the aforementioned limitations, we propose a novel PDE-based method to estimate the strain and wall thickening from 4D cine CMR based on tracking the LV wall geometry. To achieve this goal, we develop a 4D (3D+time) approach to track the LV wall points based on solving the 3D Laplace equation between each two successive surfaces over the cardiac cycle. To preserve the anatomy of the heart wall, the initially tracked surface points are iteratively refined through an energy minimization cost function using a generalized Gauss-Markov random field (GGMRF) image model. Since we use the same image modality (i.e., cine CMR) to estimate both wall thickening and functional strains, more correlated and accurate indexes can be obtained, which have the ability to quantify meaningful effects in treatment and physiological studies.

E   Methods

The proposed framework for estimating different performance indexes of the heart (e.g., functional strain and wall thickening) from cine CMR is schematized in Fig. 28. The segmentation of the LV wall borders can be obtained using any segmentation technique, e.g., using the method in [67]. In this chapter, we focus on

the tracking of the LV wall points and the assessment of the myocardial function. Details of the proposed framework are described below.

1   4D Tracking of the LV Wall Points

Initial tracking using the solution of the 3D Laplace equation

In order to estimate the heart performance indexes, the surface points of the myocardium should be tracked over the cardiac cycle. In this work, we propose a geometrically motivated approach to track the surface points on the LV wall through the cardiac cycle. Our method tracks the LV surfaces' points by solving the Laplace equation between each two successive surfaces (we denote one as the reference surface and the other one as the target surface). The Laplace equation is a second-order linear PDE, which takes the form:

$$\nabla^2\Psi = \frac{\partial^2\Psi}{\partial x^2} + \frac{\partial^2\Psi}{\partial y^2} + \frac{\partial^2\Psi}{\partial z^2} = 0 \tag{9}$$

where $\Psi(x, y, z)$ is the estimated electric field between the surfaces. The solution Ψ between two surfaces results in intermediate equipotential surfaces and streamlines (field lines), being everywhere orthogonal to all equipotential surfaces and establishing natural voxel-to-voxel correspondences between the surfaces. In order to estimate $\Psi(x, y, z)$, we used a second order central differences method and the iterative Jacobi approach:

$$\Psi^{i+1}(x, y, z) = \frac{1}{6}\left\{\Psi^i(x + \theta_x, y, z) + \Psi^i(x - \theta_x, y, z)\right.$$
$$+ \Psi^i(x, y + \theta_y, z) + \Psi^i(x, y - \theta_y, z)$$
$$\left. + \Psi^i(x, y, z + \theta_z) + \Psi^i(x, y, z - \theta_z)\right\} \tag{10}$$

where $\Psi^i(x, y, z)$ is the estimated electric field at (x, y, z) during the ith iteration; and θ_x, θ_y, and θ_z are the step length or resolution in x, y and z

directions, respectively. Basic steps of the proposed Laplace-based tracking methodology are summarized in Algorithm 2.

Algorithm 2 Solution of the 3D Laplace Equation Between Two Surfaces
---
1 Find the 3D edges of both LV wall surfaces.
2 **Initial condition:** Set the maximum and minimum potential Ψ at the target and reference surfaces, respectively.
3 Estimate Ψ between both surfaces using Eq. (10).
4 Iterate Step 3 until convergence is achieved (i.e., there is no change in estimated Ψ values between iterations).

GGMRF-based refinement

In order to avoid any anatomical distortions that result from solving the Laplace equation, we employ a smoothness constraint to preserve the LV wall anatomy. The introduced constraint preserves the relative position between the neighboring voxels on the target LV wall surface through iterative energy minimization using a GGMRF image model [135] on the initially tracked points. Each tracked point on the target is iteratively refined by a GGMRF image model [135] using the voxels neighborhood system (N-nearest neighbors, Fig. 29).

Given the N-nearest neighbors of each point on the target surface, the location of each point is refined using its maximum A posteriori (MAP) estimates [135] and voxel-wise stochastic relaxation (iterative conditional mode (ICM)) that jointly optimize x, y, and z spatial coordinates using [136]:

$$
\widehat{\mathbf{p}_\mathbf{s}} = \arg \min_{\widetilde{\mathbf{p}_\mathbf{s}}=(\widetilde{x_s},\widetilde{y_s},\widetilde{z_s})} \left\{ |\mathbf{x_s} - \widetilde{\mathbf{x}_\mathbf{s}}|^\alpha + \rho^\alpha \lambda^\beta \sum_{r \in N} \eta_{s,r} \left| \widetilde{\mathbf{x}_\mathbf{s}} - \mathbf{x_r} \right|^\beta \right.
$$
$$
+ |\mathbf{y_s} - \widetilde{\mathbf{y}_\mathbf{s}}|^\alpha + \rho^\alpha \lambda^\beta \sum_{r \in N} \eta_{s,r} \left| \widetilde{\mathbf{y}_\mathbf{s}} - \mathbf{y_r} \right|^\beta + |\mathbf{z_s} - \widetilde{\mathbf{z}_\mathbf{s}}|^\alpha
$$
$$
\left. + \rho^\alpha \lambda^\beta \sum_{r \in N} \eta_{s,r} \left| \widetilde{\mathbf{z}_\mathbf{s}} - \mathbf{z_r} \right|^\beta \right\} \quad (11)
$$

where $\mathbf{p_s} = (\mathbf{x_s}, \mathbf{y_s}, \mathbf{z_s})$ and $\widetilde{\mathbf{p}_\mathbf{s}} = (\widetilde{x_s}, \widetilde{y_s}, \widetilde{z_s})$ denote the tracked points' original locations and their expected estimates; N is the number of nearest neighbors (Fig. 29); $\eta_{s,r}$ is the GGMRF potential, and ρ and λ are scaling factors. In addition to N, the parameter $\beta \in [1.01, 2.0]$ controls the refinement level (e.g., $\beta = 2$ for smooth vs. $\beta = 1.01$ for relatively abrupt edges). The parameter $\alpha \in \{1, 2\}$ determines the Gaussian, $\alpha = 2$, or Laplace, $\alpha = 1$, prior distribution of the estimator. Our experiments below were conducted with $\rho = 1$, $\lambda = 5$, $\beta = 1.01$, $\alpha = 2$, and $\eta_{s,r} = \sqrt{2}$ for all directions.

2   Assessment Metrics

Strain Estimation

The estimation of strain is based on the Lagrangian strain calculation. For a 3D element with spatial dimensions x, y, and z (see Fig. 30), the strain is defined as [137]:

$$\varepsilon = \begin{bmatrix} \varepsilon_{xx} & \varepsilon_{xy} & \varepsilon_{xz} \\ \varepsilon_{yx} & \varepsilon_{yy} & \varepsilon_{yz} \\ \varepsilon_{zx} & \varepsilon_{zy} & \varepsilon_{zz} \end{bmatrix} = \begin{bmatrix} \frac{\Delta x}{x} & \frac{\Delta x}{y} & \frac{\Delta x}{z} \\ \frac{\Delta y}{x} & \frac{\Delta y}{y} & \frac{\Delta y}{z} \\ \frac{\Delta z}{x} & \frac{\Delta z}{y} & \frac{\Delta z}{z} \end{bmatrix} \tag{12}$$

where ε_{xx}, ε_{yy}, ε_{zz} denote the normal strain components in the cartesian coordinates x, y, and z respectively; ε_{xy}, ε_{yz}, ε_{xz}, ε_{zx}, ε_{yz}, and ε_{zy} denote the shear strain components in 3D; and Δx, Δy, and Δz denote the change in the 3D element dimensions between the current frame and the inital (reference) frame. As shown in Fig. 30, each strain component is estimated as the change on the length between the two frames with respect to the initial length at the reference frame. In this dissertation, we focus on estimating the normal components for the endocardium circumferential strain. To estimate these components, we use Algorithm 3.

Wall Thickness Analysis

The estimation of the wall thickening, i.e., the changes in the wall thickness during systole of the cardiac cycle, is obtained by accurate co-allocation of the corresponding points, or matches, between the inner and outer surfaces of the LV wall by solving the 3D Laplace equation. We use the geodesic distances between corresponding points to estimate the wall thickness and thickening. A typical example of finding the point-wise correspondences between the inner and outer surfaces of the heart wall using the solution of the 3D Laplace equation is shown in Fig. 31.
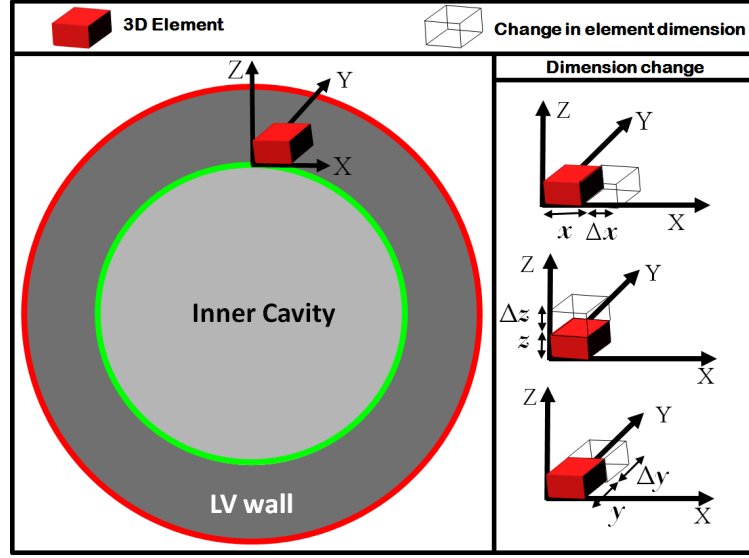
Figure 30. Schematic illustration for the estimation of the strain components on a 3D element (red). Left: 3D element at the reference frame and Right: changes in the element dimensions in the current frame.

Algorithm 3 Strain Estimation Algorithm

---

1 Segment the LV wall from cine CMR (e.g., by the approach in [67]).

2 For each two successive volumes, solve the Laplace equation between their respective inner borders to track the surface points throughout the cardiac cycle.

3 Iteratively refine the initially tracked points through energy minimization using the 3D GGMRF image model (Eq. 11).

4 Estimate the circumferential strains by tracking the change in distance between tracked points on the endocardium border using Eq. 12, see Fig. 30.
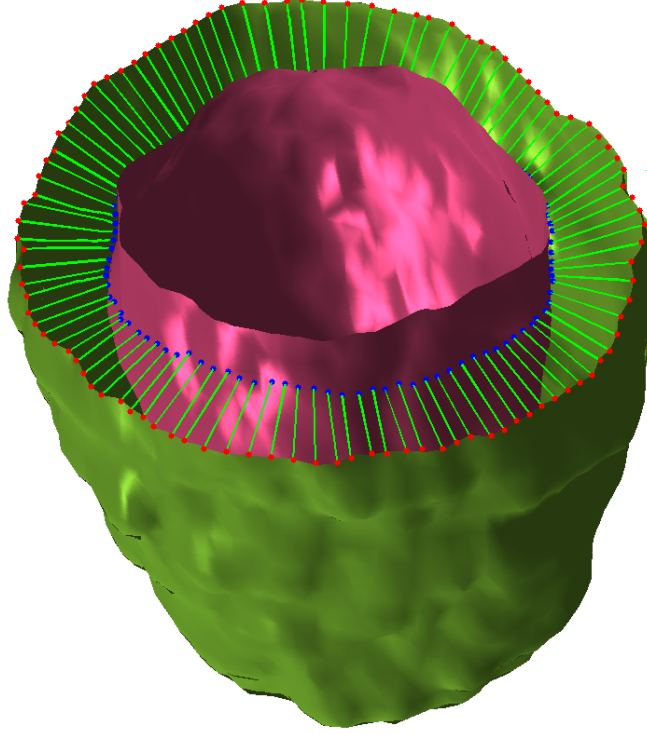
Figure 31. Coallocation of corresponding LV wall points for a patient data using the proposed method. The inner and outer LV wall surfaces are shown in pink and green respectively.

F   EXPERIMENTAL RESULTS

The proposed framework has been tested on 15 independent cine CMR data sets collected from six infarction patients who undergo a stem-cell myoregeneration therapy. Short-axis images were obtained using a 1.5 T Espree system, Siemens Medical Solutions, USA Inc., with phased array wrap-around reception coils. Breath-hold cine imaging was done using segmented True-FISP contrast. Typical parameters were: TR: 4.16 ms; TE: 1.5 ms; flip angle: 80°, 1 average; k-space lines per segment: 12; isotropic in plane resolution: $1 \times 1\ mm^2$; and slice thickness: 1 mm. Typically, 25 temporal image frames were obtained for each slice.

1 In vivo Validation

In order to validate our method, we compare the estimated values of the wall thickening and strain curves to the ground truth (GT) values, which were estimated using a set of landmark points that were traced by a radiologist through out the cardiac cycle. Comparison results between our method and the GT for estimating wall thickening and functional strain are presented in Table 8. As demonstrated, our estimation is close to the GT as documented by the statistical paired t-test with P values greater than 0.05, which indicate non-significant difference.

To highlight the advantage of the proposed 3D method for estimating the wall thickening, we compare our method with the 2D method proposed by Khalifa et al. [67]. Unlike our method, the 2D analysis [67] shows a significant difference from the GT (the paired t-test P-value is less than 0.05, see Table 8). This is due to the fact that 2D methods do not take into account the 3D heart motion (e.g., out-of-plane motion). So our method can provide more accurate results. These results highlight the advantages of the proposed framework.

TABLE 8. Comparison results for mean thickening and mean endocardium strain over the cardiac cycle using our method versus the ground truth, estimated using 12 selected landmarks. Our thickening analysis is compared to the 2D thickening analysis proposed in [67].

	Metric 1: Wall Thickening		
	Mean	**Standard Deviation**	
GT	5.74 mm	2.24 mm	P-**value**
Our	5.66 mm	1.94 mm	0.9439
2D [67]	1.42 mm	0.98 mm	0.0005
	Metric 2: Functional Stain		
	Mean	**Standard Deviation**	
GT	0.11	0.15	P-**value**
Our	0.086	0.17	0.2312

2 Clinical Applications

To emphasize the potential of using the wall thickening and strain to document changes with treatment, we have tested our method in research participants with chronic ischemic heart disease and heart damage who underwent a stem-cell myogeneration therapy. Figure 32 exemplified the circumferential strain results for one participant. As shown in the figure, the proposed method was able to detect the enhancement in strain after treatment, manifested with higher strain slopes. For visual assessment of the wall thickening (δ) functional parameter, we use a voxel-wise parametric (color-coded) map. To derive these functional maps, each δ value is normalized by relating it to the maximum value measured in the whole volume for the pre- or post-treatments, for the given subject. Fig. 33 presents the parametric maps for the δ values over multiple cross-sections for pre- and post-therapy of one subject. As shown in the figure, our 4D method can better detect the variability of the wall thickening than the 2D method proposed by Khalifa et al. [67]. These results introduce the potential of using the wall thickening and strain to document changes with treatment that were consistent with improvements in patient condition, as documented by clinical indexes. To emphasize the potential of using the wall thickening and strain to document changes with treatment, we have tested our method in research participants with chronic ischemic heart disease and heart damage who underwent a stem-cell myogeneration therapy treatment. In this section we present more results for the in vivo participants.

Figure 34 and Fig. 35 exemplified the circumferential strain results and the parametric wall thickening maps over multiple cross-sections for pre- and post-therapy of two more participants enrolled in this study. As shown in the figures, the proposed method was able to detect the enhancements in strain and wall thickening after treatment that were consistent with improvements in patient condition documented by clinical indexes. This was manifested with higher strain slopes and larger-values of wall thickening color maps. This lends encouragement for
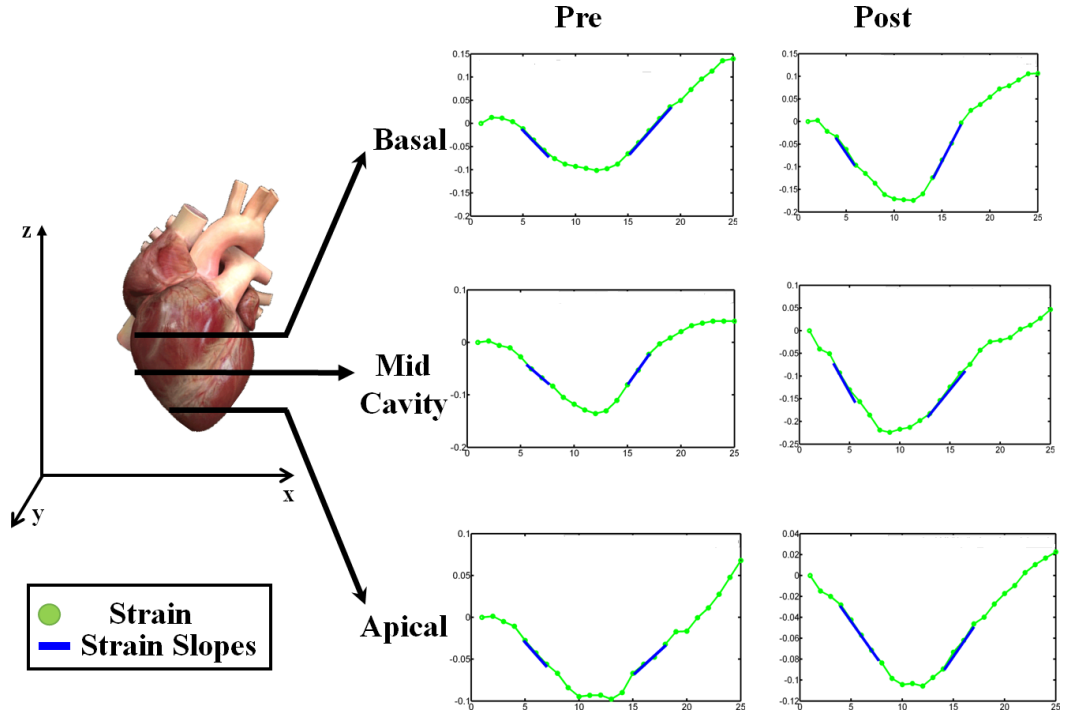
Figure 32. Pre- and post-strain analysis for a patient enrolled in this study, projected on 2D basal, mid-cavity, and apical cross-sections for illustration.

the proposed framework to detect and quantify meaningful effects in treatment and physiological studies. In addition, it is worth mentioning that all of the derived metrics are estimated from cine CMR. This avoids the need for additional tagged images and thus overcomes the inter-slice variability problem between different image modalities.

3 Comparison Results With HARP Method for Strain Estimation

Since the strain can be estimated using different methods, we used the commercial HARP diagnosoft package, version 2.6 (http://www.diagnosoft.com/) to estimate the strain on tagged data for the same six subjects enrolled in this study and compare it with our results. Tagged images were acquired by breath hold 1-1 SPAMM imaging in the cardiac short axis plane at basal, mid, and apical levels
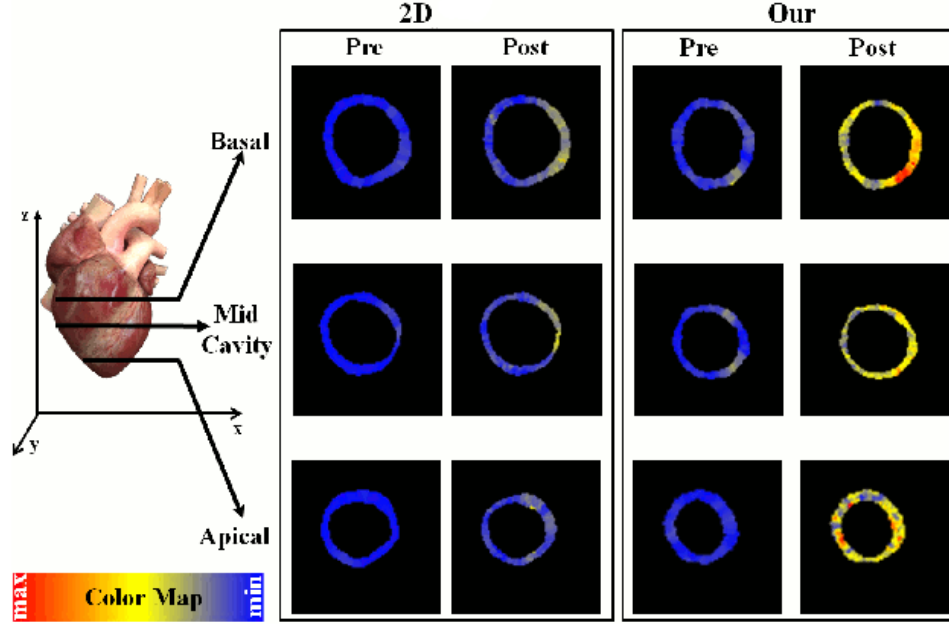
Figure 33. Pre- and post-thickening analysis using the 2D method proposed in [67] and our proposed method for a patient enrolled in this study. The results are projected on 2D basal, mid-cavity, and apical cross-sections for illustration.
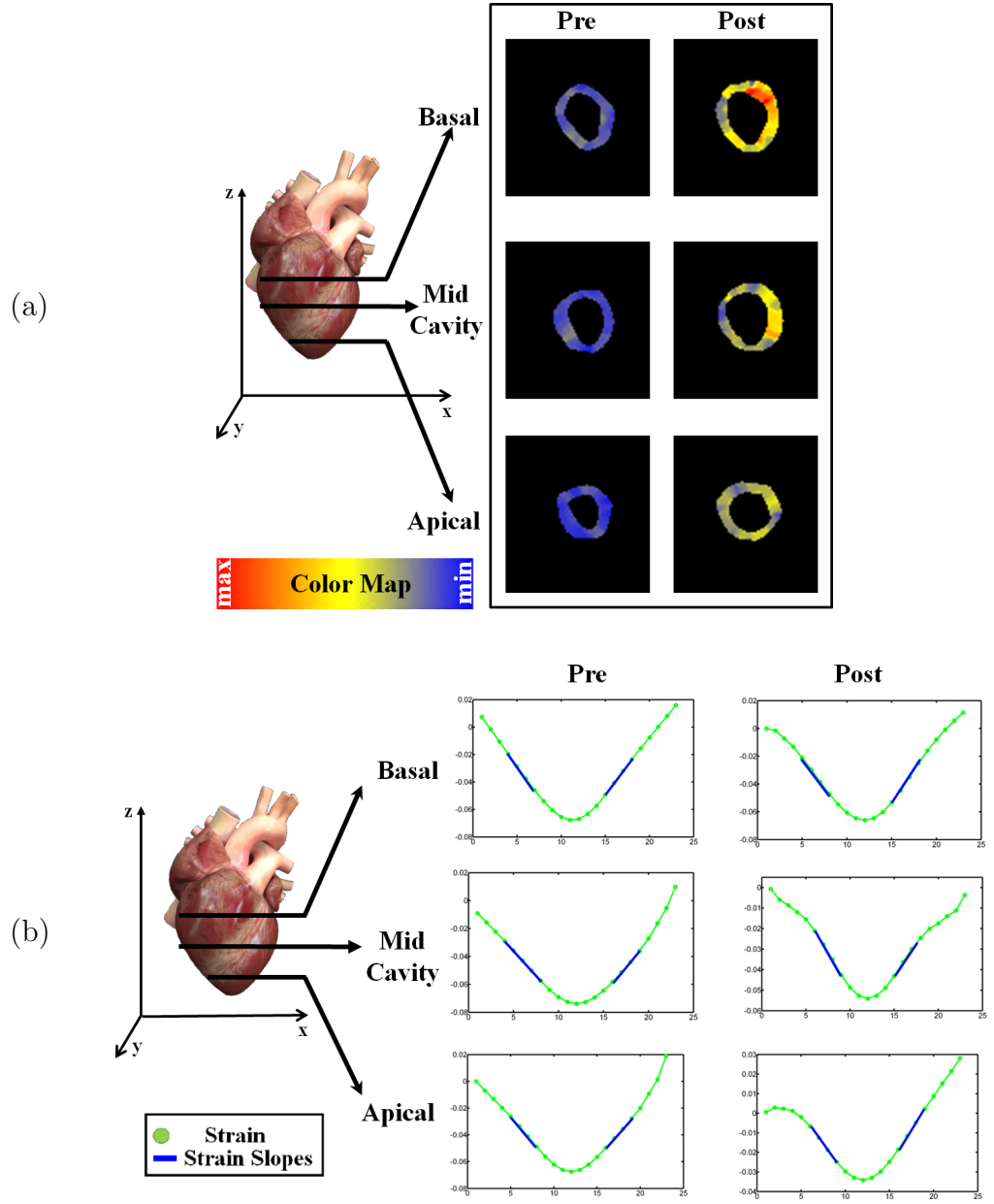
Figure 34. Pre and post (a) thickening and (b) strain results using our proposed method for a sample patient, illustrated on 2D basal, mid-cavity, and apical cross-sections.
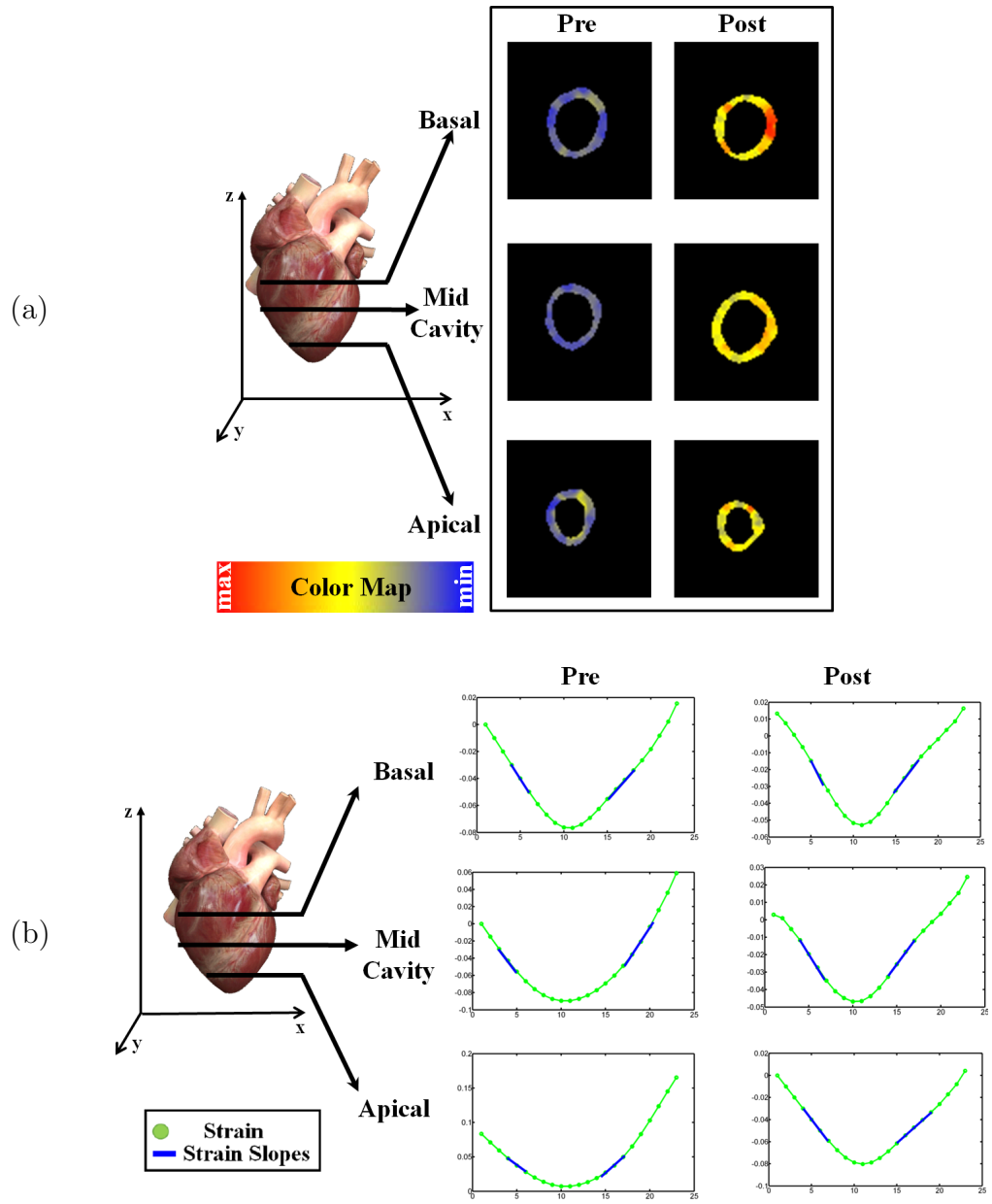
Figure 35. Pre and post (a) thickening and (b) strain results using our proposed method for a second sample patient, illustrated on 2D basal, mid-cavity, and apical cross-sections.

using a 1.5-T Siemens Espree scanner and phased-array cardiac coil reception with the maximum gradient amplitude of 33 $\frac{mT}{m}$ and maximum slew rate of 100 $\frac{mT.m^{-1}}{s}$. An ECG-triggered segmented k-space fast gradient echo sequence was performed with typical grid tag spacing of 10 mm; echo time of 4.0 ms; repetition time of 44.0 ms; flip angle of 14 degrees; voxel size of 1.48 x 1.48 x 10 mm; bandwidth of 184 $\frac{Hz}{voxel}$; 12-20 cardiac cycle frames, and typical total acquisition time of 15-20 seconds (the breath held imaging).

Our initial experiments report a higher mean correlation coefficient (r=0.97) between our estimated strain curves and the global ventricular volume curves (GVVCs) of the participating subjects enrolled in this study than between the strain curves estimated using the HARP method (r=0.87) and the GVVCs of the same subjects. Fig. 36 exemplified the comparison results for one patient enrolled in this study. These results highlight the ability of the proposed method to provide more correlated heart indexes since all of the derived metrics are estimated from cine CMR. This avoids the need for additional tagged images and thus overcomes the inter-slice variability problem associated with estimating the functional assessment metrics from different image modalities with different image resolution.

G   Summary

A novel framework for thickening and strain estimation from cine CMR images is presented. The LV wall points are tracked throughout the cardiac cycle by applying a PDE method to track the LV points by solving the Laplace equation in 3D between the LV wall borders. The main advantage of the proposed tracking method over traditional texture-based methods is its ability to track the movement and rotation of the LV wall based on tracking the geometric features of the inner, mid-, and outer walls of the LV. This overcomes noise sources that come from scanner and heart motion. Moreover, the proposed method will allow an accurate estimation of the correlation coefficients between the strain index and other
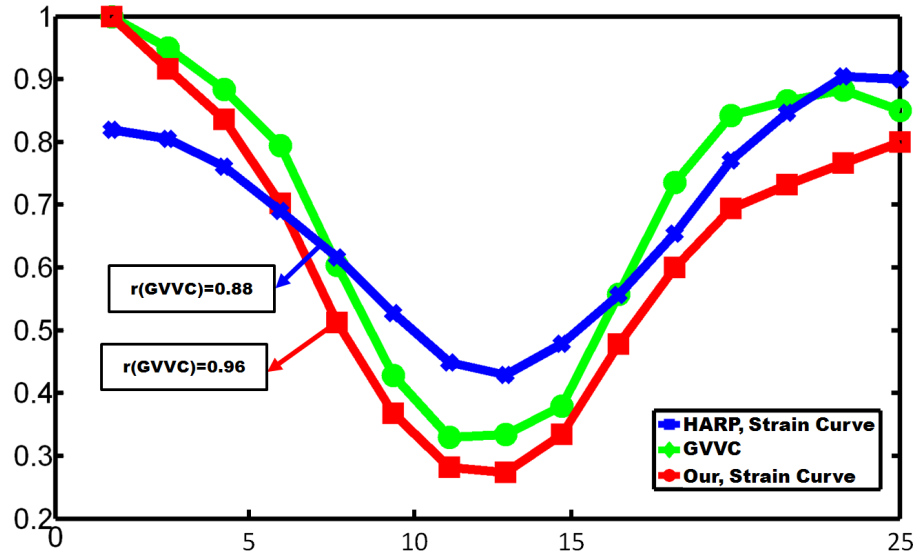
Figure 36. Comparison results between our estimation and HARP based estimation of the endocardium circumferential strain curve of a sample patient enrolled in this study. Arrows indicate the correlation coefficient between the estimated strain curves and the global ventricular volume curve (GVVC).

performance indexes derived from cine images, such as global (e.g., ejection fraction) and local (e.g., wall thickening) indexes. This will avoid the inter-slice variability problem since all indexes will be derived from cine CMR data.

CHAPTER V

CONCLUSION

Efficient and robust determination of ventricular measurements requires accurate delineation of the myocardial boundaries. However, accurate segmentation of the left ventricle (LV) wall borders is still a challenge. In this dissertation, we propose a novel 3D (2D + time) approach for the segmentation of the LV wall borders from cine cardiac magnetic resonance (CMR) images using coupled bi-directional parametric deformable models. The control points of the deformable models are tracked using a new external force that incorporates first– and second–order visual appearance features of the cine images in addition to the traditional contour internal force. The incorporation of these new features leads to an accurate segmentation, as evidenced by both the Dice similarity coefficient (DSC) and a distance metric on a cohort of 15 cine CMR data. For setting the size of the tracking search space (i.e., the size of the nearest neighbors' matrix), the effect of the temporal changes in the position/orientation of this 2D slice during imaging has been studied. For a typical temporal resolution of 25 image frames over the cardiac cycle (the typical case in this study), a search space of 3x3 pixels is necessary for tracking any control point to account for the temporal changes between the image frames. Note that for a higher spatial resolution (i.e., lower number of time frames over the cardiac cycle), one may expect the necessity to increase the tracking search space in order to cover the higher temporal changes between the temporal image frames.

In terms of practicality of computations, the present Matlab implementation on the Intel quad-core processor (3.2 GHz each; 16 GB memory) and a 1.5 TB hard

drive with RAID technology takes 51.9 ± 1.3 seconds for the wall border segmentation on a given time series (25 temporal images) of the CMR dataset.

In terms of the clinical benefits of our approach, the proposed method allows us to accurately estimate the ejection fraction (EF) as a representative of the global performance indexes of the heart. The proposed approach is not limited to the segmentation of the LV wall borders from short-axis cine CMR images, but can be used for other modalities and medical structures.

A novel 4D (3D+time) tracking approach for accurate assessment of myocardium function using cine CMR is presented. The experimental results on *in vivo* data demonstrated the ability of the proposed approach for detecting the out-of-plane heart motion which leads to accurate estimation of both 3D strain and wall thickening assessment metrics. The main advantage of estimating 3D functional strain from cine CMR is that it allows an accurate calculation of the correlation coefficients between the 3D strain index and other performance indexes derived from cine images, such as wall thickening and other global and local indexes. Therefore, the proposed approach can stand alone without the need for extra tagged images.

Our future work includes testing the generality of our segmentation approach in segmenting other medical structures from other modalities, since it shows promising results in the segmentation of the LV wall borders. In addition, our future work will also include the extension of the current 3D implementation (2D + time) to 4D (3D + time), thanks to the technological progress in rapid MR acquisition of image sequences having sufficient spatial and temporal resolutions. We also plan to ultimately test our framework to characterize pre- and post-treatment wall function status, and to investigate other types of correlation between local and global indexes for patients with ischemic heart diseases who are undergoing a myoregneration stem cell therapy.

REFERENCES

[1] Dr. Carl Bianco, "How your Heart Works,"
http://science.howstuffworks.com/life/human-biology/heart.htm

[2] http://www.webmd.com/heart-disease/heart-failure/
heart-failure-overview

[3] http://commons.wikimedia.org/wiki/File:
Diagram_of_the_human_heart_(cropped).svg

[4] http://www.nhlbi.nih.gov/health/health-topics/topics/hhw/

[5] http://www.medicalnewstoday.com/articles/237191.php

[6] Centers for Disease Control and Prevention. State Specific Mortality from
Sudden Cardiac Death: United States, 1999. MMWR. 2002;51(6):123126.

[7] http://www.nlm.nih.gov/medlineplus/heartdiseases.html

[8] http://www.who.int/mediacentre/factsheets/fs310/en/

[9] A. Schllhuber , "Fully automatic segmentation of the myocardium in cardiac
perfusion MRI," *Engineering in Medicine*, 2008.

[10] J. C. Velos, "A review of cardiac imaging modalities," *In Nurse practitioner
forum,* vol. 2, no. 4, pp. 231–238, 1991

[11] J. B. Garrison, W. L. Ebert, R. E. Jenkins, S. M. Yionoulis, H. Malcom, G. A.
Heyler, A. A. Shoukas, W. L. Maughan, and K. Sagawa, "Measurement of
threedimensional positions and motions of large numbers of spherical
radiopaque markers from biplane cineradiograms," *Computers and Biomedical
Research,* vol. 15, no. 1, pp. 76–96, 1982.

[12] A. Flotats, J. Knuuti, M. Gutberlet, C. Marcassa, F. M. Bengel, P. A. Kaufmann, M. R. Rees, and B. Hesse, "Hybrid cardiac imaging: SPECT/CT and PET/CT," *A joint position statement by the European Association of Nuclear Medicine (EANM), the European Society of Cardiac Radiology (ESCR) and the European Council of Nuclear Cardiology (ECNC). European journal of nuclear medicine and molecular imaging,* vol. 38, no. 1, pp.201–212, 2011.

[13] B. J. King,"Current Cardiology Diagnostic Modalities and Patient Dosimetry," `http: //nuclearcardiologyseminars.com/articles/Cardiology-Dosimetry.pdf`

[14] "Role of Ultrasound" `http://mustikamax.blogspot.com/2012/07/role-of-ultrasound.html`

[15] "Echocardiography," `http://en.wikipedia.org/wiki/Echocardiography`

[16] A. S. Celebi, H. Yalcin, and F. Yalcin, "Current cardiac imaging techniques for detection of left ventricular mass," *Cardiovascular Ultrasound,* vol. 8, no. 1, pp.8:19, 2010.

[17] "CT of the heart: Principles, advances, clinical uses," *Cleveland Clinic journal of medicine,* vol. 72, no. 2, pp. 127–138, 2005.

[18] `http: //imaging.cancer.gov/patientsandproviders/cancerimaging/ctscans`

[19] S. S. Halliburton, "Recent technologic advances in multi-detector row cardiac CT," *Cardiology clinics,* vol. 27, no. 4, pp. 655-664, 2009.

[20] A. P.Dhawan, H. K. Huang, and D.-S. Kim, "Principles and advanced methods in medical imaging and image analysis". World Scientific, 2008.

[21] `http://www.imaging.sbes.vt.edu/research/cardiac-ct/`

[22] http://en.wikipedia.org/wiki/File:Nl_mpi2.jpg

[23] http://radiology.med.nyu.edu/about-us/specialities/cardiac-imaging

[24] W. A. Kalender, "Computed tomography," (2001): 1610.

[25] http://mustikamax.blogspot.com/2012/07/

[26] T. Gyrke, "Nuclear Medicine,"
http://oftankonyv.reak.bme.hu/tartalom/eng/nm_eng_gyt.pdf

[27] F. M. Bengel, T. Higuchi, M. S. Javadi, R.Lautamki, "Cardiac Positron
Emission Tomography," *Journal of the American College of Cardiology,* vol. 54,
no. 1, pp. 1–15, 2009.

[28] E. C. Lin, "Cardiac MRI, Technical Aspects Primer,"
http://emedicine.medscape.com/article/352250-overview#showall

[29] Piotr Kozlowski, "Chapter 8. Magnetic Resonance Imaging," *John Wiley &
Sons, Inc.,* DOI: 10.1002/9780470451816.ch8, 2009.

[30] http://www.nuclearcardiologyseminars.net/di.htm

[31] H. Wang and A. A. Amini, "Chapter 11. MRI of Myocardial
Deformations:Imaging and Modeling," *CRC Press*, Print ISBN:
978-1-4398-7102-7, eBook ISBN: 978-1-4398-7103-4, DOI: 10.1201/b12939-12,
pp. 1-38, 2012.

[32] A. Frangi, W. Niessen, and M. A. Viergever, "Three-Dimensional Modeling for
Functional Analysis of Cardiac Images: A Review," *TMI.,IEEE*, vol. 20, no. 1,
pp. 2-25, 2001.

[33] A. K. Attili, A. Schuster, E. Nagel, J. H. C. Reiber, R. J. van der Geest,
"Quantification in cardiac MRI: advances in image acquisition and processing,"
Int J Cardiovasc Imaging, vol. 26, no. 1, pp. 2740, 2010.

[34] http://en.wikipedia.org/wiki/MRI

[35] http://www.insideradiology.com.au/pages/view.php?T_id=53&ref_info#17

[36] J. M. Groen, P. A. van der Vleuten, M. J. W. Greuter, F. Zijlstra, M. Oudkerk, "Comparison of MRI, 64-slice MDCT and DSCT in assessing functional cardiac parameters of a moving heart phantom," *European radiology,* vol. 19, no. 3, pp. 577–583, 2009.

[37] F. H. Epstein, "MRI of left ventricular function," *J Nucl Cardiol.*, vol. 14, no. 5, pp. 729-44, 2007.

[38] Zerhouni EA, Parish DM, Rogers WJ, Yang A, Shapiro EP., "Human heart: tagging with MR imaginga method for noninvasive assessment of myocardial motion," *Radiology*, vol. 169, no. 5963, 1988.

[39] Rademakers FE, Buchalter MB, Rogers WJ, Zerhouni EA, Weisfeldt ML, Weiss JL, Shapiro EP, "Dissociation between left ventricular untwisting and filling Accentuation by catecholamines," *Circulation*, vol. 85, no. 4, pp. 1572-81, 1992.

[40] D. J. Pennell, U. P. Sechtem, C. B. Higgins, W. J. Manning, G. M. Pohost, F. E. Rademakers, A. C. van Rossum, L. J. Shaw, E. K. Yucel, "Clinical indications for cardiovascular magnetic resonance (CMR): Consensus Panel reportq," *European Heart Journal*, vol. 25, no. 21, pp. 19401965, 2004.

[41] Ernesto Castillo, Joao A. C. Lima, David A. Bluemke, "Regional Myocardial Function: Advances in MR Imaging and Analysis," *Radiographics*, vol. 23, no. S127-40, 2003.

[42] V. Dilsizian, and G. M. Pohost, "Cardiac CT, PET and MR," *John Wiley & Sons*, 2011.

[43] P. Shi , H. Liu, " tochastic finite element framework for simultaneous estimation of cardiac kinematic functions and material parameters," *Medical Image Analysis,* vol. 7, no. 4, pp. 445-464, 2003.

[44] X. Papademetris, and J. S. Duncan, "Cardiac image analysis: Motion and deformation," *Handbook of Medical Imaging,* vol. 2, pp. 675–710, 2000.

[45] H. Michaely, K. Herrmann, K. Nael, N. Oesingmann, M. Reiser, and S. Schoenberg, "Functional renal imaging: Nonvascular renal disease," *Abdominal Imaging,* vol. 32, no. 1, pp. 1-16, 2007.

[46] F. Khalifa, A. El-Baz, G. Gimelfarb, and M. Abu El-Ghar, "Non-invasive image-based approach for early detection of acute renal rejection," *Medical Image Computing and Computer-Assisted InterventionMICCAI,* pp. 10-18, Springer Berlin Heidelberg, 2010.

[47] A. Elnakib, "DEVELOPING ADVANCED MATHEMATICAL MODELS FOR DETECTING ABNORMALITIES IN 2D/3D MEDICAL STRUCTURES," *PhD Thesis*, University of Louisville, Louisvilee, KY, USA, 2013.

[48] R. J. Kim, E. Wu, A. Rafael, E.-L. Chen, M. A. Parker, O. Simonetti, F. J. Klocke, R. O. Bonow, and R. M. Judd, "The use of contrast-enhanced magnetic resonance imaging to identify reversible myocardial dysfunction," *The New England Journal of Medicine,* vol. 43, no. 20, pp. 1445-1453, 2000.

[49] V. S. Lee, D. Resnick, S. S. Tiu, "MR imaging evaluation of myocardial viability in the setting of equivocal SPECT results with 99mTc sestamibi," *Radiology*, vol. 230, no. 1, pp. 191197, 2004.

[50] J. Vogel-Claussen, C. E. Rochitte, K.C. Wu, I. R. Kamel, T. K. Foo, J. A. Lima, D. A. Bluemke, "Delayed enhancement MR imaging: utility in myocardial assessment," *Radiographics*, vol. 26, no. 3, pp. 79, 2006

[51] N. Al-Saadi, E. Nagel, M. Gross, A. Bornstedt, B. Schnackenburg, and C. E. A. Klein, "Noninvasive Detection of Myocardial Ischemia From Perfusion Reserve Based on Cardiovascular Magnetic Resonance," *Circulation,* vol. 101, no. 12, pp. 1379-1383, 2000

[52] S. D. Wolff, J. Schwitter, R. Coulden, M. Friedrich, D. Bluemke, R. Biederman, E. Martin, A. Lansky, F. Kashanian, T. Foo, P. Licato, and C. Comeau, "Myocardial First-Pass Perfusion Magnetic Resonance Imaging," *Circulation,* vol. 110, no. 6, pp. 732-737, 2004

[53] S. Busch, T. R. C. Johnson, B. J. Wintersperger, N. Minaifar, A. Bhargava, C. Rist, M. F. Reiser, C. Becker, K. Nikolaou, "Quantitative assessment of left ventricular function with dual-source CT in comparison to cardiac magnetic resonance imaging: initial findings," *European radiology,* vol. 18, no. 3, pp. 570–575, 2008.

[54] M. Prasad, A. Ramesh, P. Kavanagh, B. K. Tamarappoo, R. Nakazato, J. Gerlach, V. Cheng, L. E. J. Thomson, D. S. Berman, G. Germano, and P.J. Slomka, "Automated quantification of 3D regional myocardial wall thickening from gated Magnetic Resonance images," *Journal of Magnetic Resonance Imaging,* vol. 31, no. 2, pp. 317327, 2010

[55] M. Y. Henein (Editor), *Heart failure in clinical practice*, Springer-Verlag: London, 2010.

[56] E. C. Barbier, L. Johansson, L. Lind, H. Ahlstrom, and T. Bjerner, "The exactness of left ventricular segmentation in cine magnetic resonance imaging and its impact on systolic function values," *Journal of Acta Radiologica*, vol. 48, no. 3 pp. 285–91, 2007.

[57] B. Sievers, S. Kirchberg, A. Bakan, U. Franken, and H.-J. Trappe, "Impact of papillary muscles in ventricular volume and ejection fraction assessment by

cardiovascular magnetic resonance," *Journal of Cardiovascular Magnetic Resonance*, vol. 6, no. 1, pp. 9–16, 2004.

[58] P. Thunberg, K. Emilsson, P. Rask, and A. Kahari, "Estimation of ejection fraction and stroke volume using single- and biplane magnetic resonance imaging of the left cardiac ventricle," *Journal of Acta Radiologica*, vol. 49, no. 9, pp. 1016–23, 2008.

[59] I. Ben Ayed, S. Li, and I. Ross, "Embedding overlap priors in variational left ventricle tracking," *IEEE Transaction on Medical Imaging*, vol. 28, no. 12, pp. 1902–13, 2009.

[60] I. Ben Ayed, Y. Lu, S. Li, and I. Ross, "Left ventricle tracking using overlap priors," *Proceedings of Medical Image Computing and Computer-Assisted Intervention*, vol. 11, no. 1, pp. 1025–33, 2008.

[61] C. Li, X. Jia and Y. Sun, "Improved semi-automated segmentation of cardiac CT and MR images," *IEEE International Symposium on Biomedical Imaging*, vol. 11, no. 6, pp. 25–28, 2009.

[62] W. Feng, H. Nagaraj, H. Gupta, S. G. Lloyd, I. Aban, G. J. Perry, D. A. Calhoun, L. J. Dell'Italia and T. S. Denney Jr, "A dual propagation contours technique for semi-automated assessment of systolic and diastolic cardiac function by CMR," *Journal of Cardiovascular Magnetic Resonance*, vol. 11, no. 1, pp. 30, 2009.

[63] T. Chen, J. Babb, P. Kellman, L. Axel, and D. Kim, "Semiautomated segmentation of myocardial contours for fast strain analysis in cine displacement-encoded MRI," *IEEE Transactions on Medical Imaging*, vol. 27, no. 8, pp. 1084–94, 2008.

[64] A. Pednekar, U. Kurkure, R. Muthupillai, S. Flamm, and I. A. Kakadiaris,

"Automated left ventricular segmentation in cardiac MRI," *IEEE Transactions on Biomedical Engineering*, vol. 53, no. 7, pp. 1425–8, 2006.

[65] M. Uzumcu, R. van der Geest, C. Swingen, J. Reiber and B. Lelieveldt, "Time continuous tracking and segmentation of cardiovascular magnetic resonance images using multidimensional dynamic programming," *Investigative Radiology*, vol. 41, no. 1, pp. 52–62, 2006.

[66] C. Petitjean and J.-N. Dacher, "A review of segmentation methods in short axis cardiac MR images," *Medical Image Analysis*, vol. 15, no. 2, pp. 169–184, 2011.

[67] F. Khalifa, G. M. Beache, G. Gimel'farb, G. A. Giridharan, and A. El- Baz, "Accurate automatic analysis of cardiac cine images," *IEEE Transactions on Biomedical Engineering*, vol. 59, no. 2, pp. 445–55, 2012.

[68] F. Khalifa, G. M. Beache, M. Nitzken, G. Gimel'farb, G. Giridharan, A. El-Baz, "Automatic analysis of left ventricle wall thicknessusing short-axis cine CMR images," *IEEE International Symposium on Biomedical Imaging*, pp. 1306–9, 2011.

[69] F. Khalifa, G. M. Beache, A. El-Baz, G. Gimel'farb, "Deformable model guided by stochastic speed with application in cine images segmentation," *IEEE International Conference on Image Processing*, pp. 1725–8, 2010.

[70] S. P. O'Brien, O. Ghita, and P. F.Whelan, "A Novel Model-Based 3-D+ Time Left Ventricular Segmentation Technique," *IEEE Transactions on Medical Imaging,* vol. 30, no. 21, pp. 461–474,2011.

[71] J. Cousty, L. Najman, M. Couprie, S. Clément-Guinaudeau, T. Goissen, and J. Garot, "4D cardiac MRI: Automated method based on spatio-temporal watershed cuts," *Image and Vision Computing,* vol. 28, no. 8, pp. 1229–1243 ,2010.

[72] H. Zhang, A. Wahle, R. K. Johnson, T. D. Scholz, and M. Sonka, "4-D cardiac MR image analysis: left and right ventricular morphology and function," *IEEE Transactions on Medical Imaging*, vol. 29, no. 2, pp. 350–64, 2010.

[73] A. Andreopoulos, and J. K.Tsotsos, "Efficient and generalizable statistical models of shape and appearance for analysis of cardiac MRI," *Medical Image Analysis,* vol. 12, no. 3, pp. 335–357 ,2008.

[74] M. Jolly, H. Xue, L. Grady, and J. Guehring "Combining registration and minimum surfaces for the segmentation of the left ventricle in cardiac cine MR images," *Proceedings of Medical Image Computing and Computer-Assisted Intervention*, vol. 12, no. 2, pp. 910–8, 2009.

[75] U. Kurkure, A. Pednekar, R. Muthupillai, S. D. Flamm, and I. A. Kakadiaris, "Localization and segmentation of left ventricle in cardiac cine-MR images," *IEEE Transactions on Biomedical Engineering*, vol. 56, no. 5, pp. 1360–70, 2009.

[76] C. A. Cocosco, W. J. Niessen, T. Netsch, E. P. A. Vonken, G. Lund, A. Stork, and M. A. Viergever, "Automatic image-driven segmentation of the ventricles in cardiac cine MRI," *Journal of Magnetic Resonance Imaging*, vol. 28, no. 2, pp. 366–74, 2008.

[77] M. Lynch, O. Ghita, and P. F. Whelan, "Segmentation of the left ventricle of the heart in 3-D+t MRI data using an optimized nonrigid temporal model," *IEEE Transactions on Medical Imaging*, vol. 27, no. 2, pp. 195–203, 2008.

[78] J. Liang, G. Ding, and Y. Wu, "Segmentation of the left ventricle from cardiac MR images based on radial GVF snake," *Proceedings of the International Conference on Biomedical Engineering Informatics*, vol. 2, pp. 238-42, 2008.

[79] X. Han, C. Xu, and J. L. Prince, "A topology preserving level set method for

geometric deformable models," *IEEE Transactions on Pattern Analysis and Machine Intelligence*, vol. 25, no. 6, pp. 61–79, 2009.

[80] X. Zhuang, D. J. Hawkes, W. R. Crum, R. Boubertakh, S. Uribe, D. Atkinson, P. Batchelor, T. Schaeffter, R. Razavi, and D. L. G. Hill, "Robust registration between cardiac MRI images and atlas for segmentation propagation," *Proceedings of SPEI on Medical Imaging*, vol. 6914, pp. 7., 2007

[81] S. Zambal, J. Hladvka, and K. Bhler, "Improving segmentation of the left ventricle using a two-component statistical model," *Proceedings of Medical Image Computing and Computer-Assisted Intervention*, vol. 9, pp. 151–8, 2006.

[82] M. Lynch, O. Ghita, and P. Whelan, "Left-ventricle myocardium segmentation using a coupled level-set with a priori knowledge," *Computerized Medical Imaging and Graphics*, vol. 30, no. 4, pp. 255–62, 2006.

[83] A. Katouzian, A. Prakash, and E. Konofagou, "A new automated technique for left- and right-ventricular segmentation in magnetic resonance imaging," *Proceedings of Engineering in Medicine and Biology Society*, pp. 3074–7, 2006.

[84] M. Jolly, "Automatic segmentation of the left ventricle in cardiac MR and CT images," *International Journal of Computer Vision*, vol. 70, no. 2, pp. 151–63, 2006.

[85] M. Jolly, N. Duta, and G. Funka-Lea, "Segmentation of the left ventricle in cardiac MR images," *Proceedings. Eighth IEEE International Conference on Computer Vision*, vol. 1, pp. 501–8, 2001.

[86] M. Lynch, O. Ghita, and P. Whelan, "Automatic segmentation of the left ventricle cavity and myocardium in MRI data," *Computers in Biology and Medicine*, vol. 6, no. 4, pp. 389–407, 2006.

[87] B. F. Lelieveldt, M. Uzumcu, R. J. van der Geest, J. C. Reiber, and M. Sonka, "Multi-view active appearance models for consistent segmentation of multiple standard views: Application to long- and short-axis cardiac MR images," *Proceedings of the 17th International Congress and Exhibition Computer Assisted Radiology and Surgery*, vol. 1256, pp. 1141–6, June 2003.

[88] J.C. Fu, J.W. Chai, Stephen T.C. Wong, "Wavelet-based enhancement for detection of left ventricular myocardial boundaries in magnetic resonance images," *Magnetic Resonance Imaging*, vol. 18, no. 1, pp. 1135–41 ,2000.

[89] P. Yan, A. Sinusas, and J. S. Duncan, "Boundary element method based regularization for recovering of LV deformation," *Medical Image Analysis*, vol. 11, no. 6, pp. 540–54, 2007.

[90] A. Lalande, L. Legrand, P. M. Walker, F. Guy, Y. Cottin, S. Roy, F. Brunotte, "Automatic detection of left ventricular contours from cardiac cine magnetic resonance imaging using fuzzy logic," *Investigative Radiology*, vol. 34, no. 3, pp. 211–7, 1999.

[91] N. Paragios, "A variational approach for the segmentation of the left ventricle in cardiac image analysis," *International Journal of Computer Vision,* vol. 50, no. 3, pp. 345–362,2002.

[92] Q. Song and J. Bai and M. K. Garvin and M. Sonka and J. M. Buatti and X. Wu, "Optimal Multiple Surface Segmentation With Shape and Context Priors," *IEEE Trans. Med. Imaging,* vol. 32, no. 2, pp. 376–386 ,2013.

[93] M. Kass, A. Witkin, and D. Terzopoulos, "Snakes: Active contour models," *International Journal of Computer Vision*, vol. 1, pp. 321–31, 1988.

[94] A. Farag, A. El-Baz, and G. Gimel'farb, "Precise segmentation of multimodal images," *IEEE Transactions on Image Processing*, vol. 15, no. 4, pp. 952–68, 2006.

[95] A. El-Baz, A. Soliman, P. McClure, G. Gimel'farb, M. A. El-Ghar, "Early assessment of malignant lung nodules based on the spatial analysis of detected lung nodules," *IEEE International Symposium on Biomedical Imaging*, pp. 1463–6, 2012.

[96] El-Baz, Ayman and Gimel'farb, Georgy and Abou El-Ghar, Mohamed and Falk, Robert, "Appearance-Based Diagnostic System for Early Assessment of Malignant Lung Nodules," *Proceedings of IEEE International Conference on Image Processing, (ICIP'12),* pp. 533–536, 2012.

[97] A. A. Farag, A. El-Baz, G. Gimelfarb, R. Falk, M. A. El-Ghar, T. Eldiasty, and S. Elshazly , "Appearance models for robust segmentation of pulmonary nodules in 3D LDCT chest images," In: *Proc. International Conference on Medical Image Computing and Computer-Assisted Intervention (MICCAI'06),* pp. 1662–1670, 2012.

[98] A. El-Baz, A. Elnakib, F. Khalifa, M. Abou El-Ghar, P. McClure, A. Soliman, and G. Gimel'farb, "Precise segmentation of 3-D magnetic resonance angiography," *IEEE Transactions on Biomedical Engineering*, vol. 59, no. 7, pp. 2019–29, 2012.

[99] A. El-Baz, "Novel stochastic models for medical image analysis," *PhD Thesis*, University of Louisville, Louisvilee, KY, USA, 2006.

[100] A. El-Baz, and G. Gimel'farb, "EM–Based Approximation of Empirical Distributions with Linear Combinations of Discrete Gaussians," *Proceedings of IEEE International Conference on Image Processing, (ICIP'07),*vol. 4, pp. 372–376, 2007.

[101] L. R. Dice, "Measures of the amount of ecologic association between species," *Ecological Society of America*, vol. 26, no. 3, pp. 297–302, 1945.

[102] T. F. Chan and L. A. Vese, "Active contours without edges," *IEEE Transaction on Medical Imaging*, vol. 10, pp. 266–77, 2001.

[103] Abd El Munim, H. E. and Farag, Aly A., "Curve/Surface representation and evolution using vector level sets with application to the shape-based segmentation problem," *IEEE Transactions on Pattern Analysis and Machine Intelligence*, vol. 29, no. 6, pp. 945–58, 2007.

[104] P. Radau and Y. Lu and K. Connelly and G. Paul and A. J. Dick and G. A. Wright, "Evaluation framework for algorithms segmenting short axis cardiac MRI," *MIDAS Journal - Cardiac MR Left Ventricle Segmentation Challenge*, , 2009.

[105] Y. Lu and P. Radau and K. Connelly and A. Dick and G. Wright, "Segmentation of Left Ventricle in Cardiac Cine MRI: An Automatic Image-Driven Method," *Functional Imaging and Modeling of the Heart,* pp. 339–347, 2009.

[106] S. O'Brien, O. Ghita, and P. F. Whelan, "Segmenting the Left Ventricle in 3D Using a Coupled ASM and a Learned Non-Rigid Spatial Model," *The MIDAS Journal – Cardiac MR Left Ventricle Segmentation Challenge,* `http://hdl.handle.net/10380/3110`, 2009.

[107] A. Elnakib, G. M. Beache, G. Gimel'farb, and A. El-Baz, "New automated Markov-Gibbs random field based framework for myocardial wall viability quantification on agent enhanced cardiac magnetic resonance images," *Int J Cardiovasc Imaging,* vol. 28, no. 7, pp. 1683-1698, 2012.

[108] J. M. Bland and D. G. Altman, "Statistical methods for assessing agreement between two methods of clinical measurement," *Lancet*, vol. 1, pp. 307–10, 1986.

[109] H. Sliman, F. Khalifa, A. Elnakib, A. Soliman, A. El-Baz, G. M. Beache, A. Elmaghraby, and G Gimel'farb, "Myocardial borders segmentation from cine

MR images using bidirectional coupled parametric deformable models," *Medical Physics,* vol. 40, no. 9, 2013.

[110] H. Sliman, F. Khalifa, A. Elnakib, A. Soliman, A. El-Baz, G. M. Beache, A. Elmaghraby, "A NEW SEGMENTATION-BASED TRACKING FRAMEWORK FOR EXTRACTING THE LEFT VENTRICLE CAVITY FROM CINE CARDIAC MRI," *IEEE International Conference on Image Processing, (ICIP'13),* `http://2013.ieeeicip.org/proc/pdfs/0000685.pdf`, 2013.

[111] H. Sliman, F. Khalifa, A. Elnakib, A. Soliman, G. M. Beache, G. Gimel'farb, A. Emam, A. Elmaghraby, and A. El-Baz, "Accurate Segmentation Framework for the Left Ventricle Wall from Cardiac Cine MRI," *the International Symposium on Computational Models for Life Sciences (CMLS 2013),* 2013.

[112] G. M. Beache, V. Wedeen, and R. Dinsmore, "Magnetic resonance imaging evaluation of left ventricular dimensions and function and pericardial and myocardial disease," *Coronary Artery Disease*, vol. 4, no. 4, pp. 328-333, 1993.

[113] E. R. Holman, H. W. Vliegen, R. J. van der Geest, J. H. C. Reiber, P. R. van Dijkman, A. van der Laarse, A. de Roos, and E. E. van der Wall, "Quantitative analysis of regional left ventricular function after myocardial infarction in the pig assessed with cine magnetic resonance imaging," *Magnetic Resonance in Medicine*, vol. 34, no. 2, pp. 161–169, 1995.

[114] S. Sasayama, D. Franklin, J. Ross Jr, W. S. Kemper, and D. McKown, "Dynamic changes in left ventricular wall thickness and their use in analyzing cardiac function in the conscious dog: A study based on a modified ultrasonic technique," *The American Journal of Cardiology*, vol. 38, pp. 870-879, 1976.

[115] F. H. Sheehan, E. L. Bolson, H. T. Dodge, D. G. Mathey, J. Schofer, and H. W. Woo, "Advantages and applications of the centerline method for

characterizing regional ventricular function," *Circulation*, vol. 74, pp. 293-305, 1986.

[116] H. Azhari, S. Sideman, J. L. Weiss, E. P. Shapiro, M. L. Weisfeldt, W. L. Graves, W. J. Rogers, and R. Beyar. "Three-dimensional mapping of acute ischemic regions using MRI: Wall thickening versus motion analysis," *American Journal of Physiology-Heart and Circulatory Physiology*, vol. 259, no. 5, pp. H1492-H1503, 1990.

[117] S. Pujadas, G. P. Reddy, O. Weber, J. J. Lee, C. B. Higgins, "MR Imaging Assessment of Cardiac Function," *Journal of Magnetic Resonance Imaging*, vol. 19, pp. 789-799, 2004.

[118] C. D. von Land, S. R. Rao, and J. H. C. Reiber, "Development of an improved centerline wall motion model," *IEEE Proceedings of Computers in Cardiology*, pp. 687-690, 1990.

[119] R. J. van der Geest, A. de Roos, E. E. van der Wall, J. H. C. Reiber, "Quantitative analysis of cardiovascular MR images," *The International Journal of Cardiac Imaging*, vol. 13, pp. 247-258, 1997.

[120] N. Beohar, J. D. Flaherty, C. J. Davidson, M. I. Vidovich, A. Brodsky, D. C. Lee, E. Wu, E. L. Bolson, R. O. Bonow, and F. H. Sheehan, "Quantitative assessment of regional left ventricular function with cardiac MRI: Threedimensional centersurface method," *Catheterization Cardiovasc. Interv.*, vol. 69, no. 5, pp. 721728, 2007.

[121] M. Prasad, A. Ramesh, P. Kavanagh, J. Gerlach, G. Germano, D. S. Berman, and P. J. Slomka, "Myocardial wall thickening from gated magnetic resonance images using Laplaces equation," in *Proc. SPIE2009*, vol. 72602I, Lake Buena Vista, FL, Feb. 10, pp. 18.

[122] A. Elnakib, G. M. Beache, G. Gimel'farb, T. Inanc, and A. El-Baz, "Validating a new methodology for strain estimation from cardiac cine MRI," *Proc. Int. Symp. Computational Models for Life Sciences,* vol. 1559, no. 1, pp. 277-286, 2013.

[123] M. J. Ledesma-Carbayo, J. Kybic, M. Desco, A. Santos, M. Suhling, P. Hunziker, and M. Unser, "Spatio-temporal nonrigid registration for ultrasound cardiac motion estimation," *IEEE Trans. Medical Imaging,* vol. 24, no. 9, pp. 1113-1126, 2005.

[124] A. Elen, H. F. Choi, D. Loeckx, H. Gao, P. Claus, P. Suetens, F. Maes, and J. D'hooge, "Three-dimensional cardiac strain estimation using spatiotemporal elastic registration of ultrasound images: A feasibility study," *IEEE Trans. Medical Imaging,* vol. 27, no. 11, pp. 1580-1591, 2008.

[125] T. S. Denney, Jr. and J. L. Prince, "Reconstruction of 3-D left ventricular motion from planar tagged cardiac MR images: An estimation theoretic approach," *IEEE Transactions on Medical Imaging,* vol. 14, no. 4, pp. 625–635, 1995.

[126] W. S. Kerwin and J. L. Prince, "Cardiac material markers from tagged MR images," *Med Image Anal,* pp. 339–353, 1998.

[127] N. F. Osman and J. L. Prince, "Visualizing myocardial function using HARP MRI," *Phys Med Biol,* pp. 1665–1682, 2000.

[128] N. F. Osman, E. R. McVeigh, and J. L. Prince, "Imaging heart motion using harmonic phase MRI," *IEEE Transactions on Medical Imaging,* vol. 19, no. 3, pp. 186–202, 2000.

[129] W. G. O'Dell, C. C. Moore, W. C. Hunter, E. A. Zerhouni, and E. R. McVeigh, "Three-dimensional myocardial deformations: Calculation with

displacement field fitting to tagged MR images," *Radiology*, vol. 195, pp. 829–835, 1995.

[130] X. Liu and J. L. Prince, "Shortest path refinement for motion estimation from tagged MR images," *IEEE Transactions on Medical Imaging*, vol. 29, no. 8, pp. 1560–1572, 2010.

[131] E. Maret, T. Todt, L. Brudin, E. Nylander, E. Swahn, J. L. Ohlsson, and J. E. Engvall, "Functional measurements based on feature tracking of cine magnetic resonance images identify left ventricular segments with myocardial scar," *Cardiovascular Ultrasound*, vol. 7, no. 53, 2009, doi:10.1186/1476-7120-7-53.

[132] K. N. Hor, W. M. Gottliebson, C. Carson, E. Wash, J. Cnota, R. Fleck, J. Wansapura, P. Klimeczek, H. R. Al-Khalidi, E. S. Chung, W. Benson, and W. Mazur, "Comparison of magnetic resonance feature tracking for strain calculation with harmonic phase imaging analysis," *JACC: Cardiovascular Imaging*, vol. 3, no. 3, pp. 144–151, 2010.

[133] K. N. Hor, R. Baumann, G. Pedrizzetti, G. Tonti, W. M. Gottliebson, M. Taylor, W. Benson, and W. Mazur, "Magnetic resonance derived myocardial strain assessment using feature tracking," *Journal of Visualized Experiments*, vol. 48, 2011, doi: 10.3791/2356.

[134] A. Schuster, S. Kutty, A. Padiyath, V. Parish, P. Gribben, D. A. Danford, M. R. Makowski, B. Bigalke, P. Beerbaum, and E. Nage, "Cardiovascular magnetic resonance myocardial feature tracking detects quantitative wall motion during dobutamine stress," *Journal of Cardiovascular Magnetic Resonance*, vol. 13, no. 58, 2011.

[135] C. Bouman and K. Sauer, "A generalized Gaussian image model for edge-preserving MAP estimation," *IEEE Transactions on Medical Imaging,* vol. 2, no. 3, pp. 296–310, 1993.

[136] J. Besag, "On the statistical analysis of dirty pictures," *Journal of the Royal Statistical Society. Series B,* vol. 48, no. 3, pp. 259–302, 1986.

[137] J. Bonet and R. D. Wood, *Nonlinear continuum mechanics for finite element analysis*, Cambridge University Press, 1997.

CURRICULUM VITAE

NAME: Hisham Z. Sliman

ADDRESS:

> Department of Computer Engineering and Computer Science
>
> University of Louisville
>
> Louisville, KY 40292

EDUCATION:

- **Ph.D. Computer Science Engineering,** University of Louisville, Louisville, KY 2014

- **M.S. Electrical and Computer Engineering,** Purdue School of Engineering and Technology, Indianapolis, IN 2006

- **B.S. Electrical and Computer Engineering,** AinShams Univ., Faculty of Engineering , Cairo, Egypt, 2004

Thesis/Dissertation:

- **Ph.D. Dissertation:** Image Based Approach for Early Assessment of Heart Failure

- **M.S. Thesis:** Enhancements for the VC-1 Video Coding Standard

TEACHING:

- Digital Signal Processing

- Power Electronics

- Data structures using C++

AWARDS AND RECOGNITION:

- The 1st place winner in the annual Research!Louisville 2013, Student Engineering Collaboration category

- The Best Paper Runner-up for CMLS-13. "Accurate Segmentation Framework for the Left Ventricle Wall from Cardiac Cine MRI," (http://cmls-conf.org/2013/index.php?page=prizes)

- Top 10% recognition for ICIP 2013, which places the paper within the top 4.5% of all submissions to ICIP 2013. "A New Segmentation-based Tracking Framework for Extracting the Left Ventricle Cavity from Cine Cardiac MRI"

- A two-year fellowship, 2009-2011, from the University of Louisville

- Partial tuition remission for the MSECE

- Best IUPUI's student for the year 2007-2008

- Graduated 4th/200 with distinct and honor from AinShams Univ., Cairo, Egypt 2004

HONOR SOCIETIES:

- Member of the 'International Golden Key Honor Society' since Oct. 2009

- Member of the 'Cambridge Who's Who Honor Society' since Oct. 2009

COURSE WORK:

- Data Mining, Artificial Intelligence, Pattern Recognition, Machine Learning, Data Analysis, Predictive Modeling, E-commerce and Web Data Mining, Combinatorial Optimization, Medical Image Analysis

- Image and Video Processing, Multimedia Applications, Digital Signal Processing, Algorithm Techniques, Voice Over IP, Statistics

- Analog/Digital Circuits, Basic Communications, Energy Conversion, Programmable Logic Controllers

LANGUAGES:

- English

- Arabic

SKILLS:

- Good understanding of Physics and Mathematics

- Excellent in data manipulation, troubleshooting and problem-solving skills

- Knowledge of Machine Learning, Image Processing, Predictive modeling, and Data Analysis

- Knowledge of Matlab, Python, C/C++, R, Relational algebra, SQL, and Microsoft Office tools.

PUBLICATIONS:

- H. Sliman, F. Khalifa, A. Elnakib, A. Soliman, G. M. Beache, A. Elmaghraby, G. Gimel'farb, and A. El-Baz "Myocardial Borders Segmentation from Cine MR Images Using Bi-Directional Coupled Parametric Deformable Models," in Medical Physics, vol. 40, no. 9, pp. 1-13, 2013.
  Doi="http://dx.doi.org/10.1118/1.4817478"

- H. Sliman, F. Khalifa, A. Elnakib, A. Soliman, G. M. Beache, G. Gimel'farb, A. Emam, A. Elmaghraby and A. El-Baz "Accurate Segmentation Framework for the Left Ventricle Wall from Cardiac Cine MRI," in the International Symposium on Computational Models for Life Sciences (CMLS 2013), Sydney, Australia, November 27-29, 2013

- H. Sliman, F. Khalifa, A. Elnakib, A. Soliman, G. M. Beache, A. Elmaghraby, and A. El-Baz "A New Segmentation-based Tracking Framework for Extracting the Left Ventricle Cavity from Cine Cardiac MRI," Proceedings of the IEEE International Conference on Image Processing (ICIP 2013), Melbourne, Australia, September 15-18, 2013, (**selected for oral presentation**)

- A. Elnakib, G. Beache, H. Sliman, G. Gimel'farb, T. Inanc, and A. El-Baz, "A Novel Laplace-Based Method to Estimate the Strain from Cine Cardiac Magnetic Resonance Images," Proceedings of the IEEE ICIP'13, Melbourne, Australia, September 15-18, pp. 690-694, 2013, (**selected for oral presentation**)

- F. Khalifa, G. M. Beache, A. Elnakib, H. Sliman, G. Gimel'farb, K. C. Welch, and A. El-Baz, "A new shape-based Framework for the left ventricle wall segmentation from cardiac first-pass perfusion MRI," Proceedings of the IEEE International Symposium on Biomedical Imaging: From Nano to Macro (ISBI'13), San Francisco, CA, April 7-11, 2013, pp. 41-44

- H. Sliman, M. El-Sharkawy, P. Salama and M. Rizkalla, "All-zero Block Detection in VC-1," IEEE Midwest Symposium on Circuits and Systems, August 2-5, 2009, Cancun, Mexico

- H. Sliman, M. El-Sharkawy, M. Rizkalla and P. Salama, "Improving VC-1 In Loop Deblocking Filter," International Conference on Image Processing, Computer Vision, and Pattern Recognition (IPCV'09 : WORDCOM09), July 13-16, 2009, Las Vegas, USA

- M. J. Tammen, M. El-Sharkawy, H. Sliman and M. Rizkalla "Advanced Motion Estimation Techniques for VC-1," IEEE International Symposium on Signal Processing and Information Technology, 2007 , pp. 240-245. IEEE, 2007

- M. Tammen, M. El-Sharkawy, H. Sliman, M. Rizkalla, "Fast Implementation of VC-1 with Modified Motion Estimation and Adaptive Block Transform," Circuits and Systems, vol.1 no.1, July 2010, pp. 12-17. Doi="10.4236/cs.2010.11003"